7-11-2013

Understanding the Role of Gravity in the Crystallization Suppression of ZBLAN Glass

Anthony Torres

Follow this and additional works at: https://digitalrepository.unm.edu/ce_etds

Anthony Samuel Torres

Candidate

Civil Engineering

Department

This dissertation is approved, and it is acceptable in quality and form for publication:

Approved by the Dissertation Committee:

Dr. Arup K. Maji , Chairperson

Dr. Jeff M. Ganley

Dr. Mahmoud R. Taha

Dr. Yu-Lin Shen

**UNDERSTANDING THE ROLE OF GRAVITY
IN THE CRYSTALLIZATION SUPPRESSION
OF ZBLAN GLASS**

by

ANTHONY SAMUEL TORRES

B.S. Civil Engineering, New Mexico State University, 2008

M.S. Civil Engineering, University of New Mexico, 2010

DISSERTATION

Submitted in Partial Fulfillment of the
Requirements for the Degree of

**Doctor of Philosophy
Engineering**

The University of New Mexico
Albuquerque, New Mexico

May, 2013

DEDICATION

This dissertation is dedicated to my wife, Allison, for her unwavering support to pursue

my dreams. This dissertation wouldn't exist without her love and encouragement.

ACKNOWLEDGEMENTS

UNDERSTANDING THE ROLE OF GRAVITY IN THE CRYSTALLIZATION SUPPRESSION OF ZBLAN GLASS

By:

Anthony Samuel Torres

B.S., Civil Engineering, New Mexico State University, 2008

M.S., Civil Engineering, University of New Mexico, 2010

Ph.D., Engineering, University of New Mexico, 2013

ABSTRACT

Fluorozirconate glasses, such as ZBLAN (ZrF4-BaF2-LaF3-AlF3-NaF), have the potential for optical transmission from 0.3 μm in the UV to 7 μm in the IR region. However, crystallites formed during the fiber drawing process prevent this glass from achieving its low loss-capability. Other researchers have shown that microgravity processing leads to suppressed crystal growth in ZBLAN glass, which can lead to lower transmission loss in the desired mid-IR range. However, the mechanism governing crystal growth suppression has not been thoroughly investigated. In the present research multiple ZBLAN samples were subjected to a heating and quenching test apparatus on a parabolic aircraft under controlled μ-g and hyper-g environments and compared with 1-g ground tests. Optical microscopy (transmission and polarized) along with SEM examination elucidates that crystal growth in ZBLAN is suppressed when processed in a microgravity environment. Hence crystallization occurs at a higher temperature in μ-g

and the working temperature range at which the fiber can be manufactured has been extended.

We postulate that the fundamental process of nano-scale mass transfer (lack of buoyancy driven convection) in the viscous glass is the mechanism responsible for crystal growth suppression in microgravity. Suppressing molecular mobility within the semi-molten glass starves nucleating crystallites and prevents any further growth. A COMSOL Multi-Physics model was developed to show the velocity contours due to convection processes in a 1-g, μ-g, and hyper-g environment. Analytical models show that while suppressing convection is relevant at fiber drawing temperatures (360°C), mass transfer due to diffusion dominates at higher temperatures leading to crystal growth at temperatures ≥400°C.

ZBLAN fibers are also known for their poor handling ability. Therefore an analysis of the thermal degradation of ZBLAN optical fibers based on fracture mechanics was also conducted. Conditions of crack initiation and stable versus unstable crack growth leading to fiber fracture were analyzed to explain behavior observed from controlled flexure tests of ZBLAN optical fibers exposed to various temperatures.

TABLE OF CONTENTS

LIST OF FIGURES

LIST OF TABLES

CHAPTER 1 – Introduction

1.1 Outline of Dissertation

In Chapter 1, an introduction and history of ZBLAN glass is given, along with an overview of microgravity for those readers who are not familiar with the topic.

Chapter 2 provides background information regarding crystal growth in vitreous materials and microgravity research particularly as it relates to ZBLAN. A detailed summary of past researchers' microgravity experiments and analysis is given, in addition to conjectured theories as to why crystallization is suppressed in microgravity. Processes of mass transfer governing nucleation and crystallization are also described. Furthermore, a literature survey is summarized in relation to the mechanical properties and handling ability of ZBLAN fibers.

Chapter 3 provides a summary of the experimental program completed during the course of the present research. The testing apparatus flown on two microgravity flights known as The Quencher is fully described and characterized. All materials and testing temperatures are also summarized.

In Chapter 4, detailed descriptions of all significant results obtained from the experimental program are summarized and explained. Multiple techniques were used to explicate crystallization in the ZBLAN samples, which include; phase contrast microscopy, polarized optical microscopy, and Scanning Electron Microscopy (SEM). Additional analytical models, such as COMSOL Multi-Physics, are described, which support the mass transport analysis.

Chapter 5 contains the additional study of the fragility of ZBLAN fibers. ZBLAN fibers are known to be extremely brittle; therefore a separate thermal degradation and

fracture mechanics study is described. Chapter 5 includes a separate literature review, summary of experiments, results and analysis, and conclusions section.

Chapter 6 contains the overall conclusions made and future recommendations for potential research resulting from the present research.

1.2 Background

Currently, glass fiber used for optical communication systems are silica fibers. The reason that silica is the primary choice for an optical waveguide is that silica fibers have achieved their theoretical predicted minimum optical loss of 0.15 dB/km at visible wavelengths. These low losses allow optimum data transmission between our telecommunication devices. However, silica fibers demonstrate high loss factors for transmission of infrared (IR) light (800dB/m at λ=2.94μ) [Harrington, 2007]. IR transmission is an enabling technology for surgical and defense applications. Many researchers suggest that the most promising optical waveguides to replace silica fibers are Heavy Metal Fluoride Glasses (HMFG) that can demonstrate losses as low as 0.01dB/m for near IR wavelengths. ZBLAN, a particular type of HMFG, has a theoretically predicted ultra-low optical loss of 0.001 dB/km in near-infrared regions [Varma, 2002]. Loss as low as 0.1dB/km have been demonstrated in small segments of ZBLAN fibers. Prior to recent research the losses for HMFG fibers were only in the range of 1-10 dB/km with a reported low of 0.65 dB/km [Varma, 2001]. The primary cause for these higher than predicted losses is believed to be the scattering of the light from microcrystals formed during glass synthesis as well as fiber drawing. A discovery in 1994 showed that microcrystal formation in ZBLAN could be suppressed when processed under

microgravity [Workman, 1995]. This breakthrough opened up the possibility that ZBLAN glass can achieve its theoretical ultra-low loss values approaching 0.001dB/km.

Microcrystal formation and crystal growth are extensively documented in conventional materials science texts. There are two possible methods for microcrystal formation: heterogeneous or homogeneous nucleation. Heterogeneous nucleation is the lower energy nucleation formed from contamination of the glass melt from the processing container. The processing container contamination allows there to be nucleation sites for the microcrystals to be formed. On the contrary, homogeneous nucleation is the higher energy solidification state where gravity-driven density segregation is believed to be the main cause. These two instances cannot be removed during the conventional processing of HMFG fibers under terrestrial conditions, therefore, formation of the microcrystals cannot be avoided. This is the limiting factor with the development of an ultra-low loss optical fiber. The reduced gravity environment that space possesses offers the potential for container-less processing of the HMFGs and fibers in the absence of strong gravitational force. This abridged state of gravitational force offers numerous advantages during both the high-temperature process steps involved in bulk HMFG syntheses and fiber drawing [Varma, 2001]. Fiber drawing can be easily done in space since the glass preform is reheated to its viscous state not its molten state. When HMFGs are synthesized corrosive and toxic fumes are emitted from the melt [Varma, 2001], which is not a desired process for space conditions. Therefore, fiber drawing is much more suitable for microgravity experiments. The process of fiber drawing consists of a 'preform' glass that is heated beyond its glass transition temperature (T_g) but below its crystallization temperature (T_x). The glass transition temperature (T_g) is when the material becomes soft,

such that the material is in a semi-viscous state. The crystallization temperature (T_x) is when solids (crystals) start to form in the material. The preform is the starting glass material of the fiber drawing process, which is the same consistency and geometry (core and cladding) of the final fiber product. The core is of a similar glass consistency contains a doping agent to lower the refractive index, which contains the transmission signal within the core. The difference between T_x and T_g is known as the working temperature range (ΔT). A large working temperature range makes for an easy material to draw into fiber form. ZBLAN has a very narrow working range, resulting in a difficult material to draw into a fiber. Due to the narrow working range, crystallization is prevalent in this material, which results in higher transmission loss. Overall, the microgravity environment of space can reduce crystallization in the glass during its reheating for fiber drawing.

In this document the physics and materials science related to the fabrication of ZBLAN in microgravity will be presented along with hypotheses of why microgravity fabrication is promising. The analytical and experimental tools for the verification of the hypotheses will be presented. Multiple ZBLAN samples were processed on a parabolic flight aircraft. These samples were subjected to tailored temperature schemes that induce crystal growth. It is essential to point out that the ZBLAN material was not drawn into fiber form in this study. The focus of this study is on the heating and cooling phase of the fiber drawing process; therefore multiple 'preform' ZBLAN samples were heated and cooled in a microgravity environment. The samples were post processed using a range of optical microscopy and Scanning Electron Microscopy (SEM) techniques. The

experimental description and results are presented in subsequent sections. Finally, the effect of crystal formation on mechanical behavior of a ZBLAN fiber will be addressed.

1.3 ZBLAN

HMFGs are excellent materials for the use in many IR-laser applications, such as fiber optics, fiber amplifiers, and lasers for cutting, drilling, and surgery. These fibers also show promise in applications such as nuclear radiation resistant links, high-capacity multiplexed fiber optics systems, and non-linear optical applications [Tucker, 2004]. Fluorozirconates, a subset of HMFGs, were discovered in 1974 by researchers at the University of Rennes, France [Workman, 1995]. In the 1980's the majority of fluorozirconate glass formulations tapered off to a very few practical applications. The most promising are formulations from the ZrF_4-BaF_2-LaF_3-AlF_3-NaF (ZBLAN) family with a molar composition of 53% ZrF_4, 20% BaF_2, 4% LaF_3, 3% AlF_3, and 20% NaF, which is the most stable glass for optical fiber applications. This formulation was first reported by researchers at the Furukawa Electric Co. in 1981 which led to a U.S. patent number 4,445,755 in May of 1984 [Workman, 1995]. As discussed earlier, the main advantage of ZBLAN glasses over other glasses, such as silica, is its superior infrared transmissibility. The drawbacks are that it is a fragile fiber and is sensitive to moisture. The optical transmission spectrum for a ZBLAN fiber is from 0.3 μm in the UV to 7 μm in the IR region. ZBLAN has a low refractive index of 1.5, a low glass transition temperature (T_g) of 260 °C, and a low/negative temperature dependence of refractive index (dn/dT) [Harrington, 2007].

The main obstacle with ZBLAN glass in attaining ultra-low losses is the problem of devitrification (crystallization). HMFGs have a narrow working temperature range and

the viscosity is a strong function of temperature [Workman, 1995]. The rates of nucleation and crystal growth in the glass depend on the viscosity, which makes these glasses unstable and prone to crystallization. The viscosity of ZBLAN at the drawing temperature is between two to five poise, thus making it difficult to obtain fibers from their preform melts without crystallization.

Other formulations of ZBLAN include the percent composition of LaF_3 (Lanthanum Fluoride) of four and eight percent mole. Another common composition is replacing LaF_3 with GdF_3 (Gadolinium Fluoride) to form ZBGAN glass. This can also be synthesized in four and eight percent mole composition of GdF_3 [Harrington, 2007]. Both of these are still in the HMFG category.

The bond strengths are lower in ZBLAN glass than in silica glass due to the fluoride ion being singly charged; which leads to a significantly lower melting temperature and greater thermal expansion. The weaker bonding leads to greater infrared transparency and higher chemical reactivity. This suggests that the infrared edge of ZBLAN glass is much longer that that of silica glass, but stability and hardness of ZBLAN is much lower than that of silica. Consequently, ZBLAN fibers are the most promising fibers to replace silica fibers for IR transmission.

1.4 Microgravity

Microgravity is a term that can be used colloquially to mean the lack of gravity. In a scientific sense microgravity implies an acceleration level much less than unit gravity of 9.8 m-s^{-2}, more specifically on the order of 10^{-6}g (μg). A state of true microgravity is when gravitation has been reduced to near zero. Microgravity can be achieved in an

orbiting spacecraft, suborbital rocket (sounding rocket), and a parabolic flight aircraft. An example of the parabolic flight profile can be seen in Figure 1.1.
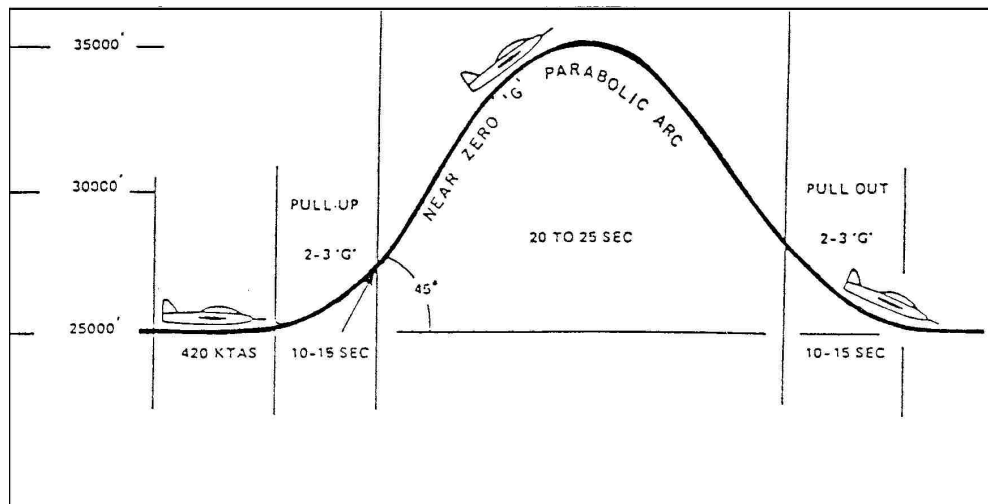
Figure 1.1: Parabolic flight profile [Varma. 2001].

Each method provides a varying duration and magnitude of reduced gravity. The space shuttle or the International Space Station can achieve days of microgravity but is the most expensive means of reduced gravity. The magnitude of microgravity can vary depending on the mission since the firing of thrusters and routine exercise by the astronauts can introduce micro-jitter [Kundrot, 2001]. A suborbital rocket, also known as a sounding rocket, can provide between three to nine minutes of microgravity but is also costly. Decreasing in price as well as microgravity time is a parabolic flight aircraft that can achieve up to 25 seconds of reduced gravity. Lastly, a drop tower can achieve a state of free fall, such that the only force acting on the body is its weight. However, the duration of a drop tower is on the order of a few seconds. These methods allow researchers to determine the effect of gravity on certain processes.

1.5 Overview of Research

The objective of this research is to understand the role that gravity plays on the formation of microcrystals in ZBLAN glass. Many researchers have conducted studies on crystal growth under microgravity [Tucker, 2004; Kundrat, 2001; Regel, 1990; Voloshin, 2002; Varma, 2001; Dunkley, 2004]. While these researchers have studied ZBLAN, protein crystals, and semiconductor growth under microgravity, all have noticed that devitrification processes are suppressed in microgravity. These studies used sounding rockets, parabolic flight aircraft and even a drop tower to achieve free fall. The authors also noticed that crystal growth was increased during times of high accelerations [Varma, 2001]. When using the parabolic flight aircraft there are periods of approximately 2-g accelerations. Varma et al. detected twice as many crystals formed during the period of high acceleration as terrestrial processed fibers. While there are a few qualitative postulates on why crystal growth in a vitreous material is suppressed in microgravity, there has not been any hypothesis verified with analytical models and/or experimental observations. The goal of this research is to investigate the mechanisms that govern crystal growth and how they may be affected by gravity or lack thereof. The hypothesis of this study is that processes of mass transfer (diffusion and convection) are the mechanisms governing crystal growth suppression in microgravity. The effect of crystallinity on wrapping ability will also be reported with regards to durability and handling ability of fibers.

CHAPTER 2 – Background Information and Literature Review

This section provides background information regarding crystal growth in vitreous materials and microgravity research particularly as it relates to ZBLAN. It begins with a short description of different types of fibers used for infrared optics and continues with many articles describing crystal growth in microgravity and in ZBLAN.

2.1 Literature Review

The article entitled, "Infrared Fiber Optics" by J. Harrington [2007] provides useful insight into the general area of infrared fiber optics. The infrared range on the electromagnetic radiation spectrum has a variety of applications, including night vision, thermography, tracking, heating and communications. Infrared optical fibers transmit radiation with wavelengths greater than approximately 2 μm. The first IR fibers were fabricated in the mid-1960's from chalcogenide glasses such as arsenic trisulfide with losses in excess of 10 dB/m. During the mid-1970's the need for a more efficient IR fiber arose. The purpose for the more efficient IR fiber was to link broadband, long wavelength radiation to remote photodetectors in military sensor applications. Along with military applications, a demand for a flexible fiber delivery system for transmitting CO_2 laser radiation in surgical applications became apparent. To meet these demands HMFG and polycrystalline fibers as well as hollow rectangular waveguides were developed. These HMFG fibers were not on par with that of conventional silica fibers but were, however, useful in lengths less than 2 to 3 meters for a variety of IR sensor and power delivery applications. IR fiber optics can be divided into three broad categories: glass, crystalline, and hollow waveguides. Within these three categories there are

subcategories based on either the fiber material or structure or both. The IR fiber

categories and subcategories can be seen in Table 2.1.

Table 2.1: *Categories of IR fibers with examples [Harrington, 2007].*

Main	Subcategory	Examples
Glass	Heavy metal fluoride - HMFG Germanate Chalcogenide	ZBLAN – $(ZeF_4-BaF_2-LaF_3-AlF_3-NaF)$ GeO_2-PbO As_2S_3 and AsGeTeSe
Crystal	Polycrystalline - PC Single crystal - SC	AgBrCl Sapphire
Hollow Waveguide	Metal/dielectric film Refractive index < 1	Hollow glass waveguide Hollow sapphire at 10.6 μm

Both the optical and mechanical properties of IR fibers remain inferior to that of

silica fibers (in the visible wavelength domain). Thus, due to high transmission loss (and

consequent heat generation), the use of IR fibers is limited primarily to non-

telecommunication, short-haul applications only requiring a few meters of fiber rather

than an extensive length of fiber. An exception to this are fluoride glass fibers which can

have losses as low as a few dB/km. IR fibers are significantly weaker than silica fiber

which results in a more fragile fiber. This aspect impedes the acceptance of IR fibers and

restricts their use to a smaller area of IR technology, such as chemical sensing,

thermometry, and laser power delivery. A key feature of current IR fibers is the ability to

transmit wavelengths longer than most oxide glass fibers. In certain instances the

transmittance of the fiber can extend beyond 20 μm. Typical applications do not require

the delivery of radiation longer than roughly 12 μm. There is a wide variation in range of

transmission for the different IR fibers and there is significant extrinsic absorption, which

degrades the overall optical response. Most of the extrinsic bands can be attributed to

various impurities. There are many motivations for the development of IR fibers and they

stem from many proposed applications. The below table describes these current and
future applications and the associated candidate IR fiber that will best meet the need.

Table 2.2: Examples of IR fiber candidates for various applications [Harrington, 2007].

Application	Comments	Suitable IR Fibers
1. Fiber optic chemical sensors	Evanescent wave principle –liquids	AgBrCl, sapphire, chalcogenide, HMFG
2. Fiber optic chemical sensors	Hollow core waveguides – gases	Hollow glass waveguides
3. Radiometry	Blackbody radiation, temperature measurements	Hollow glass waveguides, AGBrCl, chalcogenide, sapphire
4. Er.YAG laser power delivery	3 μm transmitting fibers with high damage threshold	Hollow glass waveguides, sapphire, germinate glass
5. CO_2 laser power delivery	10 μm transmitting fibers with high damage threshold	Hollow glass waveguides
6. Thermal imaging	Coherent bundles	HMFG, chalcogenide
7. Fiber amplifiers and lasers	Doped IR glass fibers	HMFG, chalcogenide

A chalcogenide is a chemical compound consisting of at least one chacogen ion and at
least one more electropositive element. The high refractive index of chalcogenide fibers
is ideal for chemical sensing via evanescent wave coupling of a small portion of the light
from the core into an IR absorbing medium. From the table previously mentioned it can
be noticed that the hollow waveguides are an ideal candidate for laser-power delivery at
all IR laser wavelengths. The air core of these special fibers or waveguides provides an
inherent advantage over solid-core fibers whose damage threshold is frequently very low
for these IR transmissive materials. For the application of measuring temperature
through the simple transmission of blackbody radiation, IR fibers such as Ag halide,
chalcogenide, and hollow waveguides, are excellent candidates for measuring
temperatures below 50°C, since the peak of room temperature blackbody radiation is
approximately 10 μm.

2.2 Microgravity Experiments

Regel et al. [1990] described several crystallization experiments carried out in the microgravity environment of the Russian Mir orbital complex, analogous terrestrial experiments and a study of the resulting microstructure. This included direct crystallization of Al-Ni (Aluminum-Nickel) eutectic alloys at varying rates, growth of GaSb crystals of specific conductivity and crystallization of hydroxyapatite and calcium sulphate from aqueous solutions under microgravity.

The ground-based experiments were done by means of the Crystallizer CSK-1 at the Institute of Space Research of the U.S.S.R. Academy of Sciences. The method of controlled cooling for direct crystallization was at 0.3 and 1.5°C/min, which corresponds to a crystallization rate of 2 and 20 cm/hr. The space experiments were done in July 1987 on-board the Mir orbital complex and two experiments were completed using the Crystallizer CSK-1.

Both terrestrial (ground based) and space samples were cut by means of a diamond disc in order to examine the internal order of the specimens. Micro-sections of metallographic specimens were prepared by mechanical polishing and images were developed with the help of a SEM (Scanning Electron Microscope). Multiple SEM images were obtained from longitudinal and lateral sections. During solidification, one of the phases ($NiAl_3$, Nickel Alluminide, intermetallide) crystallized in the form of fibers located parallel to the sample axis. It was postulated that differential densities of the nickel and aluminum gravitational convection breaks the uniformity of the structure.

The results from the ground based and space based testing at the two cooling rates are as follows. In both tests a fiber-type structure was formed with a uniform distribution

of NiAl$_3$ intermetallide fibers in the Al matrix. The interfiber distance of the eutectic

structure was measured. The measurements are provided in Table 2.3.

Table 2.3: *The interfiber distance for both cooling rate and Space and Earth tests [Regal, 1990].*

Conditions of Crystallization	Space	Earth
	λ [μm]	
Sample I (rate 0.3˚C/min)	0.85	0.78
Sample II (rate 1.5˚C/min)	0.6	0.53

A slight coarsening of the eutectic structure in microgravity was observed from

these results. In the space samples a complete absence of the region of competing growth

was observed in the beginning of the sample (typically, under gravity conditions, at the

beginning of the sample there are eutectic grains with a disorientated structure). These

tests demonstrated the possibility of obtaining eutectic alloys with a perfect

microstructure under microgravity conditions.

Additional experiments by Regel et al. [1990] describe the crystallization of GaSb

under microgravity. While the ability to grow such crystals in microgravity was

demonstrated, there were no major microstructural differences between terrestrially

grown samples and those grown in microgravity. However, resistivity values measured in

the space-grown samples were more uniform.

The third set of experiments done by Regal et al. included the works on mass

crystallization from aqueous solutions under microgravity performed on orbital stations.

This section of their research was carried out to study the features of the particle

aggregation and solid-phase spatial texture formation during crystallization of calcium

sulphate and phosphate from aqueous solutions under microgravity. The only reported

difference was the creation of larger aggregates (sediments) with almost zero-buoyancy from the microgravity experiments. This article describes the crystallization of different systems under microgravity and how they compare to that of crystals grown terrestrially. The fundamental difference noted is that micro-crystal growth is suppressed in microgravity as opposed to those grown under terrestrial conditions. The work by Regal et al. is useful to this research as it discusses how zero-buoyancy from microgravity experiments yields zero crystal growth. This shows the connection between buoyant convection and crystal growth. By suppressing buoyant convection, crystallization is also suppressed.

A review article by Kundrot et al. [2000] provides a detailed summary of microgravity and macromolecular crystallography. Among the several topics discussed are the growth of macromolecules (complex molecules such as industrial enzymes), variations of micro-g conditions in different space flight experiments, and plausible explanations for differences created by the micro-g environment. The article provides an introduction to each topic and delineates how it's used and why it is useful to researchers. Macromolecular crystallography is a multidisciplinary science involving the crystallization of a macromolecule or complex of macromolecules, followed by X-ray or neutron diffraction to determine its three-dimensional structure [Kundrot, 2000]. Neutron diffraction is a process in which neutrons are used to determine the atomic and/or magnetic structure of a material. The purpose for understanding the structure is that it provides a basis for the development of new macromolecules (e.g. more efficient industrial enzymes) and structure guided design of drugs, insecticides, and herbicides.

An ideal environment for biological crystal growth has been conceived as a reduced acceleration environment of an orbiting spacecraft since buoyancy-driven convection and sedimentation are significantly reduced. The perfect combination for a microgravity experiment is one that is small and requires simple equipment and minimal intervention. Thus allowing larger crystals to grow without interference. The larger the crystal is the easier it is to inspect via diffraction techniques. An ideal crystal for X-ray diffraction studies is one that has dimensions on the order of 100 μm.

The article describes the many factors that affect microgravity in an orbiting spacecraft, such as residual accelerations. Residual accelerations arise from several sources and can be characterized as quasi-steady, oscillatory, or transient. Quasi-steady accelerations with a frequency less than 0.01Hz result from atmospheric drag, venting of air or water, and the gravity gradient across the spacecraft. Gravity gradient describes the forces that arise due to the tendency of different parts of the vehicle to follow different orbital trajectories. Parts of the aircraft that are not on the same trajectory as the center of mass experience a residual inertial force. Gravity gradient forces produce accelerations of about 0.1-0.3 μg per meter of displacement from the center of mass. The amount of atmospheric drag depends on the altitude of the orbiting vehicle. Atmospheric drag exerts an acceleration of around 5 μg at an altitude of 250 km (depends greatly on the attitude/orientation). The orbital drag for the International Space Station is expected to be less than 1 μg. Oscillatory accelerations result from on-board activities such as crew exercise, the operation of experimental and life support equipment, and harmonic structural vibrations of the spacecraft itself. The frequencies are characterized as being

on the order of $0.01 < f < 300$ Hz. Additionally, larger magnitude oscillatory accelerations on the order of 10-1000 µg and are referred to as g-jitter.

The article also describes a possible explanation as to why microgravity may affect crystallization. Overall, microgravity is not expected to directly affect the interatomic and inter-molecular forces. This is evident from the fact that the boiling and freezing temperature of materials, which are related to interatomic forces, are not affected at microgravity. Empirical observations, however, indicate that nucleation times are significantly longer and overall growth rates are slower than on Earth. For instance, in microgravity a small crystal (or particle) is subject to Brownian motion as on the ground, but unlike the ground case, there is no acceleration inducing larger particles to settle down (sedimentation). The transition from Brownian motion to sedimentation occurs at a size of approximately 1µm. A growing crystal in zero gravity will move minimally with respect to the surrounding fluid. Another factor influencing the effects of microgravity on macromolecular crystal growth is based on the concept of the depletion zone. As growth units leave solution and are added to the crystal, a region of depleted solution (lower saturation level) is formed. Typically, this solution has a lower density than the bulk solution and will convect upward in a 1g field as seen by Schlieren photography (a process that is used to photograph the flow of fluids of varying densities [Kundrot, 2000]). Under microgravity the buoyant convection and sedimentation are severely attenuated rather than eliminated. This may explain the slower crystal growth rate observed in microgravity and provide impetus for suppression of crystallization in a microgravity environment.

The initialization of a crystal (primary growth) involves solute-solvent/precipitant interactions. Assuming microgravity to have a direct effect on this implies that gravity significantly affects the bond energies and assumes that gravitational forces at the molecular scale are comparable in magnitude to the intermolecular forces. As mentioned earlier, if this was true, other physical properties such as boiling and freezing points would be affected as well. Overall, this occurrence has not been observed to date.

In addition, the numbers, size and location of crystals can be used to examine the effect of microgravity upon crystal nucleation. The overall affect of microgravity upon nucleation behavior seems to be macromolecule and hardware-specific. Researchers have reported reduced crystal numbers in vapor diffusion experiments and increased crystal numbers in batch experiments in microgravity.

The article describes secondary nucleation and how microgravity can affect this process. Secondary nucleation is the formation of nuclei in solutions that already contain growing crystals. In a 1g field and a crystal of size about 10-100 μm, buoyancy-driven flows develop which not only maintain a high growth rate but may also produce increased secondary nucleation. In microgravity the reduction of buoyancy driven flows is expected to reduce this effect. However, there is insufficient experimental evidence to indicate the effect of microgravity on secondary nucleation.

The article also describes the macro effects of crystallography under microgravity, specifically the macro effects of nucleation. As nuclei grow, they eventually reach a size where their movements in solution is dominated by sedimentation rather than Brownian motion. After moving through the solution the particle will eventually settle where it can continue to grow. The contact with the boundary wall often

results in the prevention of crystal growth. However, crystals that stay suspended in solutions as in microgravity grow free of the boundary restriction and exhibit a more uniform shape. The sedimentation is greatly reduced in microgravity but sudden movements can occur due to transient accelerations. Overall, the great detail on convection/nucleation under microgravity provided in this paper is essential to this research. The article stipulates an in-depth look into the macromolecular physics of the system in an attempt to understand the phenomenon of crystal suppression in microgravity. This generalized discussion can offer valuable insight to the specifics of this research.

Voloshin et al. [2002] reported on the study of a Te-doped (Tellurium) GaSb (Gallium Antimonide) single crystal grown under microgravity aboard a Chinese spacecraft in 1992. The experiments done in this article were aimed at the growth of a dislocation-free homogeneous crystal and the study of the characteristics of the dopant (Te) distribution in space-grown crystals. This report contributed more detail on the specific features of the defect formation and dopant distribution by highly sensitive X-ray diffraction methods (single-and double-crystal X-ray topography) in order to establish the consequences of crystal growth in microgravity. Microgravity was reported to result in low dislocation density and absence of zonal inhomogeneity in the Te concentration. Another interest of the study was to establish the working growth mechanisms and their influence on the structures perfection. The authors also discussed how microgravity allows crystals to grow without boundary influences from the container walls. The advantage of crystal growth in space is associated with the fact that suppression of natural, thermo-gravitational convection in weightlessness allows one to grow crystals

without zonal inhomogeneity (uniform concentration of Te allows lattice parameter to be more uniform throughout and reduced dislocation defects from $10^4/cm^2$ to $10^2/cm^2$.) When the crystal is free of the boundary of the container walls the crystal will also, theoretically, be less influenced by impurities.

However, as discussed in the article, the first experiments in space showed that the existence of a free melt surface increases the significance of Marangoni convection provided by the surface-tension gradient caused by the temperature gradient. The Marangoni effect is the mass transfer along an interface between two fluids due to surface tension gradient, and when caused by temperature dependence the Marangoni effect is referred to as thermocapillary convection [Voloshin, 2002]. At a high intensity of the convective Marangoni flow, the crystal growth becomes unstable, which results in striation in the growing crystals.

In addition to semiconductor and single crystal growth, protein crystals are also affected by gravity. The article, "Protein Crystal Growth of Ribonuclease A and Pancreatic Trypsin Inhibitor aboard the MASER 3 Rocket" by Sjölin et al. [1991] also provided information relevant to our research. Many of the world's space agencies suggest that crystals of biological macromolecules may grow to larger size and with better order under microgravity conditions. The structure of biological macromolecules, especially that of proteins have been used in a wide variety of industrial studies. Industrial applications include new proteins with altered properties, molecular design of new pharmaceuticals, development of synthetic vaccines and development of biochip technology. Sjolin et al. [1991] report that crystals grown in space were considerably larger than crystals grown under identical conditions on earth. There is also evidence that

a microgravity environment can improve crystal perfection as evident from an increase in

X-ray diffraction power down to 1.06Å (compared to 1.26Å for terrestrial crystal growth.

Experiments done in this research to study the effects of microgravity on protein crystal

growth were designed and executed under the microgravity sounding rocket program of

the Swedish Space Corporation (SSC). The Material Science Experiment Rocket

(MASER) provided acceleration levels below 10^{-4}g for approximately seven minutes.

This information is helpful in this study as it shows that micro-inhomogoneities are not

only suppressed in a specific type of material but also observed in the growth of protein

crystals.

Thus, the journal article, "Solidification under Microgravity" [Dhindaw, 2001]

describes various areas of microgravity research including biotechnology, combustion

science, material science and fluid physics. The main focus of this research is the studies

of materials science, specifically solidification science. This area of study also helps in

the application of gravity-dependent fluid phenomena in other microgravity science

disciplines. The research programs, described in the article, are as follows:

- The effect of convection on morphological stability during coupled growth in immiscible systems.
- Processing of eutectics in microgravity.
- Melt interface stability during solidification studied by Seebeck coefficient variation in MEMPHISTO facility.
- Interface undercooling, solidification velocity and nucleation,
- Isothermal dendritic growth experiment to study undercooling effect on growth kinetics.
- Pushing/engulfment transition in insoluble particles dispersed material systems.
- Macro-segregation in alloys.

The article begins by characterizing solidification of monotectic transitions

(Liquid to Solid+Liquid). The monotectic reaction occurs in many immiscible systems

and processing in microgravity should make it possible to produce an aligned fibrous composite structure. To prove this, a convection-free environment is compulsory and requires directional solidification of a range of alloy compositions at several solidification rates. To rid the experiment of sedimentation effects a microgravity environment is sought out. Experiments were carried out on the space shuttle during the Life and Microgravity Spacelab (LMS) mission on Al-In (Aluminum-Indium) alloys in AlN (Aluminium Nitride) crucibles. The experiments showed that solidification of monotectics under microgravity is complicated due to the wetting behavior and its strong influence on the solidification.

Nucleation behavior under microgravity experiments were also described in this article. The microgravity experiments involving nucleation behavior have shown a continuous transition from a purely equiaxed to an anisotropic solidification microstructure as a function of solidification rate and the local temperature gradient. Equiaxed crystals are crystals that have axes of approximately the same length and have more planes on which to slip and thus have a higher strength and ductility. The experimental study described here included the effect of undercooling on kinetics of dendrite growth. Growth of dendrites is one of the commonly observed forms of solidification encountered when metals and alloys freeze under low thermal gradients. In engineering alloys, dendritic morphology directly relate to important material responses and properties. Experiments show that gravity-induced convection controls dendritic growth in the lower supercooling range typical of metal alloy castings. The isothermal Dendritic Growth Experiment (IDGE) from a NASA sponsored series of Space Shuttle microgravity experiments, was designed to grow and photograph dendrites in the absence

of convective heat transfer for fundamental tests of dendritic growth theories. It was stated in the article that further investigations need to be made for adequate dendritic growth conclusion to be made. The paper presented basic theory that relates temperature gradients, velocity of solidification front (or crystal growth), extent of undercooling and relevant material properties. Kinetics of crystal formation and growth are also available from the field of environmental sciences (colloid and surface chemistry). Overall, this study provides pertinent information relevant to this research.

Hiemenz and Rajagopalan [1997] discuss the factors that relate to the kinetics of coagulation. Coagulation in colloid chemistry is a process in which colloids (substances evenly dispersed in another solution) form agglomerates. The first issue affecting coagulation kinetics is that for asymmetrical particles. The collision of asymmetrical particles has a higher probability than that predicted for symmetrical particles. This can be better understood from the aspect that the diffusion coefficient is most influenced by the smaller dimensions of the particles. Another issue of coagulation kinetics is that the frequency of collisions is expected to be greater in a polydispersed system than that of a monodispersed system. The last issue presented by Hiemenz is that of the presence of velocity gradients in the system may also increase the rate of coagulation. The ratio of the probability of a collision induced by a fluid velocity gradient (*dv/dx*) to the collision probability under the influence of Brownian motion is shown in the below equation.

$$\frac{k_{r,Flow}}{k_{r,Diff}} = \frac{\left[\eta(2R_s)^3\left(\frac{dv}{dx}\right)\right]}{(2k_BT)}$$

For particles of different sizes, $2R_s$ should be replaced with $R_{s,1} + R_{s,2}$ where R_s is the radius of the particles, η is the viscosity, k_B is the Boltzmann constant, and T is the temperature

The paper also discussed the topic of macrosegregation; microscopic casting defects caused by the redistribution of solute in the matrix during solidification. Thus far there exist a multitude of numerical and analytical models describing the macrosegregation phenomena, but there is no reliable experimental data to validate these models. While experiments conducted in microgravity show that convection strongly affects macrosegregation, they do not provide quantitative data to validate the various models. The specificity of this work by Dhindow results in viable information that will be used to investigate the phenomenon of crystal suppression in microgravity.

2.3 Microgravity Experiments on ZBLAN

This section describes research related to both microgravity and ZBLAN fibers. The article, "Effect of Gravity on Crystallization in Heavy Metal Fluoride Glasses Processed on the T-33 Parabolic Flight Aircraft," by S. Varma et al. studies the effect of gravity on crystallization and the optical degradation of HMFG during the heat treatment for fiber drawing. The HMFG used in this research was synthesized on the ground and then heat treated in microgravity. Similar to future work conducted for the present study Varma et al. utilizes a parabolic flight aircraft. Specifically Varma et al. used a modified T-33 fighter jet, in which the back seat was removed to accommodate the experimental payload. The ZBLAN fibers were synthesized prior to being placed on board the aircraft. Two compositions were synthesized, one with a LaF_3 percent composition of 4% (ZBLAN-L4) and one of 8% (ZBLAN-L8). Cylindrical preforms of about 6 mm (D) x

50 mm (L) were softened by heating their center, lengthwise, in a customized furnace and pulling edges of the fiber outwards with uniform speed. The drawn fiber was cut into 40 mm long pieces and were individually sealed in silica tubes of 3 mm (OD) x 50 mm (L). This process describes a fiber drawing processes that is related to the to the fiber puller that will be used for this research. The main differences between the work by Varma et al. and this research is that they focus primarily on just the heat treating of the fiber in microgravity and not the entire fiber pulling process in microgravity. The fibers are pre-drawn in 1-g then placed on board the aircraft and a automated mechanism places the fiber in a furnace during the microgravity duration of the flight. Four processing temperatures were used in the range of 370-500°C. Four samples were processed in microgravity and four others were processed during the 2-g portion of the flight path. The microgravity time achieved was about 20-25 seconds. Microstructural characterization of the samples, before and after microgravity processing was done by a back scattered electron imaging technique using a JEOL-820 Scanning Electron Microscope operated at 15 kV with a beam current of 1-12 nano-amperes.

The results of these studies showed that the ZBLAN-L4 glass samples heat treatment at 370°C for 20 seconds in microgravity did not produce any crystallization, as indicated by the SEM micrograph. However, processing of the same composition fiber at 370°C for 20 seconds in 2-g acceleration showed crystallization of two phases at the surface. Meaning, there were two distinct crystal growth areas shown by the SEM micrograph. This was also observed in ZBLAN-L4 samples processe at 400°C. However, samples processed at temperatures of more than 420°C in microgravity didn't

show any crystallization. These results show that gravity enhances crystallization in HMFGs during their heat treatment at crystallization temperatures.

The outcome of this study confirms that gravity has a strong role in the crystallization of ZBLAN fibers. The conclusions indicate that in 2-g accelerations more crystals are grown than that in 1-g, alternatively no crystals are found in a near 0-g environment. The work published by Varma on board the T-33 aircraft is useful to the objectives of this study in the sense that they demonstrated how gravity affects crystal growth in ZBLAN fibers. This work very specifically studied the effects of the heat treatment process of fiber drawing of the fibers rather than completely drawing the fibers in microgravity, as will be done in the current research. However, they did not provide any discussion on why they believe this phenomenon is occurring. The authors suggest that the 20 sec microgravity time was not enough time to fully characterize the crystal growth process.

In addition, continued word completed by Varma et al. titled, "Effect of Microgravity on Crystallization in Heavy Metal Fluoride Glasses Processed on the CSAR-I Sounding Rocket" was accomplished to fill the holes that the authors felt were lacking in the past research. The objective of this article was the same as in the previous article but this experiment took place on the CSAR-I sounding rocket. Previous testing conducted by these researchers on the T-33 parabolic flight aircraft show that gravity enhances crystallization in HMFG, these results were not considered conclusive due to the short microgravity processing time of only 20 seconds. The CSAR-I sounding rocket, however, provides an opportunity to process HMFG samples in microgravity for a longer duration. The payload for this experiment was modified to fit the sounding rocket

25

dimensions. The ZBLAN samples were synthesized and drawn into a fiber prior to being placed on board the sounding rocket similar to previous work by this author. The CSAR-I sounding rocket provided microgravity for a duration of five minutes. The processing temperatures ranged from 325-400°C. Microstructureal characterization of the HMFG samples was carried out after being removed from the payload. Back scattered electron imaging technique using a JEOL-820 scanning electron microscope operated at 15 kV with a beam current of 1-12 nano-amperes was used for the post characterization. The samples appeared clear, transparent and free of defects after the microgravity processing. Tiny bubbles were sometimes observed along the axis in some portions of the glass preforms and these areas were cut off and discarded before the samples preparation for further processing.

The samples processed in microgravity showed no evidence of crystallization but on the other hand the samples processed on the ground for the same duration and heating profile showed extensive crystallization at the surface. These results imply that microgravity aides in reducing crystallization, which results in less optical degradation. Past research by the authors show that HMFG samples processed in higher levels of gravity and higher temperatures yield even more crystal growth in the samples. Overall, these experiments show comparable results obtained by other microgravity researchers as well as the authors past experiments. This article relates to the current research as it indications that a longer duration of microgravity can be achieved and crystallization is still suppressed. It is noted that the authors, in this study, pre-processed the fibers before being placed on board the rocket as opposed to drawing the fiber in microgravity.

In addition to the previous article by Varma et al. the authors continued their study on the CSAR-II sounding rocket. The same payload used for the CSAR-I sounding rocket experiments was utilized again for the CSAR-II sounding rocket. The basic design and operation remained the same, but many modifications were done to the CSAR-I payload to make it more suitable for the CSAR-II sounding rocket. The main difference is that the CSAR-II payload was aimed at processing HMFG samples at different temperatures in the narrow range of 300-320°C. This required excellent control, stability, reproducibility and uniformity in temperatures across the furnaces and the glass samples. Some modifications were based on previous malfunctions observed from the CSAR-I sounding rocket experiments. A reduction in overall weight of the payload was done in order to improve the microgravity duration for the CSAR-II rocket flight. Each HMFG sample was typically 15-20 mm (L) x 4 mm (D). The sample temperature data was collected via six thermocouples, which were attached to the sample holders. In addition to the thermocouples, electronics to attain the information were added to the control system.

The experiments consisted of HMFG samples synthesized in the ZBLAN glass system using conventional melt-quenching process. The ZBLAN glass samples were synthesized, again, in the same manner as the past two publications. The sounding rocket achieved a microgravity period of about seven minutes. The results from this research simply strengthened the author's prior conclusions, that crystal growth is suppressed in microgravity in ZBLAN fibers. The samples were processed at a temperature of 310°C onboard the sounding rocket and compared to the same processing temperature on the ground. Overall, the sample showed no crystallization in microgravity levels and crystal

27

growth on the ground based experiments. Similar to other conclusions the sample processed during the high acceleration period of the flight showed broad crystallization. A recommendation from the authors is that future rocket experiments should ensure that HMFG samples should be rapidly cooled below the critical temperature before the rocket's re-entry to minimize adverse effect of high gravity exposure. These conclusions provide adequate evidence that gravity is the main contributing factor to crystal growth in ZBLAN fibers. The author's provide no discussion to explain the mechanisms governing this phenomenon.

Other researchers that are interested in ZBLAN glass processed under microgravity are Tucker et al. For the experiments conducted in the article, "Effects of Gravity on ZBLAN Glass Crystallization," fibers were prepared and flown on board the KC-135 aircraft and on board a suborbital rocket. Fibers were heated to the crystallization temperature in unit gravity and in reduced gravity. The temperature of the experiments were chosen as 370°C and the crystallization peak from differential thermal analysis of 375°C. On board the KC-135, 20 samples of ZBLAN were heated in the furnace at 400°C for 20 seconds during the low-gravity portion of the parabola. For comparison purposes the same heating technique was completed on the ground. The fibers were heated to 400°C for 6.5 minutes during the low-gravity portion of the suborbital rocket. The fibers were then processed using X-ray diffraction and electron microscopy. Another experiment was performed to adequately determine if the reduced gravity samples reached the same temperature as the ground samples. Both samples that were flow in microgravity and on the ground reached the same temperature between 365°C to 370°C which is very close to the temperature of maximum crystallization.

The authors observed crystal formation in the terrestrial processed fiber, which was apparent in all samples processed on the ground. As for the specimens subjected to microgravity there was no presence of crystallization. X-ray diffraction analysis of the ground processed samples showed the crystal structure to be β-BaZrF$_6$. β-BaZrF$_6$ is a metastable crystal with an orthorhombic structure. X-ray diffraction analysis of the flight samples showed an amorphous structure showing no crystallinity.

Likewise, the results from this research were similar to results reached by Varma et al., gravity does play a role in the crystallization of ZBLAN glass. However, Tucker et al. does postulate at why these results were obtained. The authors believe that the reason crystal growth is suppressed in microgravity is that ZBLAN behaves as a non-Newtonian fluid. A number of glass-forming liquids have been shown to exhibit shear thinning (pseudoplasticity). This is attributed to structural rearrangements in the liquid and, in particular, to the orientation of anisometric, chain like, flow units [Tucker, 1997]. The authors provide the following explanation: "Viscosity is the only directly measurable kinetic parameter used in nucleation and growth equations. In the classical treatment of crystallization by Turnbull [1969] the nucleation rate, I, and crystal growth rate, U, are both inversely proportional to viscosity, η, with the viscosity term appearing in the preexponential factor shown below:

$$ I = \frac{k_n}{\eta} \exp\left[-\frac{b\alpha^3\beta}{T_r(\Delta T_r)^2}\right] $$

$$ U = \frac{k_n'}{\eta}\left[1 - \exp(-\beta\Delta T_r)\right] $$

where T_m is the melting temperature, T is the absolute temperature, and ΔT_r is the reduced undercooling $(T_m-T)/T_m$. The kinetic constants k_n and k'_n, nucleus shape factor,

b, and dimensionless parameters related to the liquid-crystal interface tension, α, and entropy of fusion, β, are described by Turnbull. The fraction of glass crystallized, X, with time at a given temperature was described by Uhlmann [1972] to be a function of the rate of nucleation, the third power of the growth rate, and the fourth power of time, shown below:

$$X = \frac{\pi \iota}{3} I U^3 t^4 \qquad \blacksquare$$

Under conditions of shear thinning, the effective viscosity decreases with increasing shear rate so that the viscosity can be expressed as a function of shear rate,

$$\eta = \eta(\varepsilon) \qquad \blacksquare$$

The crystallization parameters, such as the nucleation rate, are also functions of shear rate shown below:

$$I(\varepsilon) = \frac{k_n}{\eta(\varepsilon)} \exp\left[-\frac{b\alpha^3\beta}{T_r(\Delta T_r)^2}\right] \qquad \blacksquare$$

Low gravity processing is known to greatly reduce convection, which reduces shear in the liquid. Thus, the viscosity would be higher in these circumstances when compared to samples processed in unit gravity, reducing the nucleation and growth rates. For an increase in viscosity by a factor of two, the nucleation and growth rates are halved, but the fraction crystallized is reduced by a factor of 16. Since shear in liquid occurs as a result of fluid flow and fluid flow is greatly reduced in low-gravity, we have crystallization equations that are effected by gravitational effects. If the viscosity in low gravity environments is effectively higher, then crystallization can be suppressed in liquids that exhibit shear thinning." Overall, this journal publication provides useful information as it utilizes both a parabolic flight aircraft and a sounding rocket to achieve

microgravity but also provides a possible explanation for why crystal growth is suppressed in microgravity.

Additional research by Tucker et al. titled, "Effects of Microgravity on ZBLAN Optical Fibers Utilizing a Sounding Rocket," demonstrated how microgravity processing has the potential to reduce extrinsic losses in ZBLAN glass. Both intrinsic and extrinsic processes limit light propagation at low powers in ZBLAN [Tucker, 1996]. Intrinsic processes include band gap absorption, Rayleigh scatter and multiphonon absorption, which can be controlled be raw material processing. Extrinsic processes include impurities and crystallites formed during preform processing and fiber pulling. The intrinsic processes and extrinsic impurities can be better controlled through processing the initial raw materials and in preparation of the glass preform. Tucker et al. [1996] believe that devitification of ZBLAN is due to a narrow working range and low viscosity at the pulling temperature. Overall, as many researchers have shown, microgravity processing can offer the potential to minimize these losses in ZBLAN glass.

The objectives of this study were to heat ZBLAN fiber to the pulling and crystallization temperature in microgravity on board a sounding rocket and on the ground at 1g. Two meter lengths of ZBLAN optical fiber were obtained from two separate sources. The protective polymer coating was removed chemically, and then the fibers were cut into 25 mm lengths. The fiber diameters were 300 microns for the fiber provided by Infrared Fiber Systems (IFS) and 530 microns for the Galileo fiber. A fiber processing furnace was designed and constructed as a payload on the Congquest 1 sounding rocket flight launch on April 3, 1996 at White Sands Missile Range, New Mexico. The entire system was designed to fit within the size constraints of the supplied

payload cylinder skin of 33 inches long and 15.3 inches inside diameter. Once the tests

were completed, optical and scanning electron microscopy were used to evaluate each

fiber. Energy dispersive x-ray analysis was also performed in conjunction with the SEM

analysis.

Acceleration levels on board the rocket were in the 10^{-5} to 10^{-6} level through the

majority of the μg portion of the flight. After recovery of the sounding rocket it was

found that nine of the twelve ampoules had cracked. The three samples that did survive

the impact had been heated to the pulling temperature of 323°C for the two Galileo fibers

and 340°C for the one IFS fiber. These specimens did not show evidence of

crystallization. However, voids were present along the side of the fiber, which was in

contact with the ampoule wall in all three samples. Samples heated to the same

temperature on the ground showed significant evidence of crystallization. It is believed

that the porosity noticed is due to the reaction of the ZBLAN fluorides with the SiO_2 of

the ampoule. The author's main conclusion from these experiments is that under 1g there

is enough convection occurring to enhance crystallization. During microgravity the

convection would be suppressed and thereby preclude crystallization. Tucker et al.

reproduced previous results obtained in past studies and coincides with results obtained

by Varma et al. Similar to Varma et al. this research only focused on the heat treatment

process of ZBLAN fiber drawing in microgravity as opposed to the complete drawing

process in microgravity. In addition, both authors use SEM micrographs to interpret their

results as will be conducted in this research.

Further research conducted by Tucker et al. titled, "The Study of Devitrification

Processes in Heavy-Metal Fluoride Glasses" attempted to explain the suppression of

crystallization of ZBLAN glass under microgravity. The role of viscosity is critical when investigating nucleation mechanisms, but unfortunately due to the tendency of fluoride glasses to devitrify, the viscosity data for ZBLAN glass is incomplete. Other studies have been done on ZBLAN and fluoride glass but the only reliable data produced has been at temperatures below the glass transition and above the melting point. The viscosity of ZBLAN decreases rapidly with increasing temperature as with most glasses [Tucker, 1996]. This transition is even more pronounced in fluoride glasses and occurs at a far lower temperature. The consequence of this fast viscosity change is that the optimum fiber-drawing range is narrow and the risk of entering the crystallization region is heightened. It has been demonstrated that remelting ZBLAN glasses in a microgravity environment can suppress devitrification [Varma, 2001; Tucker, 1996; Dunkley, 2004].

The devitrification mechanisms of ZBLAN at 1-g are poorly understood. It was initially hypothesized that the gravity-induced density segregation would cause a composition gradient to occur within the glass with the heavier fluorides (BaF_2 and LaF_2) sinking to the bottom, thus shifting the glass into a composition region that favors crystallization over the vitreous state. Researchers have offered an explanation based on the concept of shear thinning to account for the 1-g crystallization of ZBLAN glass. HMFGs are considered non-Newtonian fluids and consequently exhibit pseudoplastic flow behavior, whereas their viscosity decreases with increasing shear rate. Tucker et al. proposed that the 1-g convective flow within the glass preform is sufficient to cause sheering of the glass, thus lowering its intrinsic viscosity. The lowered viscosity causes an increase in the rate of diffusion within the glass, allowing crystallites to more readily nucleate and grow. Previously described, this suggests that a decrease in the viscosity by

33

a factor of two, which would double both nucleation and crystallization rates and consequently increase the fraction crystallized by a factor of 16. However, the extent to which convection can produce a substantial shear on the glass in this temperature regime has yet to be established, according to the article.

2.4 Related Work on ZBLAN

Additional work related to ZBLAN and the devitrification mechanisms under microgravity are presented in this section. Another aspect of devitrification of HMFG that is being researched is the influence of hydrostatic pressure by Dunkley et al. [2004]. It has been shown that nucleation and crystal growth can be lowered by pressurizing a vitreous melt. However, exerting this hydrostatic pressure also causes an increase in the viscosity of the melt yielding the opposite effect. It has been discovered that in cordierite glass that pressure suppresses nucleation and crystal growth under both low pressure (0-2kbar) and high pressure (greater than 5kbar) conditions. Quartz from vitreous silica is an example of increased crystal growth rates with the application of hydrostatic pressure in the range of 5-40kbar. Researchers suggest that the application of hydrostatic pressure decreases the atomic transport coefficients (i.e., fluidity, diffusivity, and crystal growth rate) in ionic solids resulting in the suppression of devitrification with pressure in these materials. In contrast to the above statement, covalent glasses such as fused silica undergo the opposite effect because an increase in hydrostatic pressure enhances the transport properties. Due to fluoride glass being more ionic in nature it would most likely behave more similarly to cordierite under pressure. Therefore, with the application of hydrostatic pressure nucleation will be suppressed in ZBLAN glass. However, this

explanation of nucleation suppression in more ionic glasses has been established entirely on observations made on silica-based and/or oxygen containing glasses [Dunkley, 2004].

Overall, there are many different techniques that can be used to measure the viscosity of a glass. Many materials, including glasses, exhibit a substantial change in viscosity with temperature. Such high changes in viscosity are often recorded such that it is usually necessary to employ several different techniques and viscometers to measure the full viscosity range of the material. Dunkley *et al.* (2004) developed a piezoelectric viscometer to complete the viscosity data for ZBLAN glass without need for a second piece of equipment. It also provides for a compact size and low energy measurement system; characteristics that are critical for reduced gravity experiments. The piezoelectric viscometer functions by giving off an ultrasonic pulse that travels through the fluoride glass rod until it is reflected back to the transducer by the glass-rod and/air interface. An ultrasonic detector attached to the piezoelectric transducer then calculates the time of flight of the ultrasonic pulse. The time of flight and the viscosity of the glass can be determined from the changes in the time of flight of the ultrasonic pulse at various test temperatures. The main purpose for this research is to fully describe and present techniques to suppress crystallization processes in ZBLAN fibers. Dunkley *et al.* (2004) feel that the role of viscosity in devitrification is significant and a reliable model to describe crystallization cannot be advanced until the full viscosity spectrum of ZBLAN glass is determined. From this research a piezoelectric viscometer was developed to measure the missing viscosity data through terrestrial and reduced gravity experiments. However, no data or validation was presented on the use of the piezoelectric viscometer. This research also didn't present any information regarding specific experiments on

ZBLAN in microgravity but described a possible explanation for the crystal suppression in microgravity. Dunkley et al. did present the idea that hydrostatic pressure on terrestrial devitrication of ZBLAN fibers could be a mechanism suppressing crystal growth. The article relates ZBLAN to cordierite glass, which was noticed to have crystal suppression under hydrostatic pressure [Dunkley, 2004]. Cordierite glass is similar to ZBLAN as it is an ionic glass. However, hydrostatic testing on ZBLAN has not been attempted. The work done by Dunkley et al. provides useful information pertaining to this study as it contributes to the previous postulations of 'shear thinning' being a possible explanation to crystal suppression under microgravity.

An article by Tucker et al. [2007] describes the effects of a magnetic field on the crystallization of a fluoriozierconate glass. Other researchers have used magnetic fields to affect flows in conducting fluids and results show that crystals are improved by using uniform and rotating magnetic fields. Convective heat and mass transport in semiconductor melts with large electrical conductivities can be controlled by magnetic fields [Tucker, 2007]. The overall purpose of the work was to determine whether crystallization in ZBLAN glass would be suppressed in a magnetic field. Nine fibers were used in this research. The fibers were 50 mm in length and 300 μm in diameter. Three samples were heated to the crystallization temperature of 345°C for 45 sec with the magnetic field vector parallel to the gravity vector, and the other three samples were heated to the same temperature with the magnetic field vector perpendicular to the gravity vector. The last three samples were used as control specimens. After processing the fibers in microgravity, the samples were observed with a stereo-optical microscope and a scanning electron microscope (SEM). X-ray diffraction was also used to identify

the crystal type. The ZBLAN fibers that were heated in the magnetic field did not show evidence of crystallization using both the optical microscope and the SEM. It was hypothesized by the authors that the mechanism for the suppression of crystallization was the permeability difference between the amorphous glass and the crystallites. Assuming the formation of spherical nuclei in solids, the change in free energy without a magnetic field consists of three parts: the bulk free energy, strain energy, and surface energy. It was seen that the effect of a magnetic field yields two measurable variables: the intensity of the applied magnetic field, and the permeability difference. The authors tested this hypothesis that permeability may play a role in suppressing crystallization. A glass sample with a thickness of 4 mm and a diameter of 11 mm was crystallized fully by heating to 345°C for 6 hours. The magnetic susceptibility of the samples were measured using a vibrating sample magnetometer. The result of the test show that there is no significant numerical difference between the calculated permeability values, which eliminates a difference in permeability between the glass and the crystal as being the mechanism of suppressed crystal growth. It has been reported by other authors that in semiconductor melts the flow velocity is attenuated and viscosity increases above a critical magnetic field strength. The authors believe that a similar mechanism may be at work for this research. An increase in the viscosity would slow diffusion, and crystallization would be slowed. The authors from this article demonstrated the effects of a magnetic field on the crystallization of ZBLAN fibers. This result is useful to this research as it contributes other mechanisms that may be at play in the crystal suppression of these fibers. Likewise, the authors used X-ray diffraction and SEM to study the

crystalline structure of the fibers. This is pertinent to this research, as equivalent imaging will be used to characterize the microstructure of the ZBLAN fibers.

In the article, "Mathematical Modeling and Experimental Investigation of the Effect of Temperature Gradients on Crystallization Processes under Terrestrial and Space Conditions" by V.I. Strelov et al. [2005] suggest that the processes of heat and mass transfer occurring in a melt during its crystallization is one of the deciding factors for the homogeneity of properties of the crystal growth. Depending on the structure and intensity of these processes, the crystal growth is determined by diffusive, convective, or both of these HMT processes [Strelov, 2005]. The authors feel that the main decisive factor for this occurrence is the radial temperature gradient ΔT_r in a melt and under the conditions of microgravity the Marangoni convection is the deciding factor. The Marangoni Effect is described as the mass transfer along an interface between two fluids due to surface tension gradient. The authors feel that by optimizing these processes it will be possible to grow single crystals with highly uniform properties under both terrestrial and space conditions. The purpose of their study is to investigate the processes of formation of microinhomegeneities during the growth of Ge(Ga) crystals by directed crystallization under terrestrial and space conditions, depending on the intensities of thermal gravitational convection and Marangoni convection. The authors used a mathematical approach to determine the velocity of convective flows in the melt volume and near the phase boundary for the growth of Ge(Ga) single crystals by crystallization as functions of the radial temperature gradient at the melt surface and the axial temperature gradient under terrestrial and space conditions. This was shown theoretically and then was confirmed experimentally that the Marangoni convection significantly affects the

HMT processes under both terrestrial and space conditions. It was shown that under 0-g

conditions the Marangoni convection is the main factor violating the diffusive HMT

mode, which leads to uninhibited processes in the melt during the crystal growth. This

proof shows that convection can be reduced in microgravity, therefore crystallization will

ultimately be suppressed. A schematic of their convective flow velocity model results are

shown in the figure below.
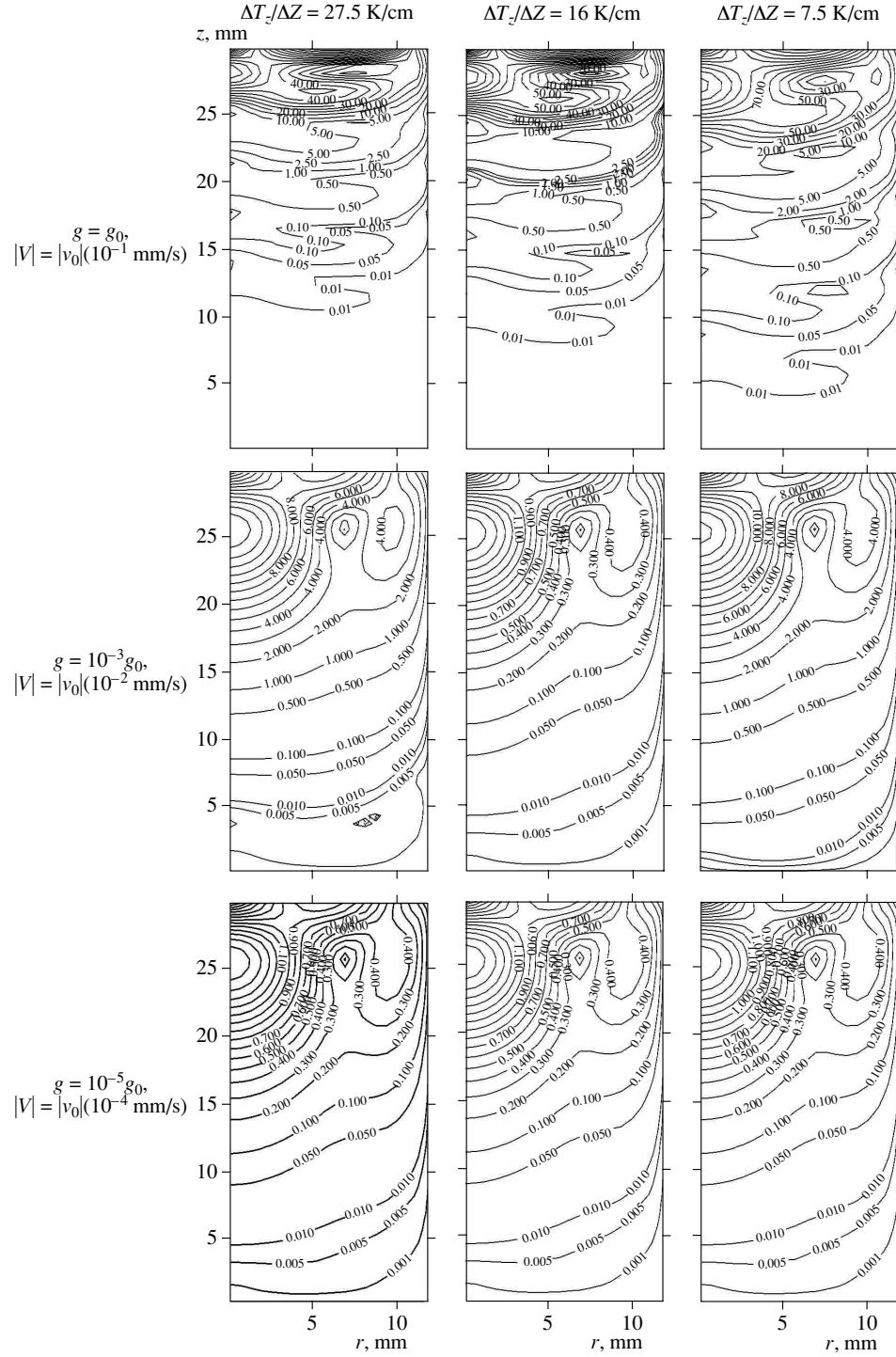
Figure 2.1: *Isolines of the absolute velocity of convective flows at different values of gravity and ratios $\Delta T_z/\Delta Z$ ($\Delta T_r = 2K/cm$) [Strelov, 2005].*

This analysis is beneficial to the present effort as it focuses on convection and surface tension as the main contributors to crystal growth/suppression. Although the authors emphasis is on the direct crystallization of Ge(Ga) single crystals this work is still applicable to crystal formation in ZBLAN glass in microgravity as the convective forces are still inherent in the vitreous material. The mathematical model is extremely useful, as similar convective flow fields will be developed for this study.

The article, "Under What Conditions can a Glass be Formed," by Turnbull et al. [1969] provides quality background information describing viscosity of glass and how it is related to temperature, as shown in the below equation:

$$\eta = A exp[\frac{a}{T-T_0}] \qquad \blacksquare$$

where A, a and T_0 are constants depending on the material and T is the absolute temperature and T_0 is the initial temperature. Therefore the viscosity will increase with a decreasing temperature either when a is very large relative to T or, if a is small, when T has fallen nearly to T_0. The article also describes nucleation and how crystallization cannot occur without nucleation. The author presents the statement, "The resistance of a liquid to nucleation, as measured by the undercooling necessary to overcome it, is much greater than its resistance to growth." Heterogeneous nucleation will typically occur in a melt because there are either suspended particles or container walls to create nucleation sites. The pertinent information from this article is the topic of bypassing crystallization. This topic begins by introducing an equation that describes the number of crystal nuclei, δn, which appear isothermally in a volume, v_1, of liquid in time δt as:

$$\delta n = I v_1 \delta t \qquad \blacksquare$$

where I is the nucleation frequency/(volume x time). The crystal growth rate is so large in a liquid with a low viscosity that the cooling rate will be limited by the recalescence (heating of the liquid upon crystallization) after a single nucleus has appeared. Under these conditions nucleation would have to be suppressed completely for crystallization to be bypassed. In the equation below, n would have to be less than 1 if crystallization was suppressed. Equation 2.9 is shown below:

$$n = v_1 \int_0^t I\,dt$$

where t is the time in which the liquid is cooled, I is a function of temperature, and the variation of v_1 with temperature is neglected. These two relationships indicate that the probability of forming a nucleus will be less the smaller the volume of the liquid and the nucleation frequency and the greater is the cooling rate. The article describes an example of a liquid free of heterogeneities when it is undercooled from its crystallization temperature, T_m. Formation of the first nucleus will require at least the time, t_{min}, for all molecules constituting the nucleus to jump from the liquid to the nucleus, i.e. $t_{min} = i^* \tau_i$, where i^* is the critical number of molecules and τ_i is the initial time. At a viscosity of 10^{-2} poise, τ_i is about 10^{-12} s and, setting i^* to 100 would yield $t_{min} = 10^{-10}$ s. Thus this liquid would not crystallize if it were cooled to its glass temperature in less than 10^{-10} s. This would require a cooling rate of the order of 10^{12} K/s, which has not been achieved experimentally.

This article is useful as it provides a lot of information involving crystal nucleation of vitreous materials and the governing equations describing viscosity and the crystallization bypass equation. It also delivers equations governing nucleation, which

42

can be used in further research. Although this article is generalized for any vitreous material it can be specifically applied to ZBLAN glass fibers.

Relative to the postulated crystal suppression mechanism of shear thinning is the viscosity of the pseudoplastic material. In the article, "Measurement of Extensional Viscosity by Stretching Large Liquid Bridges in Microgravity" by S. Berg et al. [1994] experimental viscosity measurements in microgravity were completed. This article presents and tests a new liquid bridge stretching technique for measuring the extensional viscosity of polymer solutions. This method utilizes two adjustable plate devises held by surface tension that were mounted to a stepping motor that can deliver a constant extension rate. The apparatus was operated under microgravity in the Bremen drop tower for a free fall of 4.7 s. All experiments were carried out at a constant temperature of 25°C. A Newtonian fluid and a non-Newtonian (viscoelastic) fluid were tested at varying weight concentrations. The effect of necking was avoided by using variable plate diameters. The purpose of this article was to develop and test the apparatus under microgravity. The article, however, doesn't describe why it was necessary to run the apparatus under microgravity. We believe that this was done because the microbalance system can only measure forces up to 1 N with an accuracy of 0.001N, thus the weight of the plates and fixtures below would affect the output reading. Therefore, dropping the entire apparatus in a drop tower will eliminate this strain on the balance system. The authors feel that the objectives of this research were achieved. The apparatus was designed for measuring extensional viscosity and tested in microgravity. This article is useful in the sense that if a ZBLAN viscosity measuring apparatus is required then the information from this article can be useful. Viscosity measurements could be useful to

this research as with a pseudoplastic the viscosity decreases with an increase of shear rate and at low viscosities crystallization is more prevalent.

2.5 Crystal Growth Processes

In order to fully understand why crystal growth is suppressed in a microgravity environment we must understand the fundamental forces that cause the initial nucleation and subsequent growth of crystals. A system nucleates when a new phase forms in the parent phase. Nucleation can occur in two different forms: heterogeneous and homogeneous nucleation. The process of heterogeneous nucleation is when a new phase nucleates at a boundary (such as container wall or an existing grain boundary) or on foreign objects such as impurities trapped in the parent phase. Contrary, homogeneous nucleation occurs randomly within the parent phase. Since this involves the creation of new surfaces, homogeneous nucleation requires more energy than the heterogeneous nucleation. Since control of impurities is not a subject of this research and the solidification of a glass fiber typically occurs when it is being drawn (outside of a container), only homogeneous nucleation is being considered. Schaffer et al. [1999] provides the following explanation: "The interatomic distances in the liquid are similar to those of the crystalline phase, but each atom on average has fewer nearest neighbors in the liquid than in the crystal. Therefore the structure is more open and allows greater atomic mobility than does that of the solid state. Distributed throughout the liquid are small, closely packed atomic clusters having a packing arrangement similar to that of the solid. Due to the open structure, these clusters form and disperse quickly. The relationship between the size and the stability of the clusters depends on the temperature." Overall, two specific components are associated with the free-energy

change of the liquid-solid transformation. The first is the change in energy associated with the creation of the liquid-solid interface of the new crystal, and the second is the difference in bulk free energies of the liquid and solid phases (equivalent to latent heat of phase transition). The formulation is shown below:

$$\Delta G(r) = (4\pi r^2)\gamma_{SL} + \frac{4}{3}\pi r^3 (\Delta G_v)$$ ▮

The above equation describes the change in free energy $\Delta G(r)$ as a function of r (radius of a newly formed spherical particle). Where γ_{SL} is the interfacial energy per unit area and ΔG_v is the change in free energy per unit volume of the nucleated crystal. The first term in the equation is the change in energy associated with the creation of the liquid-solid interface, and the second is the difference in bulk free energies of the liquid and solid phases.

The critical radius above which a crystal is stable is given by:

$$r^* = \frac{(-2\gamma_{SL})T_E}{\Delta H \Delta T}$$ ▮

Where T_E is the Equilibrium temperature, ΔT is the degree of undercooling and ΔH is the change in enthalpy (equivalent to latent heat).

Once a critical radius is reached the r^3 volume term in Eq. 2.10 begins to dominate, and further increases in the particle size resulting in a reduction in the free energy of the system. Therefore the critical radius represents the size of a stable nuclease below which the smaller particles redissolve into the liquid phase and above which the particle will continue to grow. Eqn. 2.2 shows that as the undercooling ΔT increases, the energy barrier to nucleation decreases and a nucleus of smaller size can become stable, therefore lowering the temperature of the system can allow the nucleation to occur more

readily. However, with the decreased temperature there is a reduction in atomic

'mobility'. Diffusion (random fluctuations in the local arrangements of atoms) is slowed

within the system, which reduces the rate at which atoms can move and cause clusters of

atoms to form. The effect of temperature on the energy balance and mobility (diffusion)

can be seen graphically in the Figure below.
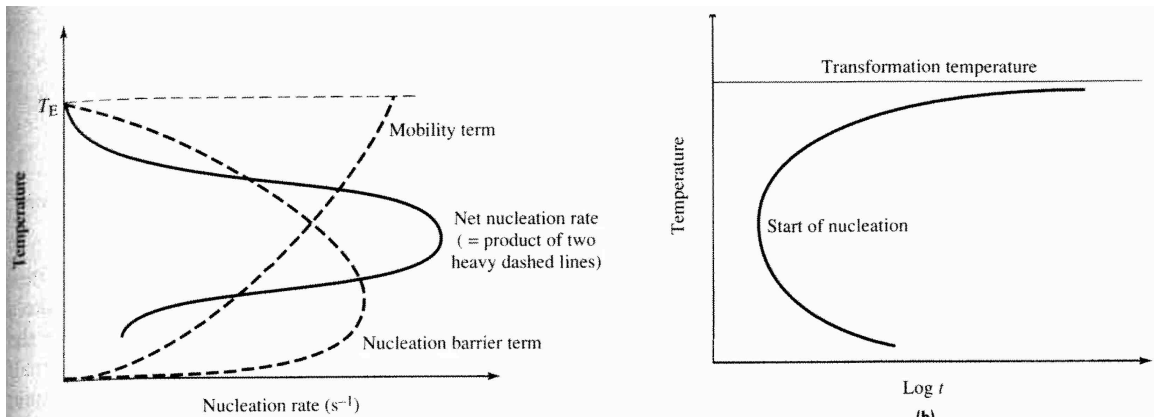
Figure 2.2: *The influence of temperature on the mobility (diffusion) and the nucleation*

barrier (left); How time and temperature affect the nucleation process (right) [Schaffer,

1999].

Vlack [1989] presents a relationship for crystal formation that combines the nucleation

rate $\dot{N}$ and growth rate $\dot{G}$ of crystals given by R:

$$R = f(\dot{G}\dot{N})$$

This can also be shown schematically in Figure 2.3 below.

46
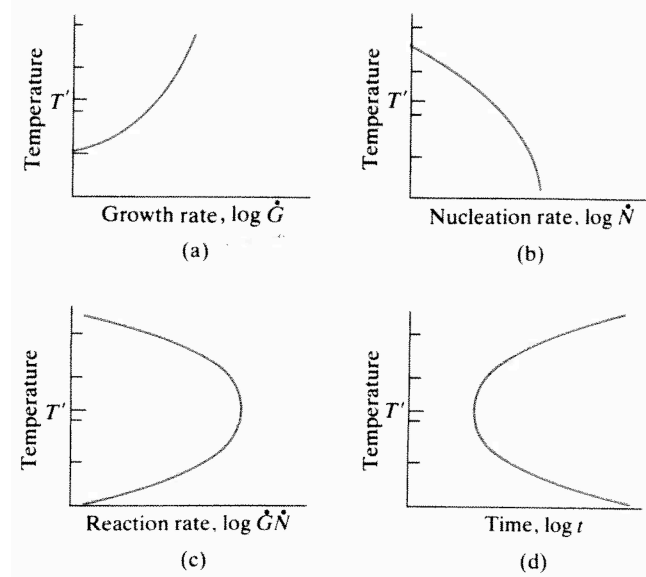
Figure 2.3: (a) Crystal growth vs. temperature (b) Nucleation rate vs. temperature (c)

Reaction rate vs. temperature (d) Reaction time vs. temperature [Vlack, 1989].

From the above discussion we can see that crystal growth is aided by the mobility of

molecules at higher temperatures and nucleation proceeds more rapidly with greater

supercooling. Shown in Figure 2.3c is the intermediate temperature, T', which is the most

conducive to crystal growth. Overall, if the temperature is low there is more nucleation

but less growth because diffusion is hindered. Alternatively, at higher temperatures

nucleation is slowed but growth is increased because diffusion is more active. Existing

literature on crystal growth clearly emphasize the relevance of movement of molecules

on the resulting microstructure of materials.

Since the growth of a crystal is dependent on the availability of new molecules

and hence driven by mobility of molecules, it is influenced by several mechanisms of

fluid flow. One example is the replenishment of molecules is aided by a higher diffusion

rate. Diffusion is driven by random movement of molecules, and increases with

temperature. In addition, the rate of collision of molecules is also a function of the size

47

and asperity (higher chances of collision for more elongated molecules) [Hiemenz and Rajagopalan, 1997].

The fluid immediately next to a newly formed crystal tends to have a lower concentration of molecules that have the needed attributes for crystallization. Mixing and flow within the liquid therefore assists crystallization. The ratio of probability of collision of molecules due to fluid flow vs. that due to pure diffusion controlled mobility was provide by Probstein [1994] as follows:

$$\eta(R_1 + R_2)^3 \, (\delta v/\delta x)/(2k_B T) \qquad \blacksquare$$

Where v is viscosity, $\delta v/\delta x$ is velocity gradient, T is absolute temperature, k_B is Boltzmann's constant, and R_1 and R_2 are the size of the particles colliding. While this equation was developed for colloidal chemistry to model flocculation and sedimentation, it quantifies how convection currents can significantly increase crystal growth.
In the absence of convection in a micro-gravity environment, surface tension forces tend to provide residual fluid flow and hence govern the location and growth rate of crystals. Surface tension is a function of temperature. Hence temperature gradient in a cooling fiber strand will lead to differences in surface tension along the length of the fiber. Since the surface has a curvature, this leads to a pressure gradient *p(x)* along the fiber equal to:

$$p(x) = T(x)/R \qquad \blacksquare$$

where *T(x)* is the surface tension gradient along the fiber and *R* is the fiber's radius. Surface tension driven flow is also referred to as Marangoni convection.

2.6 Assessment of Thermal Degradation and Fracture of ZBLAN Fibers

To the authors knowledge there are no specific publications relating the effect of crystallization on the microstructure of ZBLAN fibers. However, there are selected publications that relate microstructure with mechanical properties of other materials. While the specificity of the topic related to optical waveguides is very limited, many Material Science textbooks provide a short summary on the effect. Meyers and Chawla [2009] provide the following explanation, "Mechanical properties of ceramics are affected by grain size in several ways. The most important effect is the reduction in the sizes of inherent flaws, as the grain size is reduced." Therefore, vitreous materials with scattered micro-crystals are considered inherent flaws in the material and could greatly reduce the mechanical properties of the material. The location of these micro-crystals could also attenuate the light transmission resulting in a higher loss.

Park and Yang's [2001] work titled, "Effect of the Microstructure on the Mechanical Properties of a Directionally Solidified $Y_3Al_5O_{12}/Al_2O_3$ Eutectic Fiber" studied the strength and fracture behaviors of directionally solidified $Y_3Al_5O_{12}/Al_2O_3$ eutectic fibers related to the microstructure. The microstructure was depicted using X-ray diffraction, SEM, and energy dispersive spectroscopy (EDS). The imaging techniques employed by this article provide useful insight to the current study as it demonstrated three imaging capabilities. Room temperature and 1460°C heat treatment tensile testing was performed using an Instron universal testing machine. The fracture toughness and crack growth behavior was determined using a Vickers hardness tester. The $Y_3Al_5O_{12}/Al_2O_3$ fibers have a nominal diameter of 75μm. The heat treatment process was performed on the fiber to inhibit dissimilar microstructures of the fiber. Coarsening of the

49

fine lamellar structure occurred after exposure at elevated temperatures. Mechanical testing revealed a degradation of tensile strength in the fiber after heat treatment. SEM showed that the heat treatment accounted for the development of surface grooves at the surface of the fiber. The indentation test displayed a radial crack type and exhibited an anisotropic crack propagation behavior. However, the coarsening of lamellar microstructure did not affect the fracture toughness values. This was believed to be due to the aligned lamellar microstructure that was maintained after the heat treatment. The described work is useful to the mechanical testing section of this research as it implements a heat treatment process to affect the microstructure of a eutectic fiber and relates the microstructure to the mechanical properties. Although the paper is not specific to ZBLAN fiber it still contributes to the current research. The authors also use multiple advanced imaging techniques. The tensile and hardness physical mechanical testing is similar to what will be conducted in this current study.

A publication by Hayashi et al. [1989] titled, "Optical Fiber Cable Flexibility Design under Plastic Deformation and its Evaluation" provides information related to the flexibility of a fiber when it is bent to the range of plastic deformation. This research does not relate the microstructure to the mechanical properties of the material, but instead, evaluates the flexibility of a fiber. This article is discussed in this section as the handling ability of the ZBLAN fiber will be examined and compared to the size/location/amount of microcrystals inherent to the fiber. The specific objective of the work by Hayashi et al. goes beyond the scope of this research but the main pertinence is the description of the bending strain related to the curvature of the fiber. This relationship can be seen in the equation below.

$$\varepsilon = y\rho$$

Where ε is the strain at the location y measured from the neutral axis (center of fiber) and

ρ is the known curvature of the fiber. A schematic of this relationship can be viewed

below.
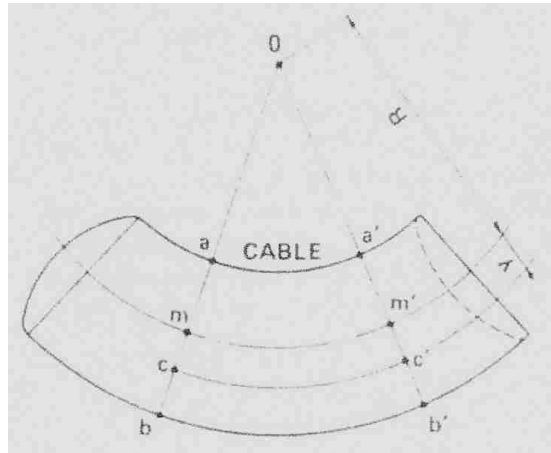
Figure 2.4: *Schematic showing the curvature of the bent fiber [Hayashi, 1989].*

The above equation will be utilized with SEM to determine the handling ability of the

fiber related to the microstructure of the ZBLAN fibers.

2.7 Conclusions

All of these articles provide useful insight into the understanding of ZBLAN glass

and how gravity affects the fabrication and inherent properties of the material.

Researchers who conducted processing of ZBLAN glass in microgravity all saw the same

results; devitrification was suppressed under a reduced gravity environment and was

increased in a high-g environment. With regards to microgravity processing many

authors postulate ideas on why gravity has such a strong influence on ZBLAN glass. The

main hypothesis for this study is that particle motion or mobility within the semi-molten

fluid is the main mechanism governing crystal growth in a vitreous material. The main contributor to this hypothesis is buoyant driven convection, which directly relates to gravity. Other particle motion mechanisms such as diffusion and Marangoni convection are affected by temperature, not gravity. This hypothesis comes from the idea of the depletion zone described by Kundrot [2001]. The depletion zone is the area around a nucleated crystal that has been depleted, 'starved', of growth units. Without a higher order particle motion mechanism, such as buoyant driven convection, there will be no movement within the liquid to fuel the growth. Therefore, reducing gravity will proportionally reduce buoyant driven convection, which will create depletion zones around nucleated crystals. Many authors feel that ZBLAN exhibits a pseudoplastic behavior in which 'sheer thinning' promotes crystallization. The flow of logic for this hypothesis suggests that convection can be significantly reduced in microgravity. Therefore, lack of fluid flow in microgravity yields low shear stress within the fluid. Low shear stress would result in a high viscosity of the fluid, which, in turn, suppresses crystal formation or even nucleation. This idea, among others, will be examined in this research.

CHAPTER 3 – Experimental Program

This section provides a summary of the experiments that were conducted in the course of the present research.

3.1 Microgravity Testing

The primary experimentation completed in this research was completed on a parabolic aircraft. The parabolic aircraft flies along a parabolic trajectory that reduces the gravitation to zero. The aircraft provides a microgravity period of approximately 20 seconds and a hyper-gravity duration of approximately 56 seconds. The Zero-G Corporation provides a pristine microgravity (0.0-g ± 0.05-g) environment for a 20 second duration, whereas, the hyper-gravity intensity ranges from 1.2-g – 1.8-g. The flight regimen consisted of 4 sets of 10 parabolas per flight.

3.2 Description of Quencher and Operation

The Quencher is the testing apparatus used on board the Zero-G Corporation's parabolic aircraft. The name "Quencher" came from the act of physically quenching the sample after it has been heated. The Quencher was initially developed for experiments completed by Dr. Dennis Tucker [Tucker, 1997]. A photo of the Quencher can be seen in Figure 3.1.
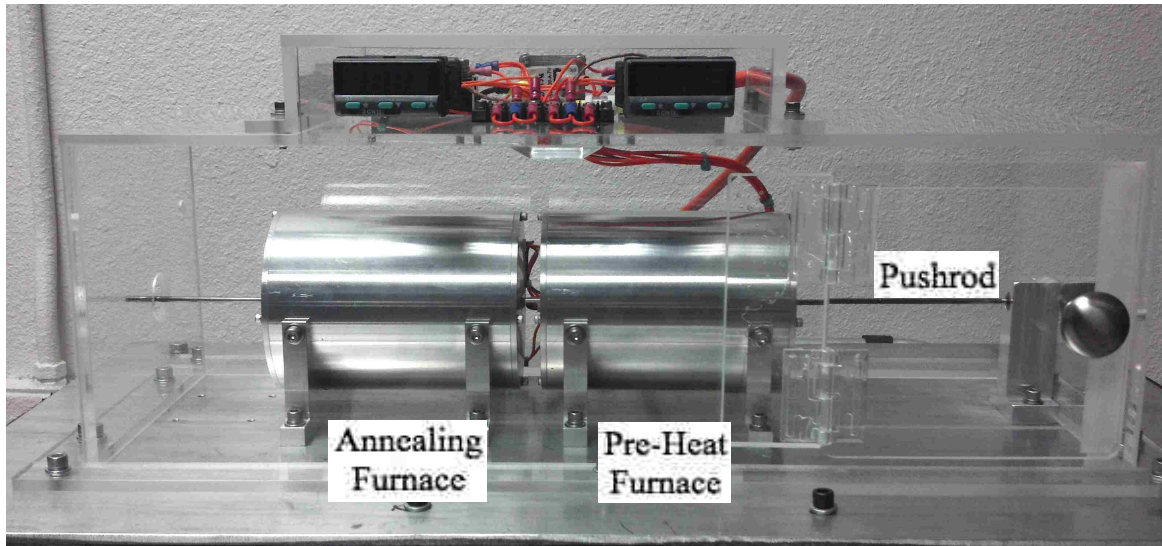
Figure 3.1: *A photograph of the Quencher.*

The Quencher consists of two cylindrical furnaces (a pre-heat and an annealing furnace) with a 4mm (.157in) hole through the middle of each. This allows a stainless steel pushrod to easily pass through each furnace. The two furnaces are encased in a Plexiglass box that holds the electronic controllers and also prevents any debris from entering the furnace area. During operation, a single quartz ampoule of average length 3.2 cm (1.26 in.) and 3 mm (0.118 in.) in diameter, containing two ZBLAN samples, were placed in the end of the pushrod. Each ampoule contained two 2-3 mm (0.79 in - 0.11 in.) by 1.03 mm (0.041 in.) diameter samples of the same type. These samples were separated by a small piece of silica glass, of similar length but slightly larger diameter, 1.09 mm (0.043 in.). This was done to ensure the two ZBLAN samples don't come in contact with each other. Eliminating sample to sample contact will prevent unwanted crystal nucleation [Tucker, 2001]. Therefore, the samples are only allowed to come into contact with the glass that is holding it and separating it. The silica glass has a very stable molecular

structure and a glass transition temperature (Tg) of 1175°C [Harrington, 2007]. Hence it does not physically or chemically interact with the ZBLAN during the experiment [Tucker, 2001]. No alteration to the silica glass was observed during experimentation; the two sides of the ZBLAN samples did not demonstrate any observable differences, irrespective of their proximity to the Silica glass. The ampoules were sealed under vacuum to remove any effect from moisture. The ampoule and sample configuration can be seen in Figure 3.2.
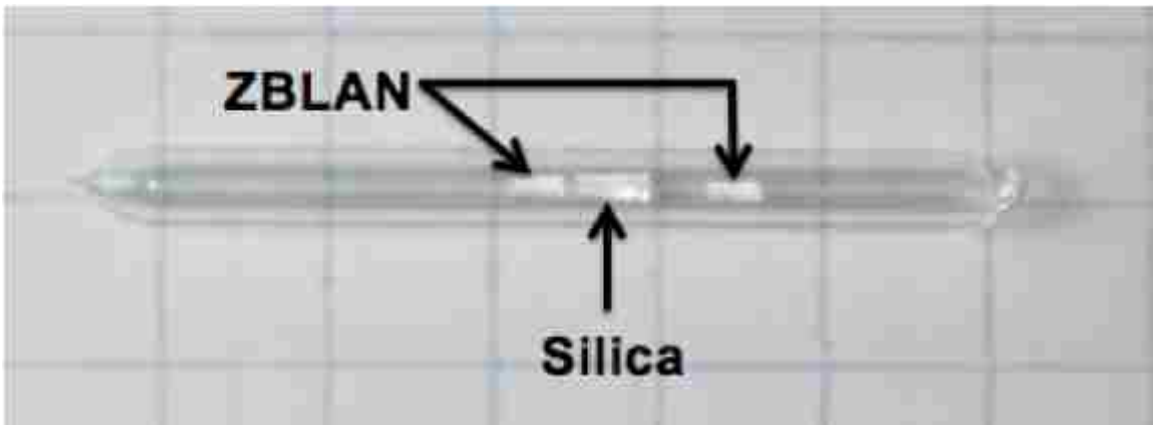
Figure 3.2: *Schematic of the ampoule configuration containing the ZBLAN samples.*

3.3 Characterization Process

Prior to any testing the Quencher was initially characterized. The purpose of this was to gain a better understanding of how the Quencher operates, how to manually operate the Quencher, the temperature ramp up/cool down time, and any other critical information required to obtain accurate results. The characterization process was done with furnace controller output and two different thermocouples. Two different type-K thermocouples were used for characterizing the two furnaces. One thermocouple had a larger diameter of 0.787 mm (0.031 in.) and the smaller gage thermocouple had a

diameter of 0.33 mm (0.013 in.). In future references in this document, the thermocouples will be designated "large" for the larger diameter thermocouple, and "small" for the smaller diameter thermocouple. In addition to the physical size of the thermocouples, the protective sheathing was also different. The large thermocouple had a higher temperature protective sheathing. Therefore, certain higher temperature redundant characterization wasn't possible due to the lower temperature protective sheathing of the smaller thermocouple. The following sections will be separated into characterizing each furnace (pre-heat furnace and the annealing furnace).

3.4 Pre-Heat Furnace

The purpose of this furnace is to increase the temperature of the sample so that the sample reaches the annealing temperature quicker. Due to the 0-g/1-8g transitions there is limited time to raise the sample temperature to the annealing temperature. Therefore, the Pre-Heat furnace was required to reach the annealing temperature in an appropriate timeframe. For example, one temperature test point is 350°C (annealing furnace) where the Pre-Heat furnace will be set at 250°C. The Pre-Heat furnace reduces the temperature differential to 100°C, in this example, as opposed to a ≈320°C difference from room temperature (≈22°C). The main purpose of the characterization process is to compare the controller read out temperature to that of one of the thermocouples. Thus, the operators know a more precise temperature range inside the furnace. For all characterization tests, the thermocouples were placed directly in the center of the furnace, unless otherwise stated. Figure 3.3 shows the temperature ramp from near room temperature to a final temperature of 260°C. This test will ultimately show how fast it will take the furnace to stabilize at its set point, as well as how far the actual temperature over-shoots.
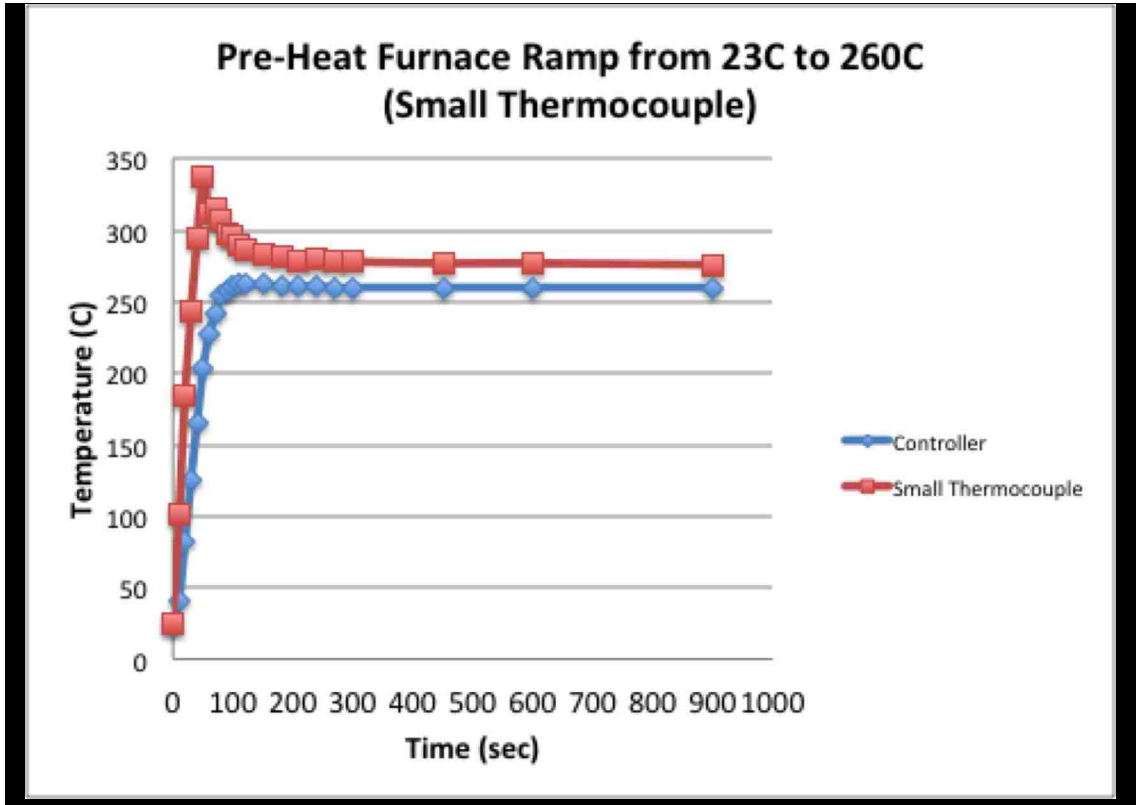
Figure 3.3: Pre-heat furnace ramp time from 23°C to 260°C, with the small

thermocouple.

From Figure 3.3, it can be seen that within one minute the thermocouple jumps about 100

degrees over the set point on the controller. However, the temperature drops back to the

set point within four minutes. The controller also goes above the temperature set point

but only by approximately10 degrees, and stabilizes within two minutes. Also

represented on the graph is that after both the controller and thermocouple have

stabilized, the thermocouple still reads at a higher temperature. The exact readings are

260°C on the controller and 276°C on the thermocouple.

The next graph shows the time required to increase the temperature by ten

degrees.
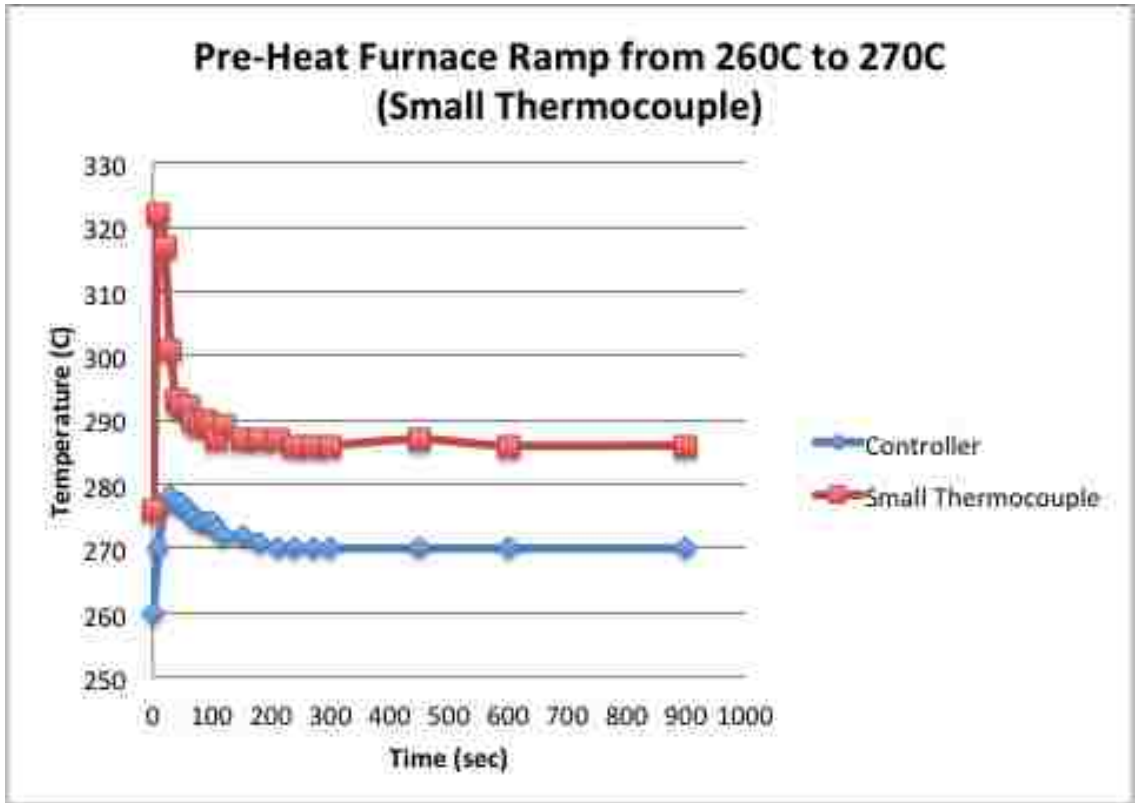
Figure 3.4: *Pre-heat furnace ramp from 260°C to 270°C, with the small thermocouple.*

Figure 3.4 shows an immediate jump for both the controller and the thermocouple. The

thermocouple maxes out at 322°C within ten seconds, and the controller at 278°C within

30 seconds. Both the thermocouple and controller stabilize within three minutes. As in

the previous graph, the thermocouple stabilizes at a higher temperature (286°C) than the

controller (270°C).

The following graph depicts the time required to cool the furnace down from

270°C. This information provides insight into reducing the temperature in the case of

retesting previous test set ups while on board the parabolic flight aircraft.
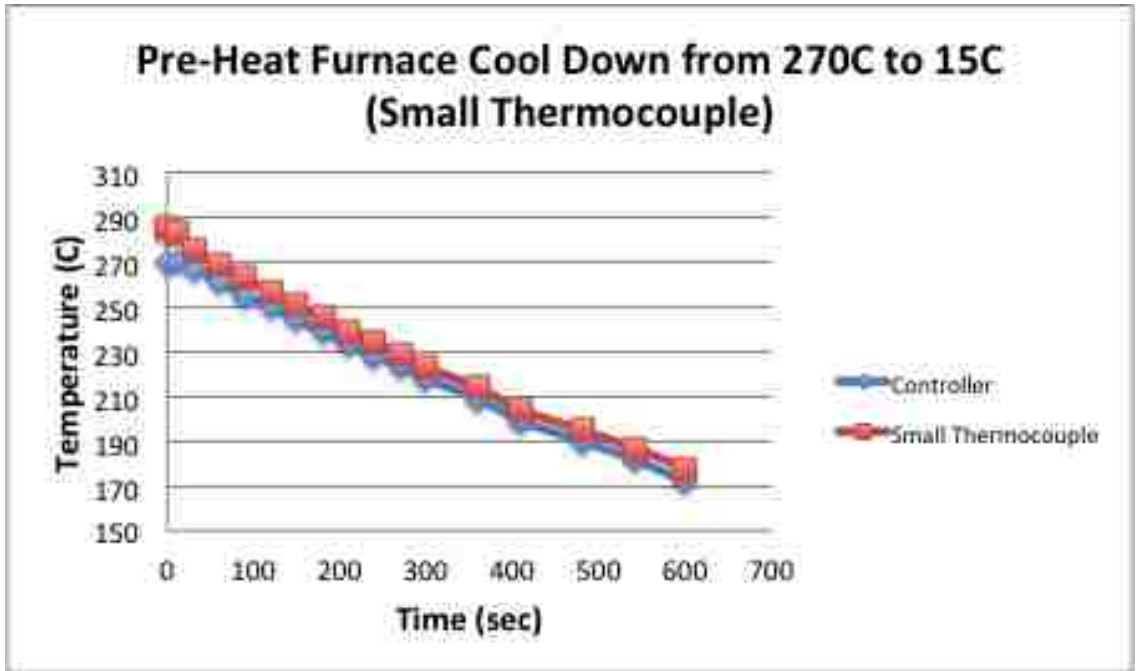
Figure 3.5: *Pre-heat furnace cool down time from 270°C to 15°C, with the small thermocouple.*

Figure 3.5 provides a representation of the cool down period for the pre-heat furnace. For this test, the controller temperature set point was adjusted to 15°C then the furnace was allowed to cool on its own. The furnace was kept in the on position during the entire test. The graph shows a gradual slope from the current temperature (270°C) down to the 15°C set point. Both the controller and the thermocouple averaged 4°C/min cool down rate. It can also be seen from the graph that at the lower temperatures, the thermocouple-controller temperature difference decreased from 16°C to 6°C.

The next set of tests is the same characterization as above, but with the larger diameter thermocouple. This was done due to general dissimilarities across different thermocouples. Figure 3.6, shown below, shows the ramp time from room temperature to the 260°C set point.
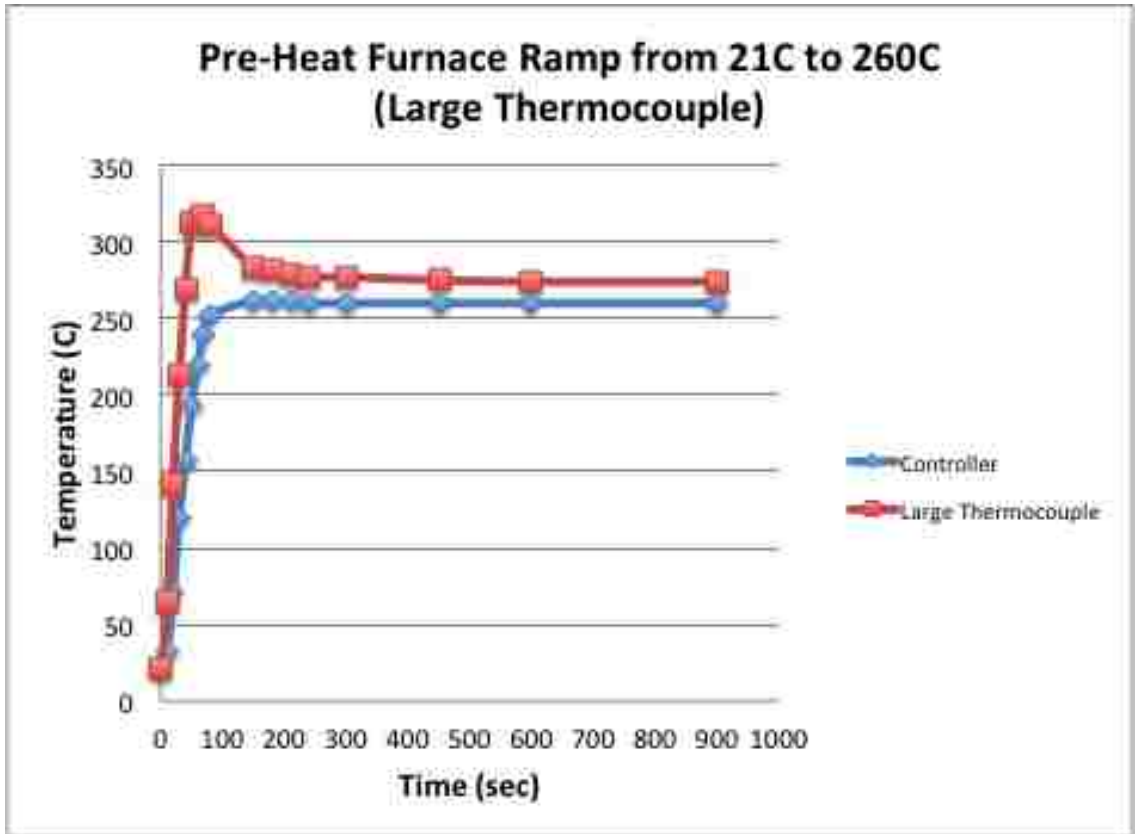
Figure 3.6: *Pre-heat furnace ramp time from 21°C to 260°C, with the large*

thermocouple.

As described in Figure 3.6, the thermocouple jumps to a max temperature of 317°C

within a minute as the controller maxes out at 262°C within two minutes. Overall, the test

yields a very similar result as with the small thermocouple (Figure 3.3). There is still a

temperature difference of 14°C after they both stabilize.

The following graph illustrates the ramp from 260°C to 270°C in the pre-heat

furnace, this time utilizing the large thermocouple.
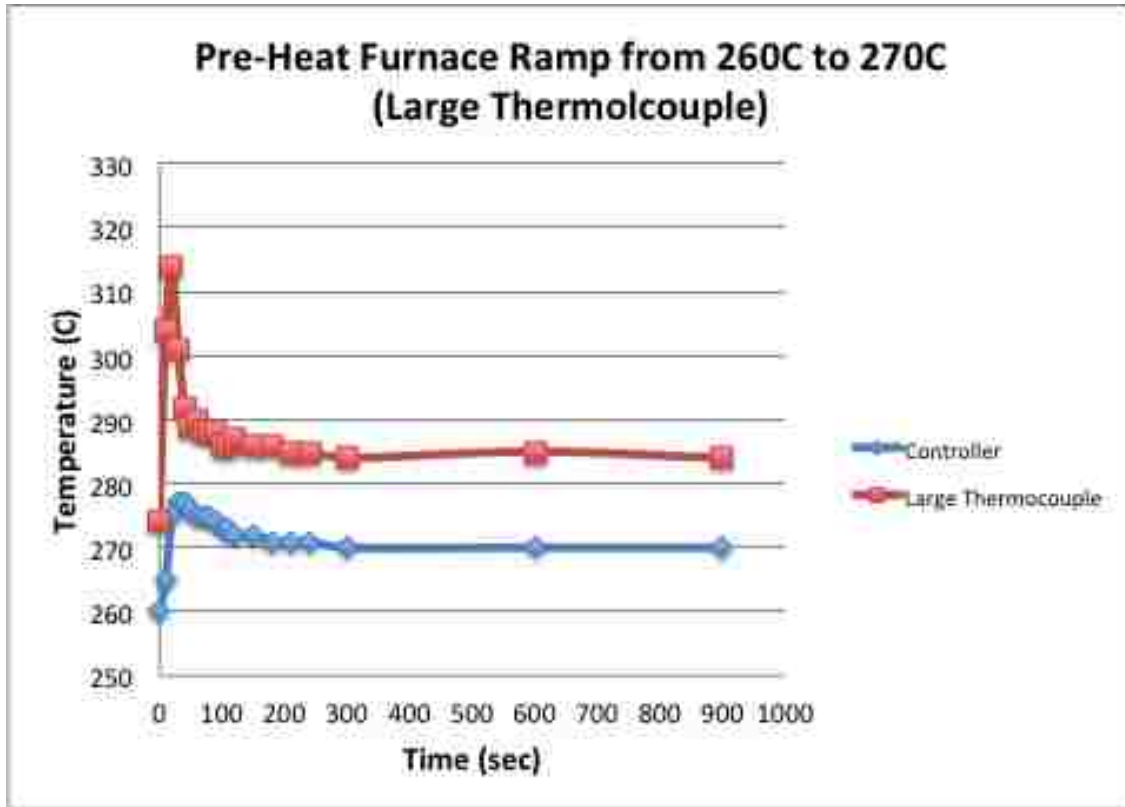
Figure 3.7: *Pre-heat furnace ramp from 260°C to 270°C, with the large thermocouple.*
As before, the large thermocouple mirrors that seen with the small thermocouple, with only minor differences. It can be seen that the large thermocouple, again, abruptly jumps to a higher temperature than that of the controller before eventually settling down. The max temperature in this instance is 314°C for the large thermocouple and 277° for the controller. Similarly, the stabilization temperature separation between the two is 15°C.

The cool down time with the large thermocouple was also recorded. The results of this test can be seen in Figure 3.8.
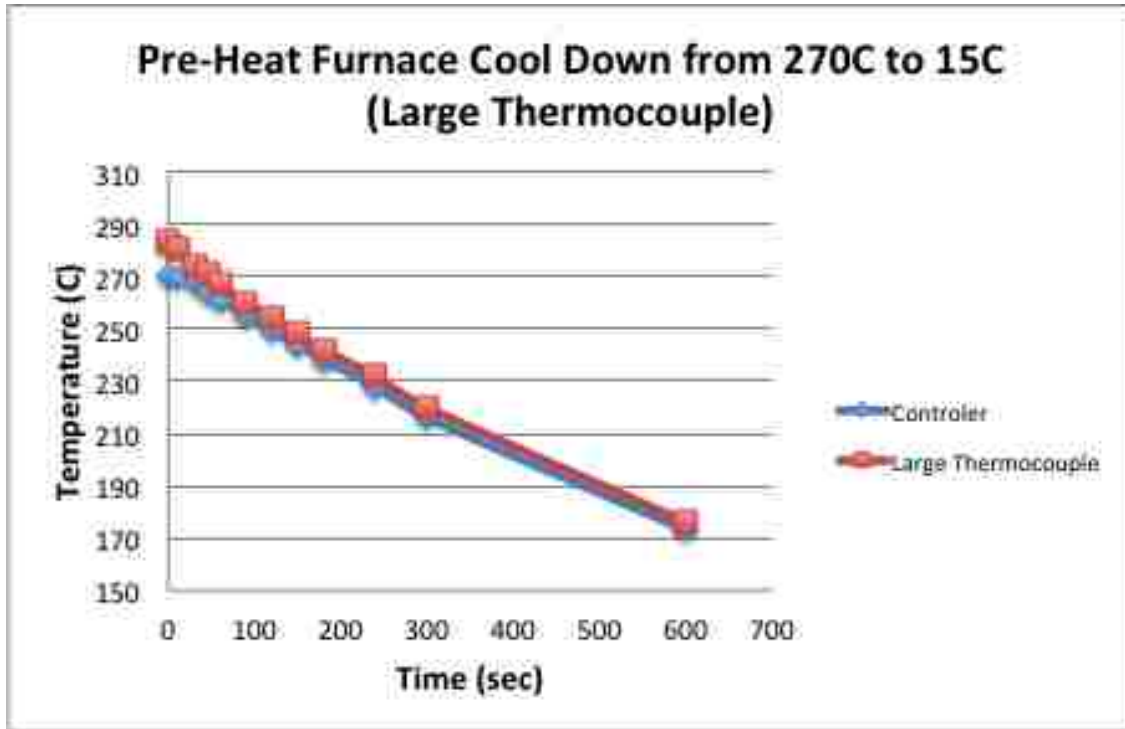
Figure 3.8: *Pre-heat furnace cool down time from 270°C to 15°C, with the large*

thermocouple.

Overall, it took about ten minutes for the pre-heat furnace to come back down to room

temperature (~22°C). This was seen with both thermocouples. Similarly, the cool down

rate was about 4°C/min for both the thermocouple and the controller. Also seen is the

degree of separation between the thermocouple and the controller is reduced at lower

temperatures. The final temperature difference at the end of this test was only 3°C.

Last in the characterization process was to determine the temperature spectrum

across the length of each furnace. This would allow the operators to know where to place

the samples during flight. The overall length of each furnace was 12.7 cm (5 in.). The

center of the furnace, prior to investigation, was assumed to be the hottest location.

Therefore, the center of each ampoule was measured to line up precisely with the center

of each furnace when placed inside. Due to the average length, 3.2 cm (1.26 in.) of the

ampoules the samples can be within 1.6 cm (0.63 in.) of the center of the furnace. This is because the samples are not adhered to the inside of the ampoule walls and are free to move within the confines of their ampoule as shown in Figure 3.2. This aspect of the Quencher is completely uncontrollable as any minor bump or jostle of the ampoule during operation will cause the samples to move around. Consequently, it is essential to determine the temperature range that the samples will be subjected to when the controller is at a particular set point. Figure 3.9 depicts the temperature spectrum across the length of the pre-heat furnace using both thermocouples.
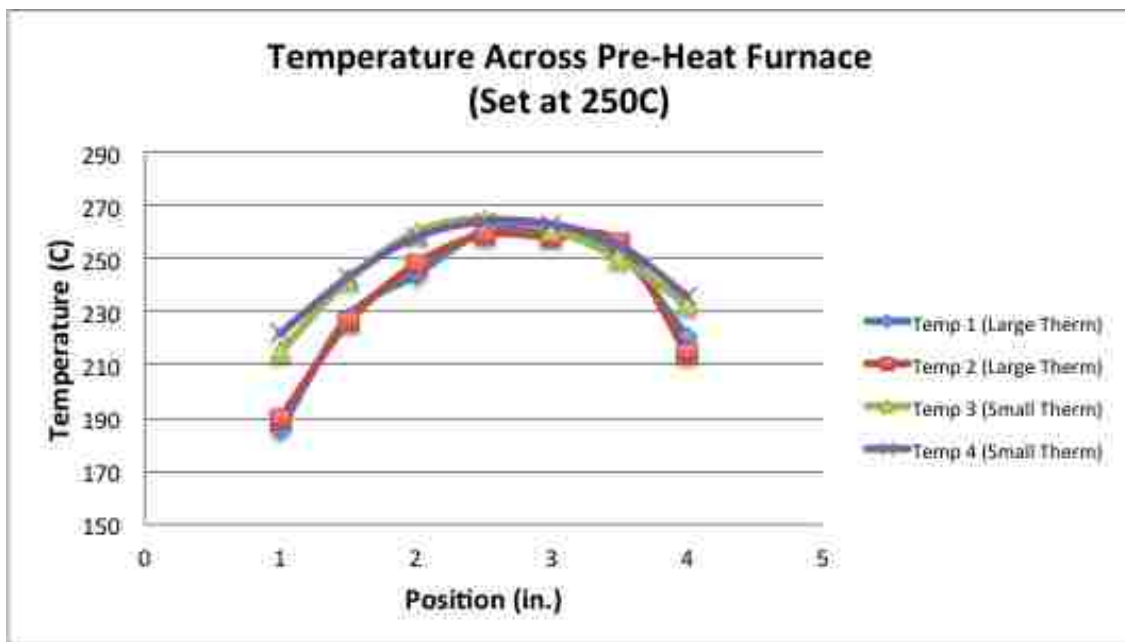
Figure 3.9: *Temperature spectrum across pre-heat furnace set at 250°C.*

Since the pre-heat furnace is only set at 250°C during the entire duration of the experiment that temperature was only one characterized. The x-axis of the graph (Figure 3.9) reads by position into the furnace from left-to-right. An example would be at 1 in. (2.54 cm) the sample is precisely 1 in. (2.54 cm) into the furnace from the left end. Since the furnace is 12.7 cm (5 in.) long the center of the furnace is 6.35 cm (2.5 in.). The shape

on the graph shows that the temperature is hottest directly in the center of the furnace.

Also, most of the temperatures are above the set point. This was predictable as the

thermocouples always recorded a higher temperature than the controller's set point

during previous testing. At this temperature range, the thermocouple was expected to read

about 15°C higher than the controller, based on the previous characterization testing.

3.4 Annealing Furnace

The purpose of the annealing furnace is to raise the temperature of the sample to

the applicable testing temperature while in 0-g or 1.8-g depending upon the test matrix

described in Section 3.7. The sample will be in this furnace for the duration of the desired

gravity level. Prior to exiting the desired gravity level, the specimen will be pushed out of

the annealing furnace and immediately quenched with a wet sponge. The annealing

furnace was characterized in the same manner as the pre-heat furnace. The same

thermocouples were also used. Figure 3.10 shows the annealing furnace ramp from room

temperature to a set point of 280°C.
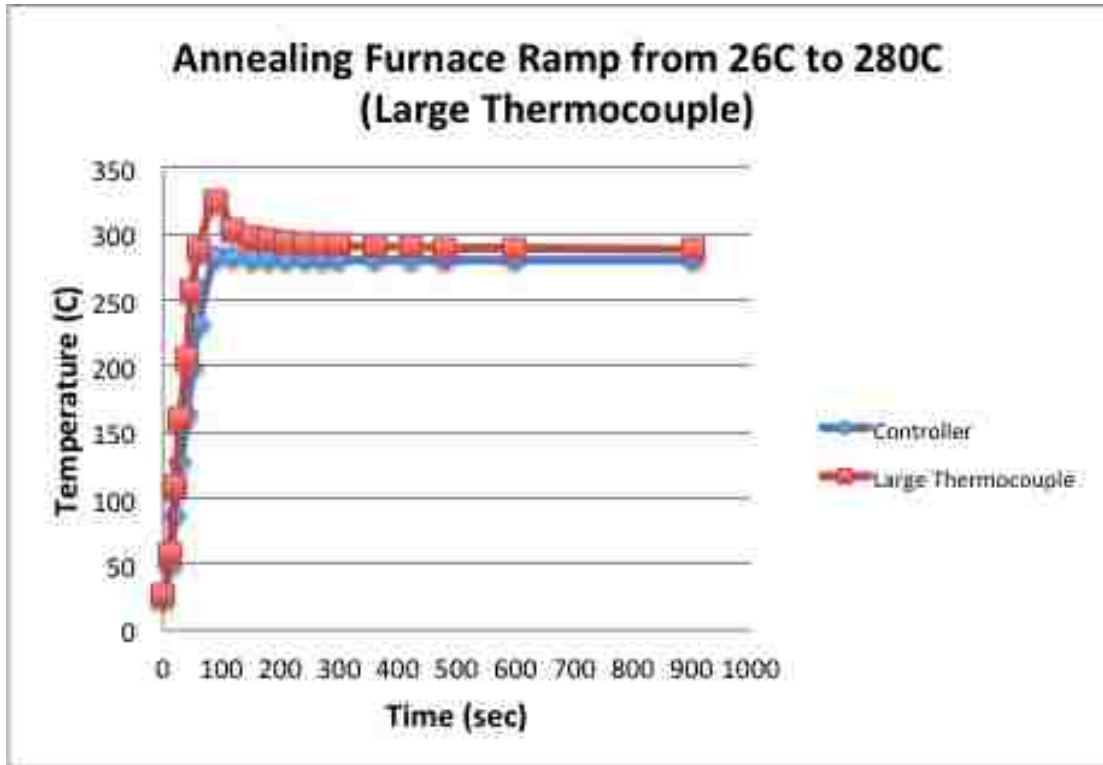
Figure 3.10: *Annealing furnace ramp time from 26°C to 280°C, with the large*

thermocouple.

As seen in Figure 3.10, the temperature quickly jumps up to above the set point, but

eventually levels out to the desired temperature. The thermocouple reads a higher

temperature initially (325°C) but eventually settles down to just above the set point

(288°C). The controller reaches the set point within 3 minutes for the thermocouple, the

set point is never reached but stabilizes within 6 minutes.

The next step in characterizing the annealing furnace was to increase the

temperature by 20 degrees. This would show how quickly the furnace would adjust to a

small temperature change. Figure 3.11 shows the annealing furnace ramp from 280°C to

the new set point of 300°C.
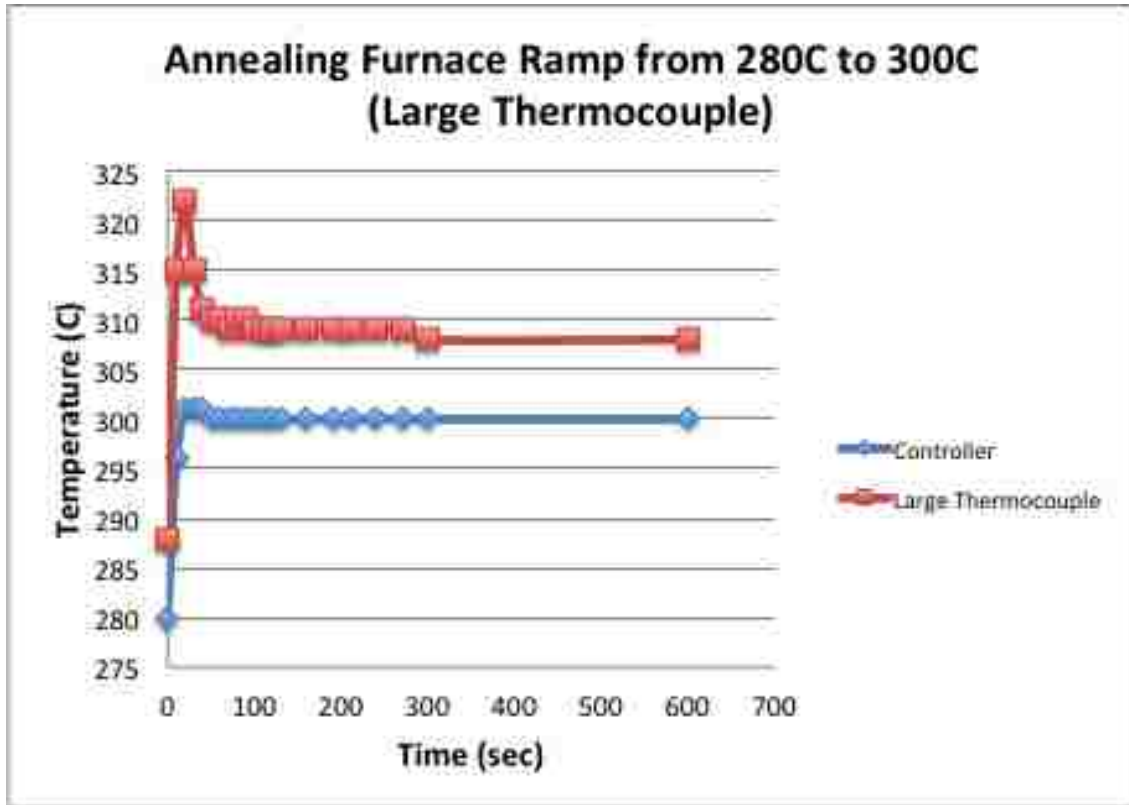
Figure 3.11: *Annealing furnace ramp time from 280°C to 300°C, with the large*

thermocouple.

As depicted in Figure 3.11, the thermocouple reading spikes to a much higher

temperature than the controller reading does. Similar to findings with the pre-heat furnace

characterization, the thermocouple read a few degrees higher than the controller. The

thermocouple read an initial high of 310°C within 90 seconds of recording while the

controller peaked at 301°C and leveled off within 60 seconds. The thermocouple leveled

off at a higher temperature of 308°C. The eight degree difference was also noticed in

previous characterization testing.

The annealing furnace was also characterized at higher temperature increments, to

determine how quickly the furnace would react when previously at a high temperature.

Figure 3.12 shows the ramp time of the annealing furnace from 400°C to 450°C.
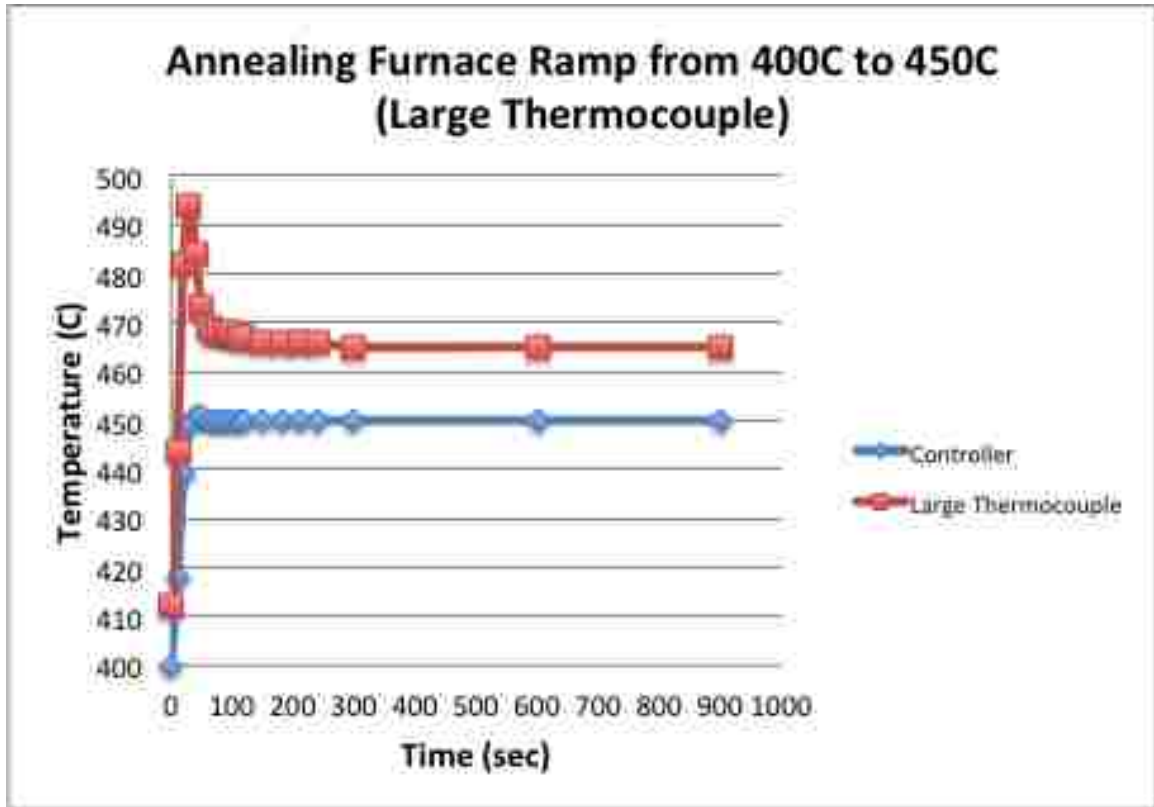
Figure 3.12: *Annealing furnace ramp time from 400°C to 450°C, with the large*

thermocouple.

As previously seen, the thermocouple reads a higher temperature than the controller set

point. At the higher temperature, the thermocouple settles at 465°C as apposed to the

controller set point of 450°C. A 15 degree separation was noticed at this temperature

setting. Both readings seemed to settle within one minute of recording, while the

thermocouple dropped a degree a minute to its final stabilization temperature.

The last ramp time for the characterization of the annealing furnace was a 600°C

to the set point of 650°C. This can be seen in Figure 3.13.
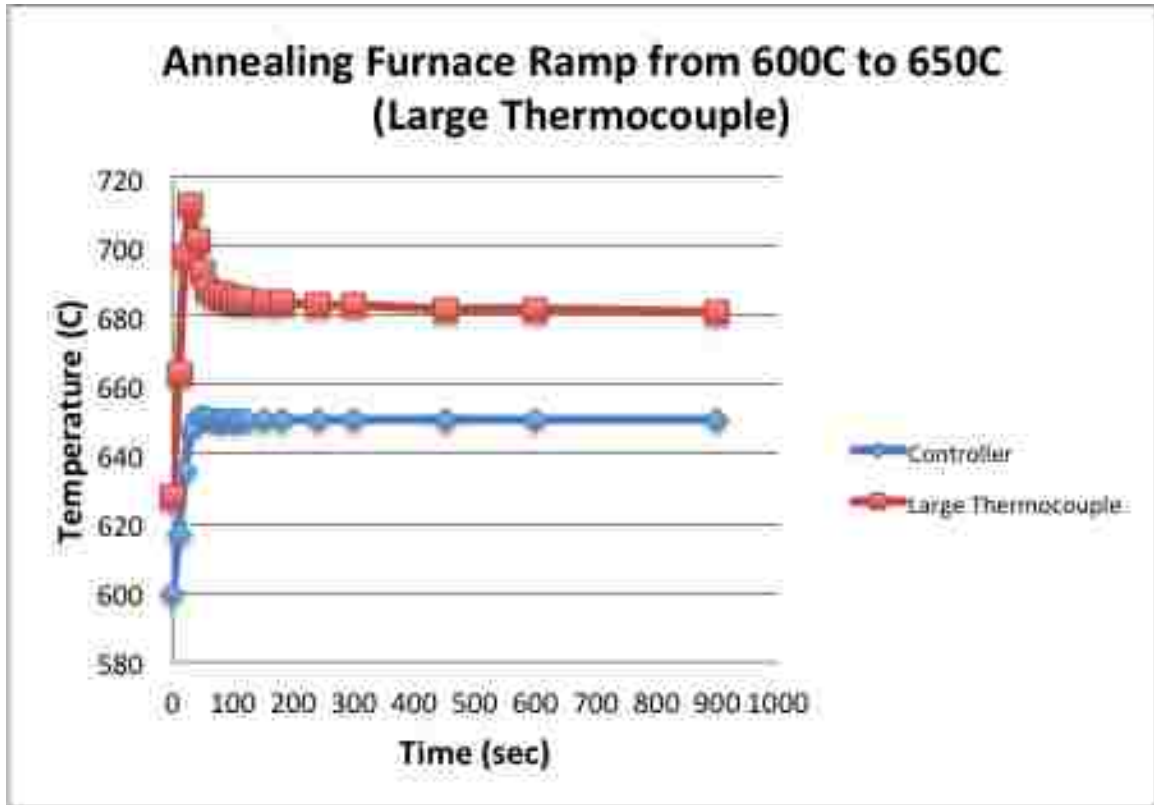
Figure 3.13: *Annealing furnace ramp time from 600°C to 650°C, with the large*

thermocouple.

As seen in Figure 3.13, the final thermocouple temperature (681°C) is much higher than

that of the controller set point (650°C). This difference was higher than the previous

annealing furnace ramp test from 400°C to 450C. That particular test only had a 15

degree separation; for this new test, the separation was 31 degrees. Both the controller

and the thermocouple settled within a reasonable time, of approximately one minute.

The last characterization test completed on the annealing furnace was the

temperature across the length of the furnace. Like previously done on the pre-heat

furnace, this was done to determine the temperature spectrum across the furnace. Also

like the pre-heat furnace, the temperature was not the same at every location. The overall

length of the Annealing furnace was also 12.7 cm (5 in) and the temperatures were taken

in 1.27 cm (0.5 in.) increments from 2.54 cm (1 in.) into the annealing furnace. Figure

3.14 below shows the temperature range for the annealing furnace set at 300°C and

similarly in Figure 3.15 for a set point of 600°C.
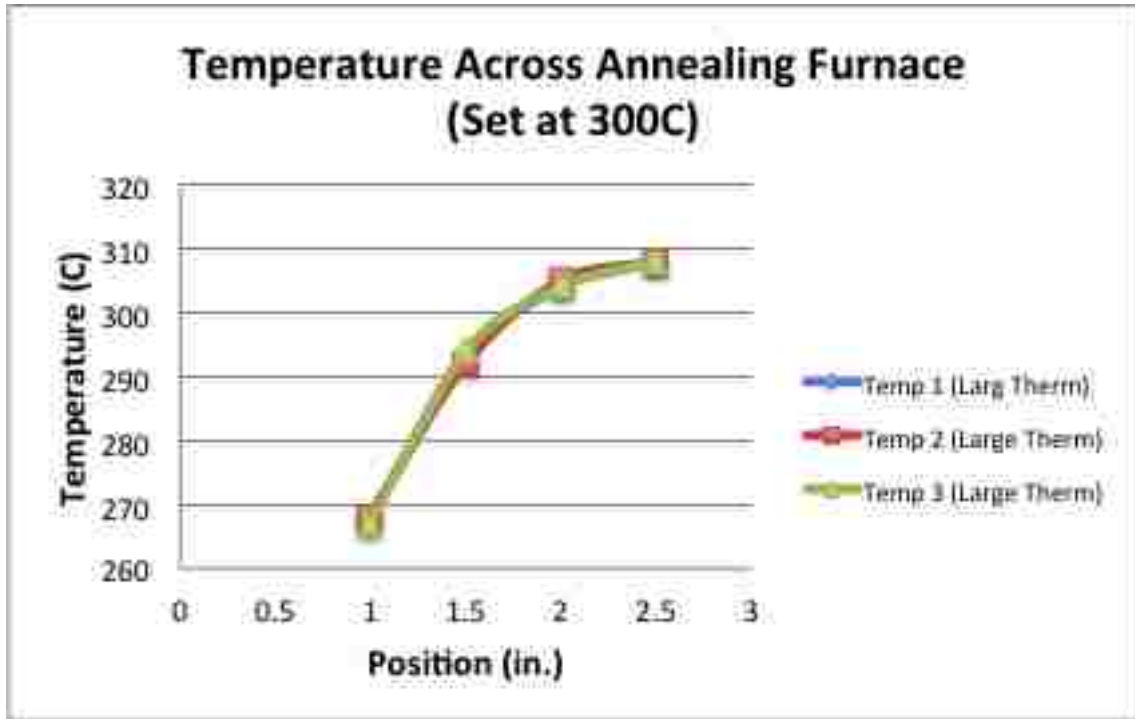
Figure 3.14: *Temperature across the annealing furnace set at 300°C.*
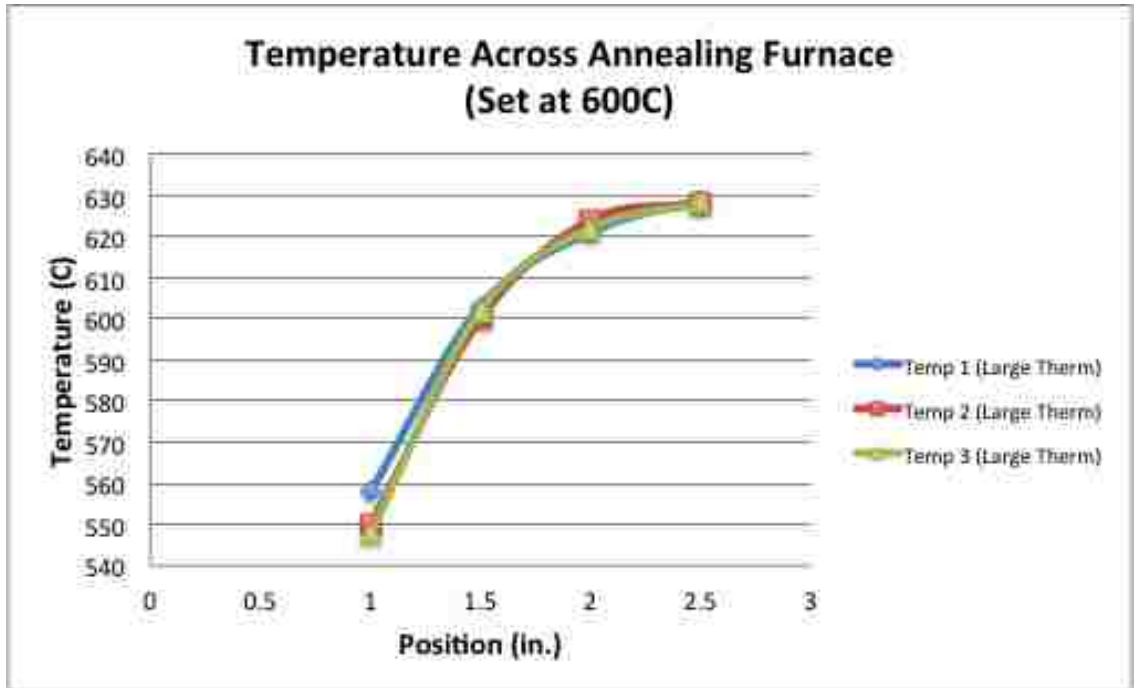
Figure 3.15: *Temperature across annealing furnace set at 600°C.*

Both of these characterization tests were only done with the large thermocouple

due to the lack of high temperature protective sheathing of the small thermocouple. Also

shown in both graphs is that the temperature was only recorded up to the midpoint of the

furnace. This was due to the thermocouple leads undesirably touching inside the furnace.

Due to the Plexiglass housing of the Quencher the annealing furnace isn't as accessible as

the pre-heat furnace, thus making it difficult to fit the thermocouple in the small opening.

This caused inaccuracies to be displayed by the thermocouple reader once beyond the

midpoint of the furnace. Both figures show at least a 100 degree difference from the

middle of the furnace to the center. The results from the lengthwise characterization

suggest that the middle of the furnace is the optimum location for the ampoule placement.

Although the annealing furnace tests only provide data up to the midpoint, it can be

conjectured that the results would be similar to the Pre-Heat furnace. Both results, however, show that the optimum place for the ampoule is the center of the furnace.

3.5 Materials

The material used for this research is a fluorozirconate glass of the Heavy Metal Fluoride Glass (HMFG) family known as ZBLAN (ZrF_4-BaF_2-LaF_3-AlF_3-NaF). The ZBLAN was purchased from OgMentum Inc. [OgMentum, Inc]. The item number purchased was ZMP-800/1000. As discussed in Section 2, this type of glass readily crystallizes in a 1-g environment. Therefore, each sample will have a small amount of initial crystallization prior to testing. The ZBLAN samples were cleaved to size and inserted into the glass ampoules for testing on the parabolic aircraft.

3.6 Material Characterization

In order to gain a better understanding of the materials being used, DSC testing was completed. The DSC testing will provide essential information such as the glass transition temperature (Tg), the crystallization temperature (Tx), and the melting temperature (Tm). This information will provide better insight about the material as well as aid in developing the experimental test plan. The results from the DSC study will also be compared to results obtained by other authors. The DSC testing was completed by FAI Materials Testing Laboratory, Inc. [FAI Mat. Testing Lab. Inc.]. The ZBLAN samples were analyzed in duplicate from 35°C up to 600°C at two different heating rates, 20°C/min and 10°C/min. The DSC plots for the ZMP-800/1000 ZBLAN samples can be seen in Figures 3.16 and 3.17.

71
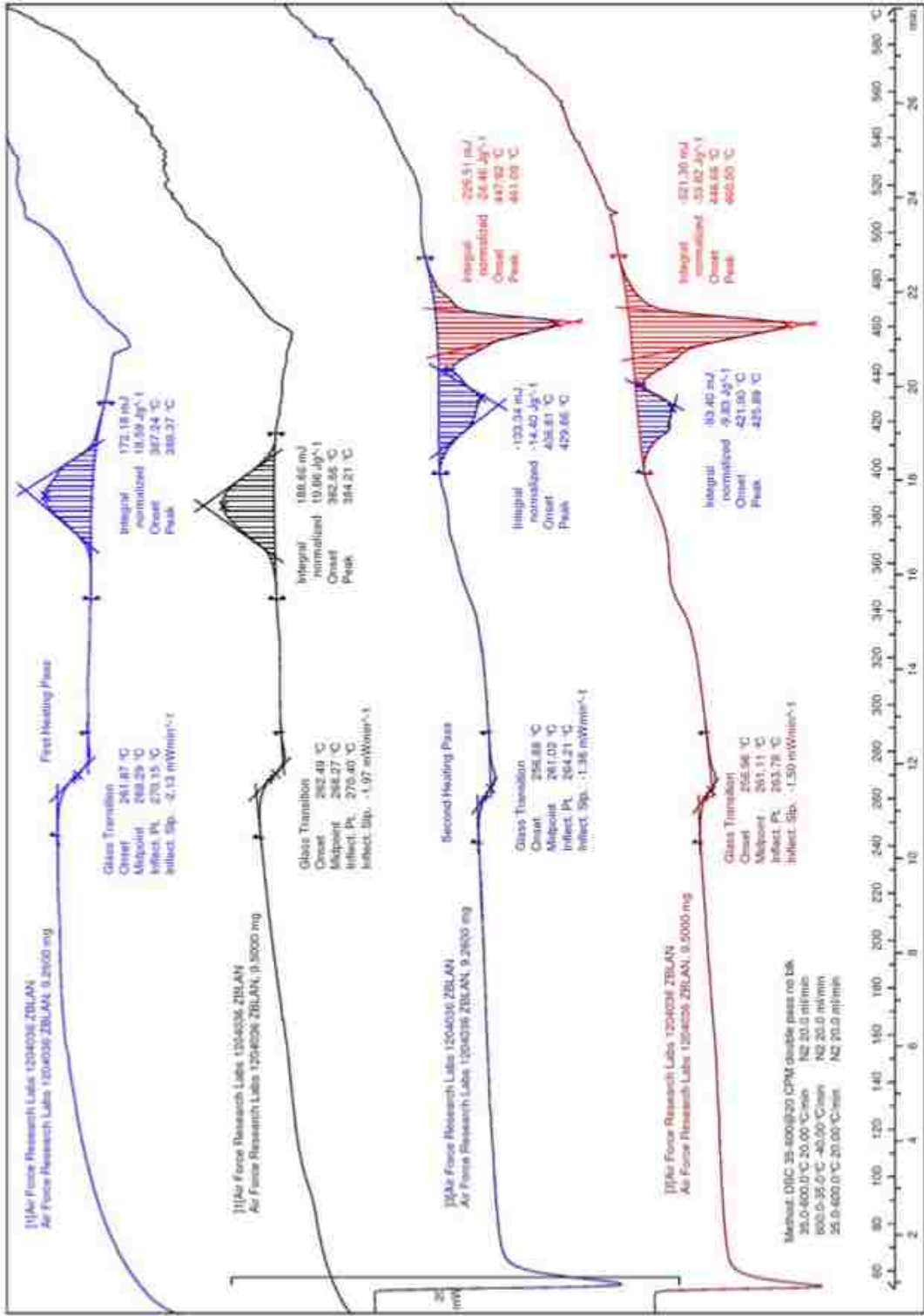
Figure 3.16: *DSC thermal curve for ZBLAN at 20°C/min.*
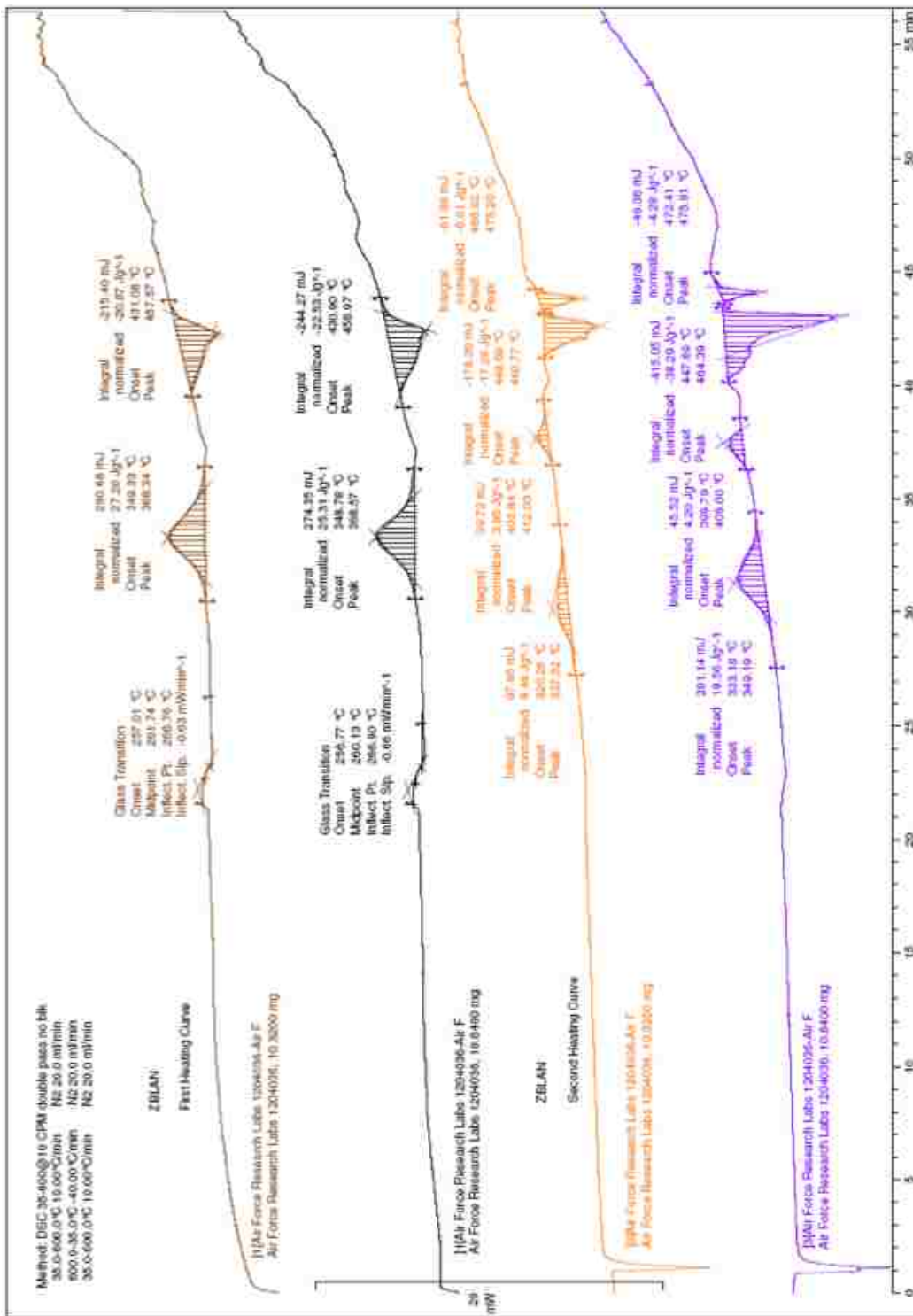
Figure 3.17: *DSC thermal curve for ZBLAN at 10°C/min (first run).*
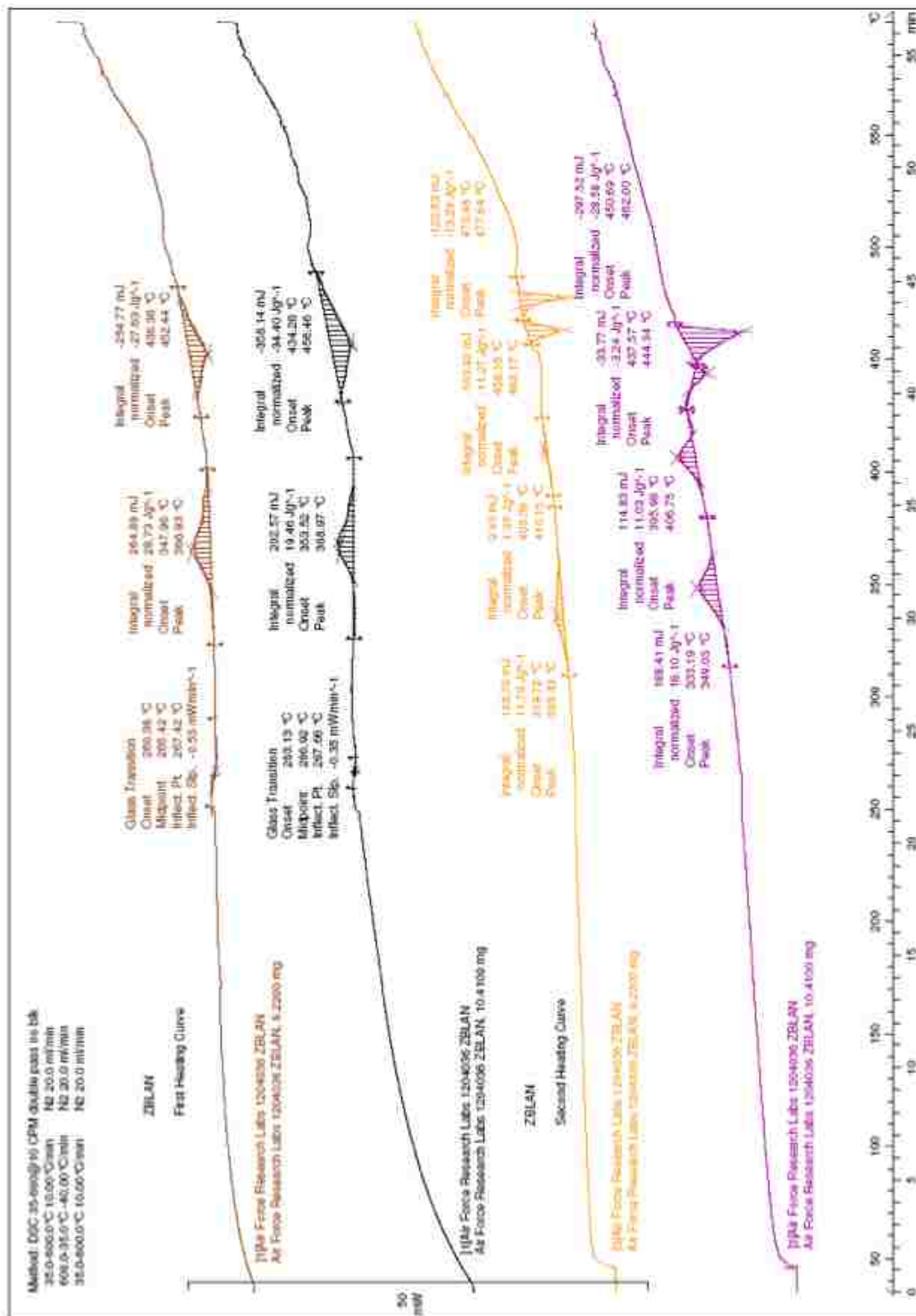
Figure 3.18: *DSC thermal curve for ZBLAN at 10°C/min (second run).*

74

Each sample was heated from 35°C up to 600°C, then cooled. This process was repeated to produce a second heating curve. The proper way to read each figure is that, the first heating curve is the top most curve, then the second heating curve, for the same sample, is the third from the top. The heating curves in between the aforementioned heating curves are for the duplicate sample. The results from the ZBLAN DSC study show that the both the glass transition temperature and the crystallization temperature are dependent upon the heating rate. Two separate runs were completed for the 10°C/min heating rate to ensure repeatability. The 10°C/min heating rate initiates the Tg (261°C) and Tx (368°C) earlier rather than the 20°C/min heating rate initiates the Tg (268°C) and Tx (386°C) later.

The overall purpose of the DSC testing is to determine the transition temperatures of the materials being used. Once this information is obtained, the experimental test matrix can be developed. The average temperature data gained from the DSC can be seen in Table 3.1.

Table 3.1: *Average DSC results for ZBLAN.*

Heating Rate	Average Peak Tg (°C)	Average Peak Tx (°C)
10°C/min	261	368
20°C/min	268	386

The results from DSC testing were as expected. Harrington [Harrington, 2007] reported the glass transition, Tg, for ZBLAN to be 265°C. This is within the range of data collected from the DSC characterization. Nakao *et al.* [Nakao, 1991] completed their own DSC analysis for ZBLAN and reported the crystallization temperature, Tx, to be 375°C.

This is also within the bounds of the DSC results obtained for this study. Overall, the DSC results obtained are as expected and consistent with documented results.

3.7 Experimental Procedure

The in-flight Quencher operation required two operators, one to load the samples and operate the controllers and the second to quench and store the samples. The operation consisted of the following steps (dependent upon test matrix, Table 3.2/3.4).

Once the ampoule is loaded into the end of the pushrod the pushrod is manually translated to the center of preheat furnace for the duration of either the 0-g or the 1.8g sections of the flight. After the sample has been pre-heated the pushrod is relocated to the center of the annealing furnace for the duration of the gravity level under testing. Lastly, the pushrod is extended out the end of the annealing furnace, and the glass ampoule is grasped with a damp sponge and removed from the pushrod. This final process simultaneously quenches the sample as the operator removes the ampoule from the pushrod. This entire process will take place during the 0-g/1.8g sections of the parabolic flight.

The test matrix for both flights was developed based on a temperature scheme that spanned just below the glass transition temperature (Tg) to well above the crystallization temperature (Tx). Both the microgravity and hyper-gravity portions of the parabolas were used as variables in the experiment. According to Varma *et al.* (2001) and Tucker *et al.* (1997) ZBLAN samples processed in hyper-gravity have higher crystal growth than those processed in unit gravity. These results suggest that the crystallization temperature has been lowered. To support this hypothesis, the ZBLAN samples processed below the crystallization temperature (270°C – 350°C) were processed in hyper-gravity. All other

temperatures were processed in the microgravity environment. The test matrix for flight 1 can be seen in Table 3.2.

Table 3.2: Test matrix for flight 1.

Test #	Quencher Temp Set Point (°C)	G-level	Expected Outcome
1	250/270	hyper-g	
2	250/290	hyper-g	Early
3	250/310	hyper-g	crystallization
4	250/330	hyper-g	(< Tx 1-g)
5	250/350	hyper-g	
6	250/360	0-g	
7	250/360	0-g	
8	250/400	0-g	
9	250/450	0-g	Suppressed
10	250/500	0-g	crystallization
11	250/550	0-g	(> Tx 1-g)
12	250/600	0-g	
13	250/650	0-g	

All tests described in the test matrix had two samples per test (enclosed in a glass ampoule), as described previously. As shown in Table 3.2, the Quencher temp set point column contains two different temperatures. The values correspond to the left (pre-heat furnace) and right (annealing furnace) set points. The pre-heat furnace set point remained constant for the duration of the experiment. The annealing furnace temperatures correspond to the 'testing temperatures' at the desired gravity level. One of two expected outcomes was also noted in the table. The expected results of the first set of tests (hyper-g) were to see if crystallization would initiate earlier than the 1-g crystallization temp (360°C) in a hyper-g environment. The second set of tests were developed to determine if

crystallization can be suppressed in a 0-g environment and at what temperature will

crystallization occur regardless of the 0-g environment.

The test matrix for flight 2 was developed based on observations from the flight 1

test results (Section 4). The first change was the size of temperature increments used and

the range of the temperature scheme. The maximum temperature from flight 1 was 650°C

whereas for flight 2 it was 450°C. Select temperatures were duplicated for a baseline

comparison (290°C, 310°C, 350°C, 360°C and 400°C). The test matrix for flight 2 can be

seen in Table 3.3. The same expected outcomes were noted as in the previous test matrix.

Table 3.3: Test matrix for flight 2.

Test #	Quencher Temp Set Point (C)	G-level	Expected Outcome
1	250/290	hyper-g	
2	250/300	hyper-g	
3	250/310	hyper-g	Early
4	250/320	hyper-g	crystallization
5	250/340	hyper-g	(<Tx 1-g)
6	250/350	hyper-g	
7	250/360	hyper-g	
8	250/360	0-g	
9	250/360	0-g	
10	250/365	0-g	
11	250/370	0-g	
12	250/375	0-g	
13	250/380	0-g	Suppressed
14	250/390	0-g	crystallization
15	250/400	0-g	(>Tx 1-g)
16	250/410	0-g	
17	250/420	0-g	
18	250/430	0-g	
19	250/440	0-g	
20	250/450	0-g	

3.8 Summary

Two microgravity parabolic flights were completed in the summer of 2012, which consisted of 40 parabolas each. Between the two flights, 33 tests were completed, which consisted of both hyper-gravity and microgravity testing. Each test had two samples of material confined in the testing ampoule for redundancy. Identical, 1-g, testing was also completed for comparison.

The characterization information yielded two primary results. The first being the optimum location to place the ampoules during testing and, the second, providing key information in order to develop the test matrix. Due to the nature of the Zero-G Corporation's parabolic flight regimen, certain aspects of the characterization process were essential. Due to time constraints, all tests temperatures had to be completed in ascending order. From the characterization process, it was determined that the cool date rate is not quick enough to transition to a lower temperature. However, the characterization tests showed that minor (5°C – 50°C) jumps could be completed within 2 minutes. Since the 0-g sections occur approximately every 20s seconds in a 10 parabola set, some parabolas had to be skipped in order for the annealing furnace to settle to the set temperature.

The results and analysis obtained from this experiment are discussed in Section 4.

CHAPTER 4 – Results and Analysis

This section discusses the results obtained from the experimental program (Chapter 3) and an in depth analysis of the results.

4.1 Optical Microscopy

A series of optical microscopy techniques were used to investigate the crystallinity of the ZBLAN samples processed on board the parabolic aircraft. The ZBLAN samples were removed from their glass ampoule housing then placed lengthwise into the microscope. The primary data investigation technique used was phase contrast optical microscopy at 100X magnification. Phase contrast microscopy works by introducing a stained slide, which enhances the contrast of the image. This process highlights essential features, such as crystals and other cellular structures not apparent in standard microscopy. Each micrograph was taken with a constant light intensity and constant focus, to minimize sample to sample image variability. The microscope model used is an Olympus BX51, which has a built-in stained slide for phase contrast microscopy. Control sample micrographs were taken prior to any testing. Figure 4.1 shows the ZBLAN control sample.

Figure 4.1: *ZBLAN control sample.*

As shown in Figure 4.1, the ZBLAN control sample is relatively clear of any

crystals. The control sample is a ZBLAN sample that hasn't been subjected to any heat

treatment. Some minor inclusions were noticed on the top half of the sample. This

suggests some minor initial crystals formed during the glass syntheses process. Each

micrograph was further processed to better quantify the light transmissivity. This was

done with an open source image-editing program titled ImageJ. ImageJ allowed the user

to select a given area of the image and plot the 'gray value' of each pixel along the

distance selected. The term gray value refers to black and white intensity level of each

individual pixel within the image. A value of zero refers to a completely black pixel and a

value of 250 refers to a completely white pixel. Since white light is transmitted through

the sample from the microscope, the gray value is representative of the light

transmissivity of each sample. Also, where the sample has more inclusions (crystallites)

the light transmission will be lost and show a lower gray value (i.e. darker pixel). Figure

4.2 shows the control sample with the targeted area for plotting the light transmissivity

plot.
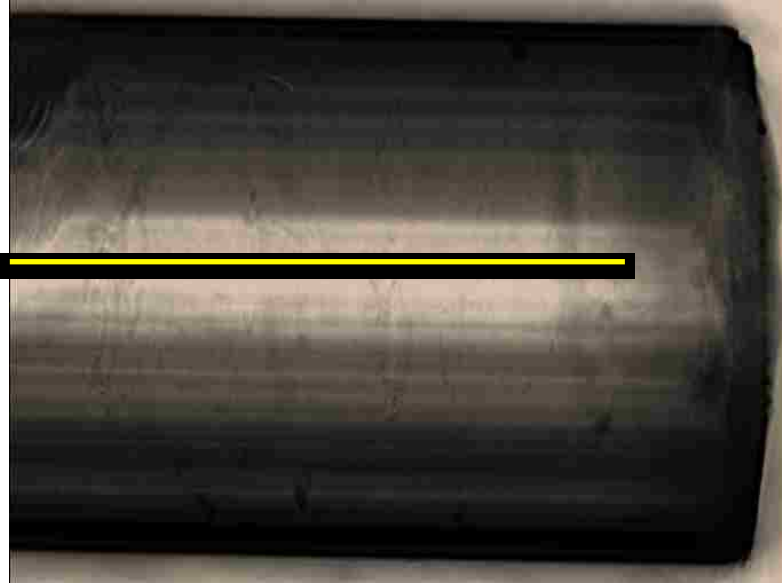
Figure 4.2: *ZBLAN control sample with target area for plotting the light transmissivity.*

The target area is within the confines of the rectangle in the middle of the image. The

target area will remain constant for all further images in order to standardize the

following transmission (gray value) graphs. The center of each image was selected as the

target area because it is the most clearly defined area within all of the images and

represents the light transmissivity of each sample at this focus level on the microscope.

Figure 4.3 shows the light transmission plot for the control sample.
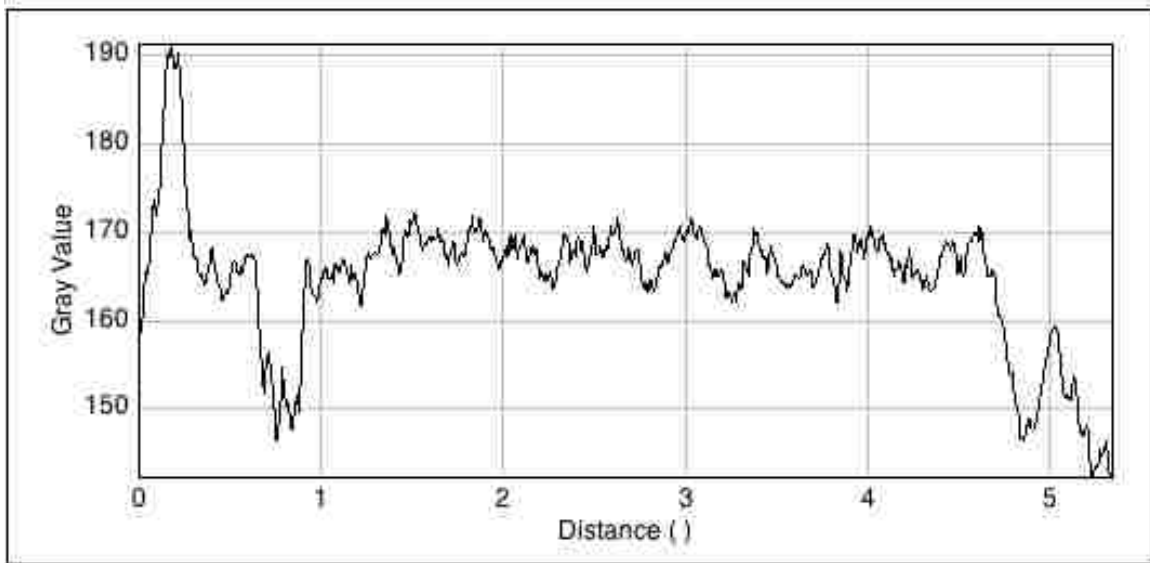
Figure 4.3: *Light transmission (gray value) plot of the control sample.*

Figure 4.3 shows the gray value versus distance plot representing the light transmission

across the sample. The plot maintains an approximate constant gray value of

approximately 165. This gray value is then compared to the 0-g and 1-g samples.

The first 0-g temperature tested was at 360°C. Figure 4.4 shows both the 0-g (top)

sample and the 1-g (bottom) sample heated to 360°C for the same time duration.
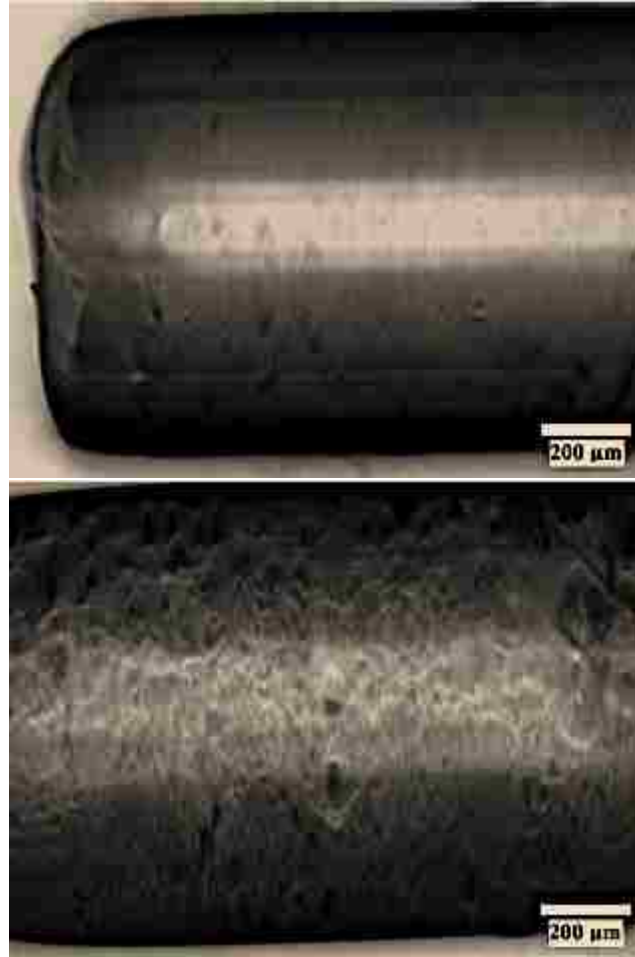
Figure 4.4: 0-g ZBLAN sample (top) and 1-g ZBLAN sample (bottom) at 360°C.

It can be observed in Figure 4.4 that the 0-g sample is relatively clear and free of any

features. The sample is similar to that of the control sample (Figure 4.1). The 1-g sample

at the same temperature has clearly crystallized, as well lost its previous spherical shape.

The 1-g sample has developed wavy texture consistent with Wilson *et al.* [Wilson, 1985].

Wilson *et al.* describe crystal growth in ZBLAN at 330°C as, 'radiating structures in the

bulk', which is comparable to what is apparent in Figure 4.4 (1-g, bottom). Figure 4.5

shows the comparison of the light transmission plot for both samples represented in

Figure 4.4.
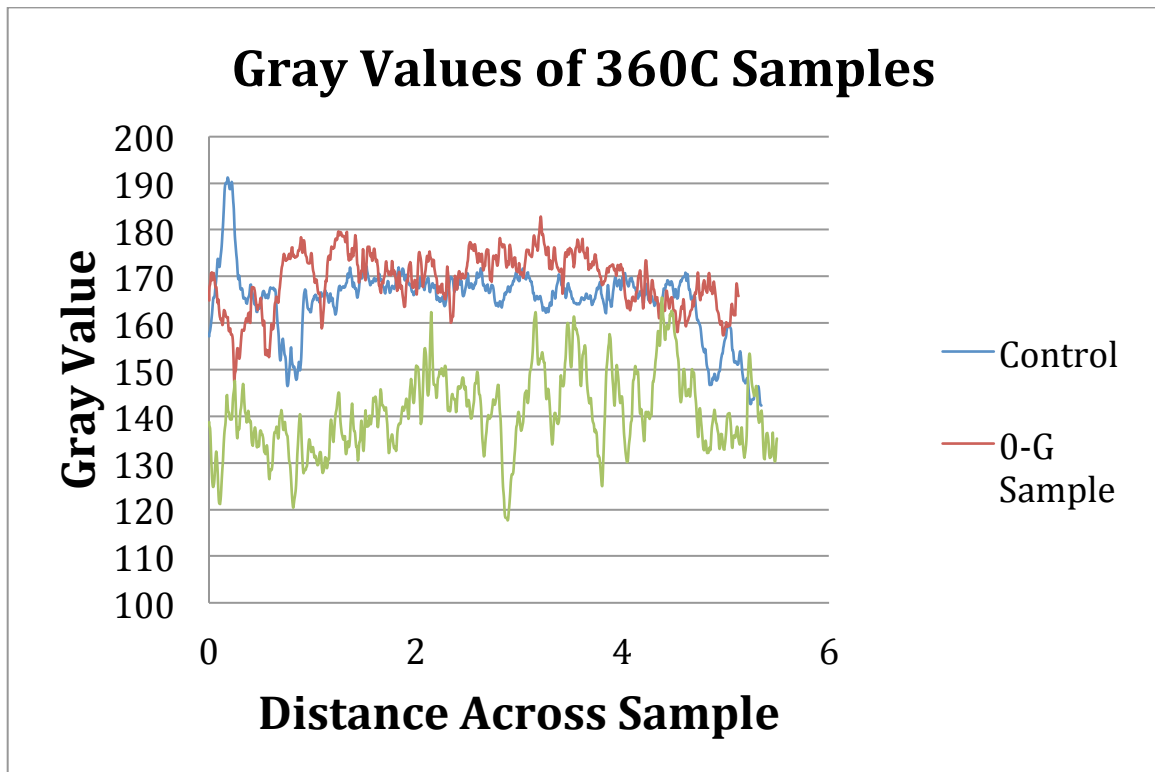
Figure 4.5: *Transmission plot of 0-g ZBLAN sample and 1-g ZLBAN sample at 360°C.*

As seen in Figure 4.5, the 0-g processed fiber has an overall higher gray value of approximately 160, which is the average gray value for the control sample, whereas the 1-g processed fiber has an average gray value of approximately 135.

Next, in sequence, a ZBLAN sample was heated to 370°C in 0-g (top) and in 1-g (bottom). The results can be seen in Figure 4.6.
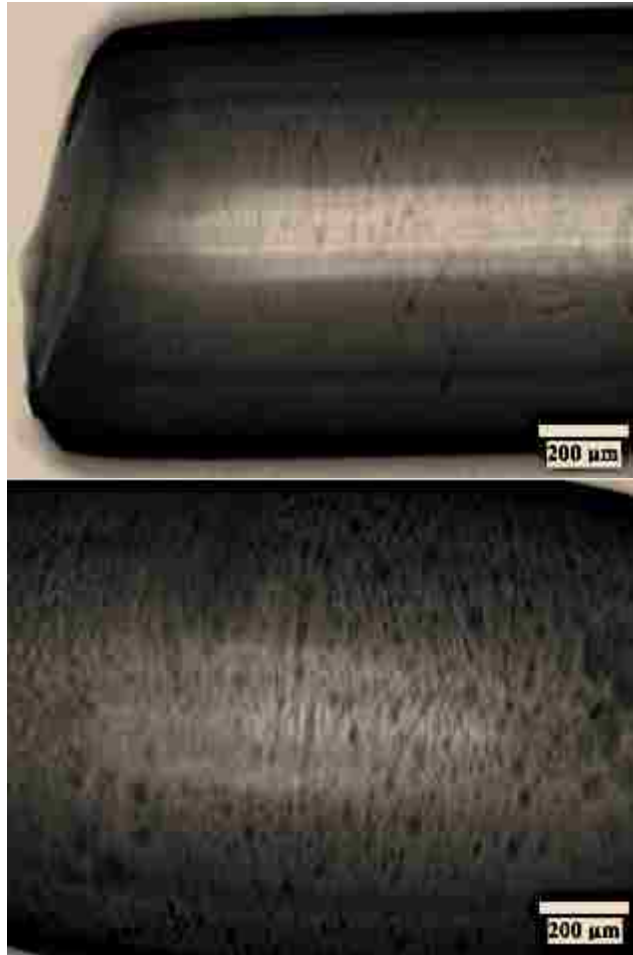
Figure 4.6: *0-g ZBLAN sample (top) and 1-g ZBLAN sample (bottom) at 370°C.*

Shown in Figure 4.6 is that the 0-g sample continues to hold its shape and is relatively

crystal free. Some slight texturing is beginning to form as well as some minor inclusions.

The 1-g however has the same wavy texture noticed in the 360°C sample. Figure 4.7

shows the light transmission plot for the aforementioned samples.
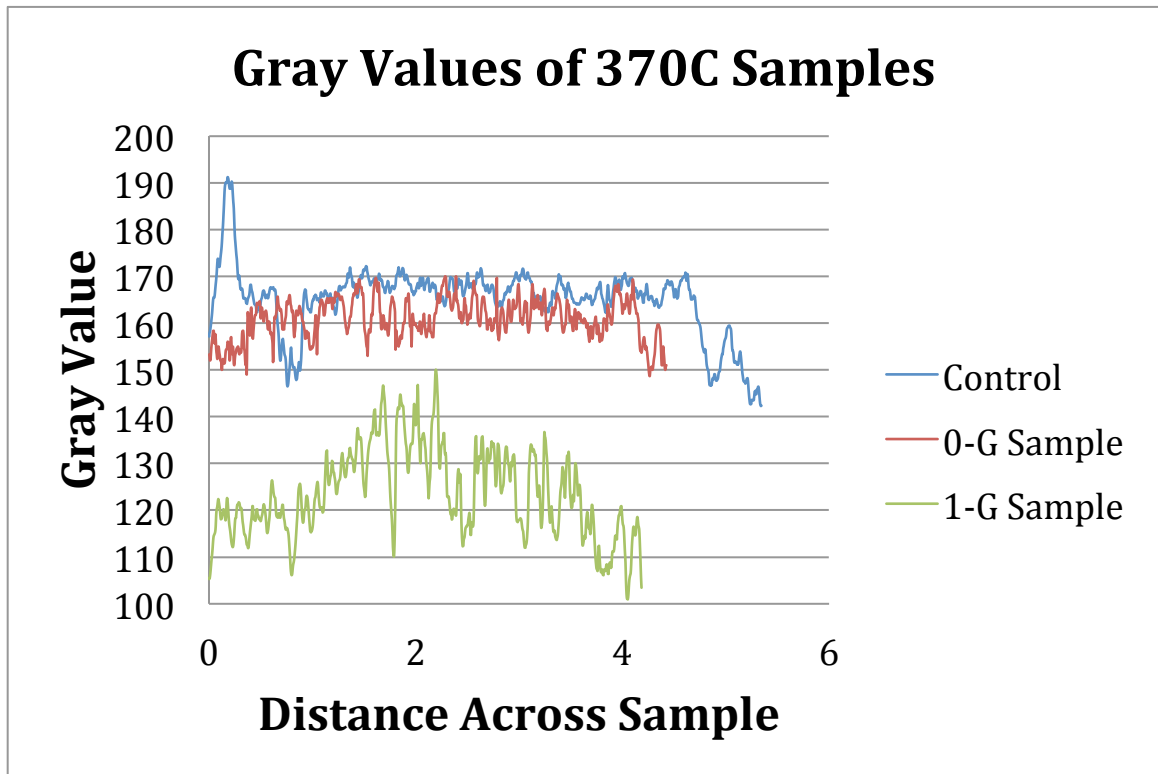
Figure 4.7: *Transmission plot of 0-g ZBLAN sample and 1-g ZLBAN sample at 370°C.*

Figure 4.7 shows similar outcomes to the 360°C processed samples. The 0-g sample has a higher gray value of 150 and is still relatively near the control sample, whereas the 1-g sample has a lower value of approximately 125.

Increasing the sample annealing temperature to 380°C, however, yields different results. Figure 4.8 shows the outcome obtained from a 380°C temperature treatment.
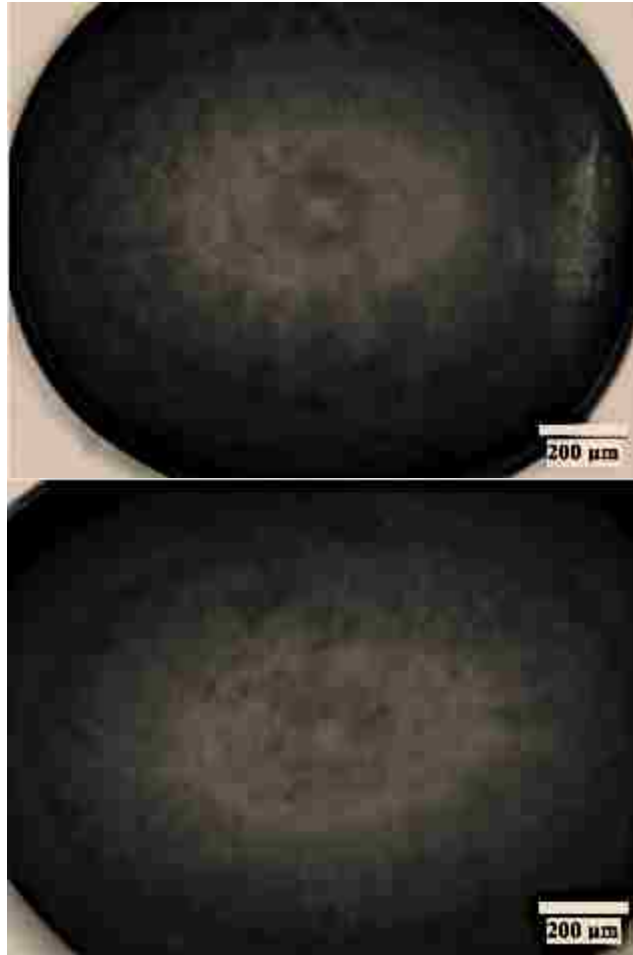
Figure 4.8: 0-g ZBLAN sample (top) and 1-g ZBLAN sample (bottom) at 380°C.

The 380°C 0-g sample has clearly lost its shape and has developed the same wavy texture as the 1-g sample. This is evidence that crystallization has now occurred for the 0-g sample as well. This demonstrates that crystallization has been suppressed in a 0-g environment, ultimately increasing the crystallization temperature. Gray value quantification graphs for these samples can be seen in Figure 4.9.
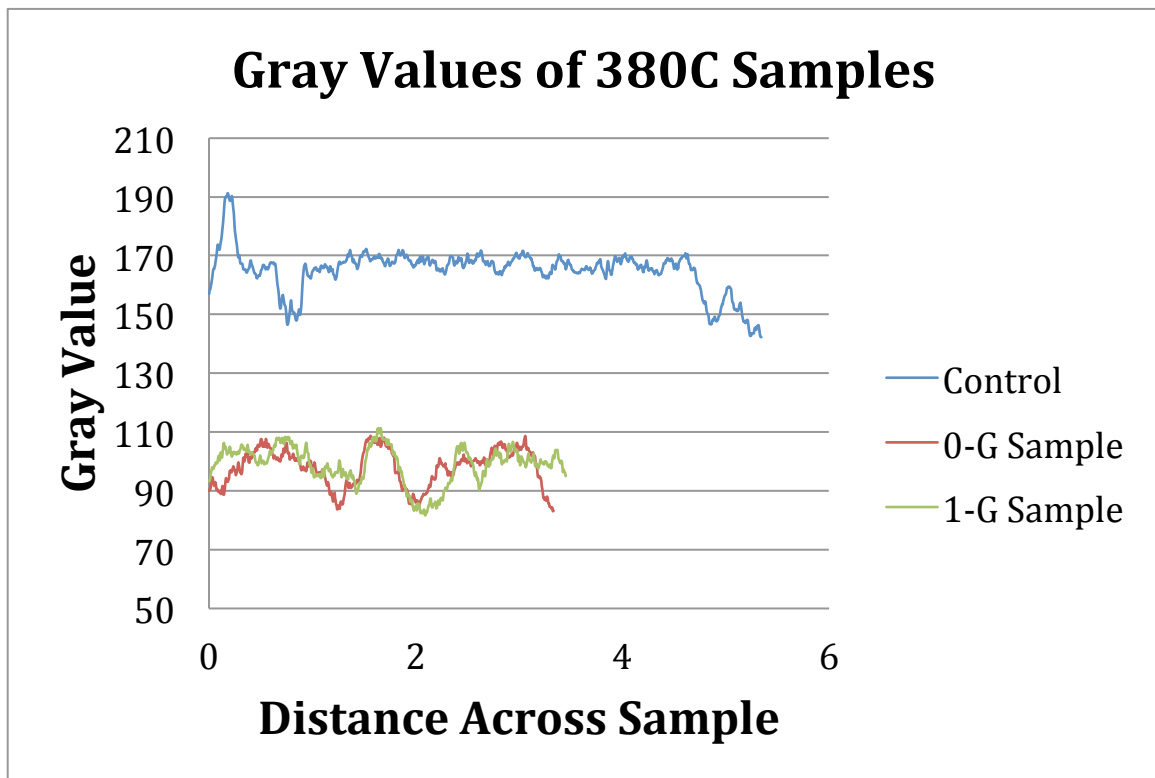
Figure 4.9: *Transmission plot of 0-g ZBLAN sample and 1-g ZLBAN sample at 380°C.*

Just as the micrographs show very similar outcomes of the 0-g versus the 1-g sample, so do the gray value plots for the respective samples. Both plots show an average gray value of near 100 and also have very similar patterns.

Taking the previous gray value plots and isolating the 0-g and 1-g samples in individual charts can be seen in Figure 4.10 and Figure 4.11 respectively.
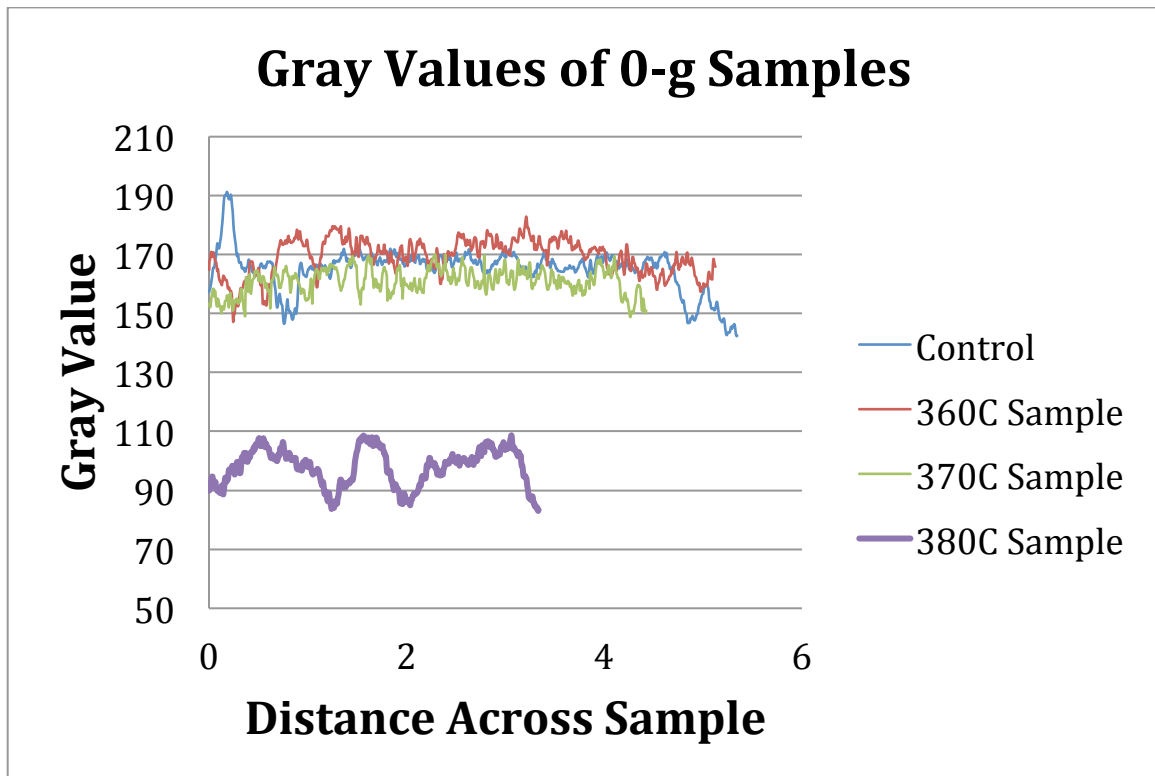
Figure 4.10: *Transmission plot of the three 0-g ZBLAN samples.*
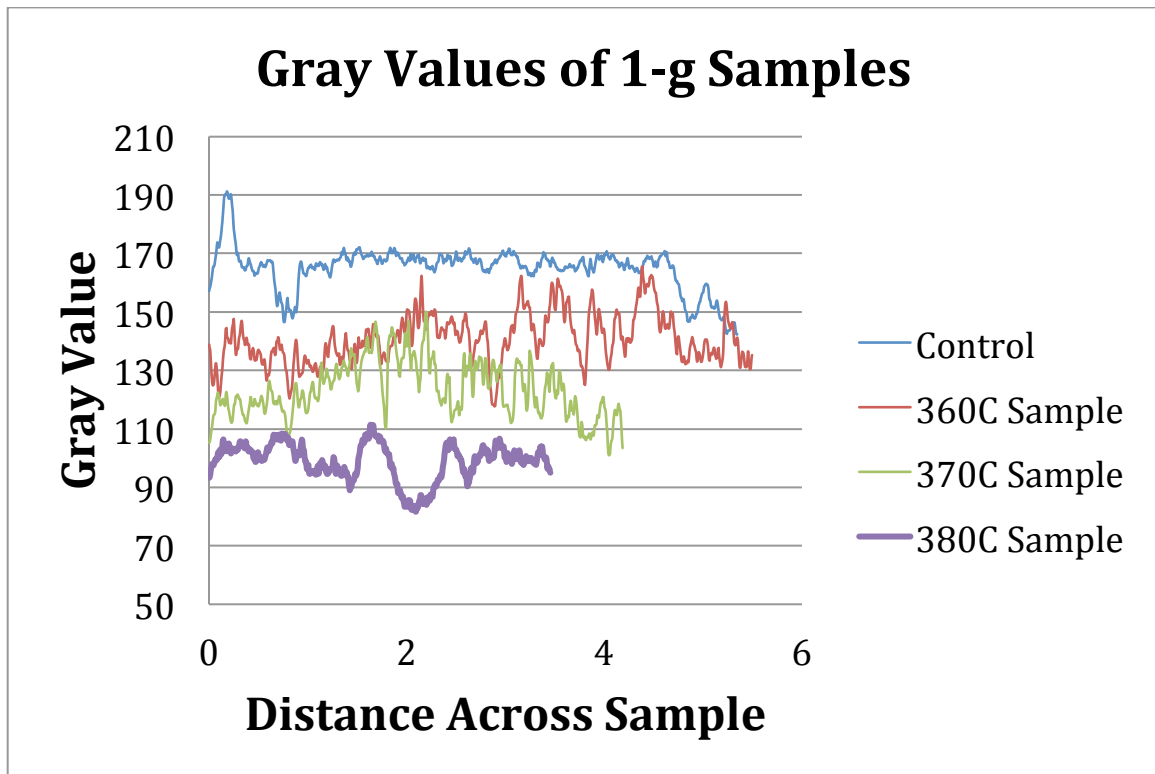
Figure 4.11: *Transmission plot of the three 1-g ZBLAN samples.*

Shown in Figure 4.10 is that the 360°C and 370°C samples maintain a consistent gray value with that of the control sample. However, the 380°C is the only outlier with a much lower gray value, evidence of sudden crystallization at approximately 380°C. Conversely, the 1-g samples don't maintain the same consistency with that of the control sample. Immediately the 360°C sample has started to shift downwards to lower gray values, which is also evidence of crystallization. Additionally, making a side-by-side comparison of the three relevant temperatures (360°C, 370°C, and 380°C) in 0-g and 1-g demonstrates the transition from amorphous glass to a crystalline glass, shown in Figure 4.12.
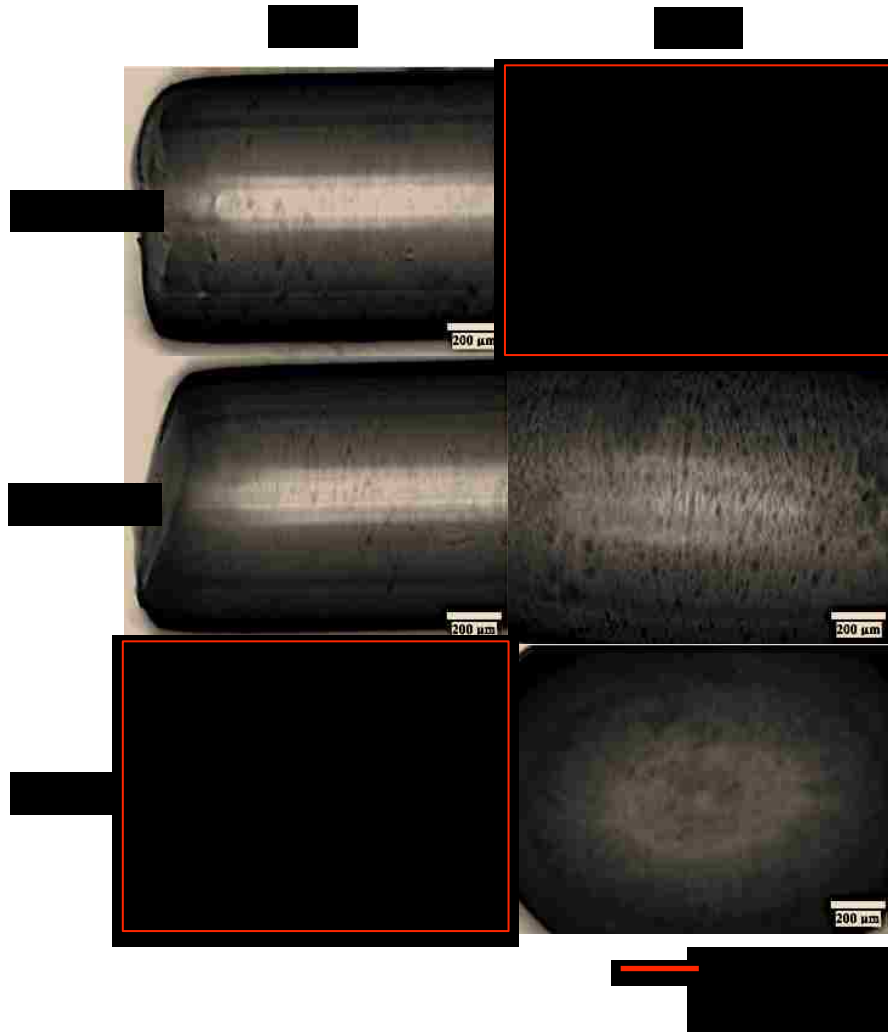
Figure 4.12: *Side-by-side comparison of micrographs that shows crystallization in 0-g vs. 1-g.*

As shown in Figure 4.12, comparing the relevant drawing temperatures processed in 0-g and 1-g, crystallization occurs at 380°C in 0-g whereas crystallization occurs at 360°C in 1-g. The first two samples (360°C and 370°C) samples in 0-g appear to only have minor inclusions and the 380°C sample has clearly crystallized as well as lost its previous cylindrical shape. The first (360°C) sample in 1-g has clearly crystallized by exemplified by the vast amount of inclusions and wavy texture not apparent in the corresponding 0-g sample.

Continuing to show samples higher in the temperature scheme is a sample processed at 410°C in 0-g and 1-g (Figure 4.13).
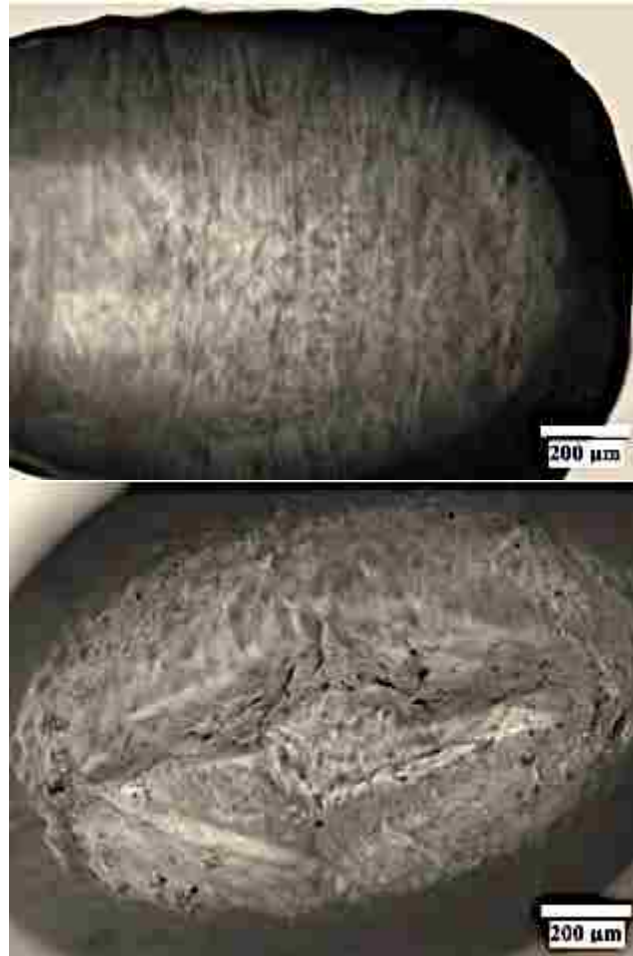
Figure 4.13: 0-g ZBLAN sample (top) and 1-g ZBLAN sample (bottom) at 410°C.

The 410°C samples both show an extreme loss of shape and a high polycrystalline structure. Similar to the samples processed at 380°C both the 0-g and 1-g samples have completely crystallized regardless of the gravity field present during the heat treatment. Gray scale plots at this stage are not relevant due to the high crystallinity of both of the samples. A high temperature processed sample, Figure 4.14, shows a ZBLAN sample processed at 550°C in 0-g (top) and 1-g (bottom).
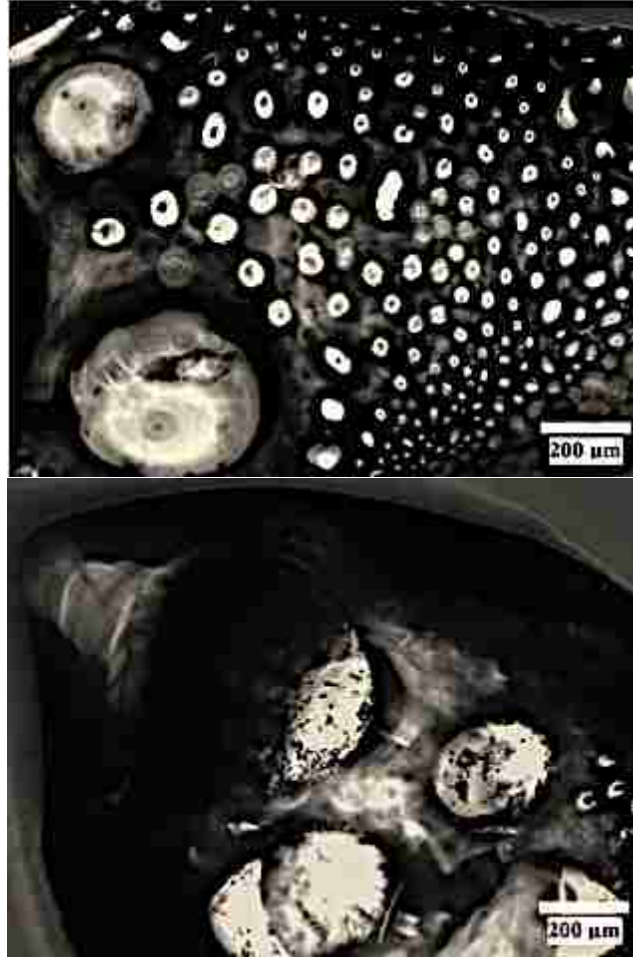
Figure 4.14: *0-g ZBLAN sample (top) and 1-g ZBLAN sample (bottom) at 550°C.*

Both samples shown in Figure 4.14 have both become polycrystalline solids with their crystal size on the order of 100–200 μm. The 0-g sample had multi-phase crystallization with a grouping of smaller crystals (50 μm) and large crystals (200 μm).

The hyper-g testing revealed that crystallization happens earlier than the 1-g samples, therefore shifting the crystallization temperature to a lower temperature. Figure 4.15 depicts the hyper-g and 1-g samples heated at 290°C.
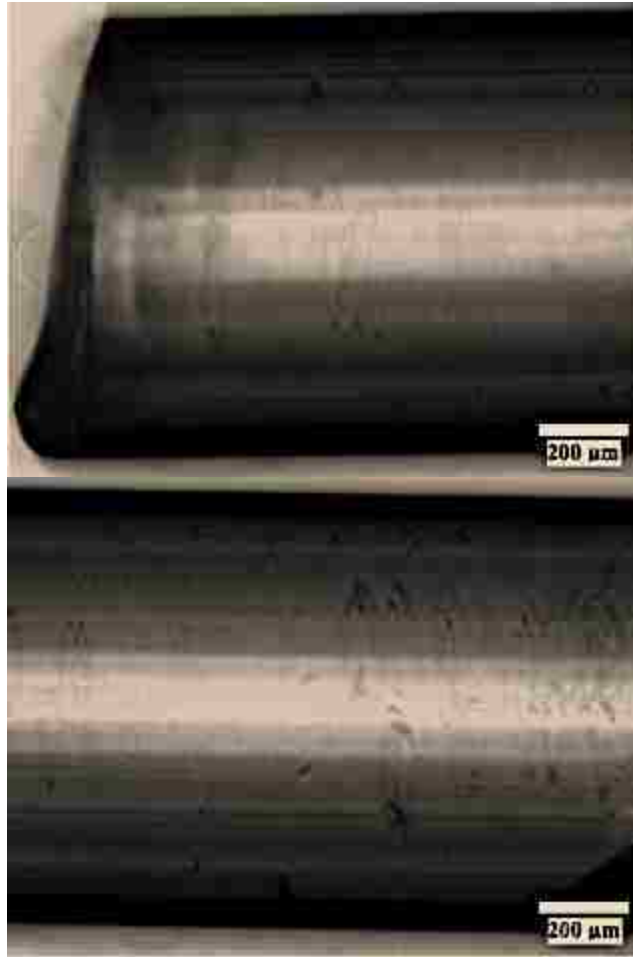
Figure 4.15: Hyper-g ZBLAN sample (top) and 1-g ZBLAN sample (bottom) at 290°C.

In Figure 4.15, the hyper-g (top) sample has a wavy texture suggesting crystallization has

occurred. Whereas, the 1-g (bottom) sample appears to be more clear than the hyper-g

sample. Thus, the hyper-g sample has begun crystallizing prior to the 1-g sample. Figure

4.16 shows the gray value plot for the micrographs shown in Figure 4.15.
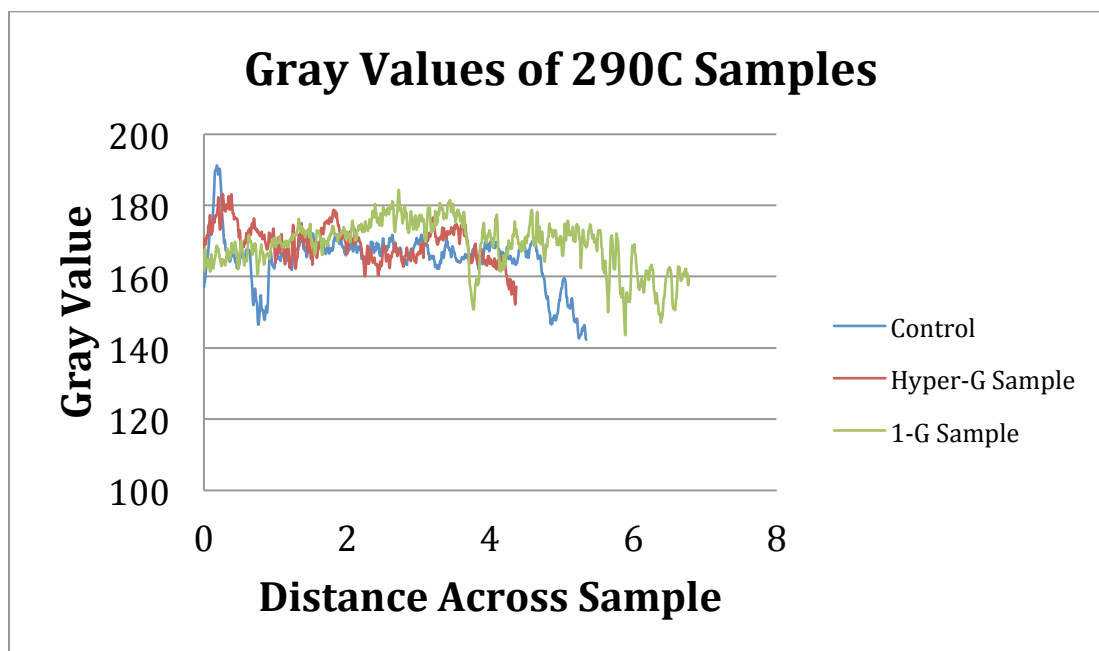
Figure 4.16: *Transmission plot of hyper-g ZBLAN sample and 1-g ZLBAN sample at*

290°C.

Figure 4.16 depicts the gray value plot for the first hyper-g sample. The hyper-g

processed sample shows a slightly lower gray value (150) than the 1-g processed sample

(160). This is evidence that the hyper-g sample has begun to crystallize prior to the 1-g

sample.

Figure 4.17 depicts the hyper-g and 1-g samples at 310°C.
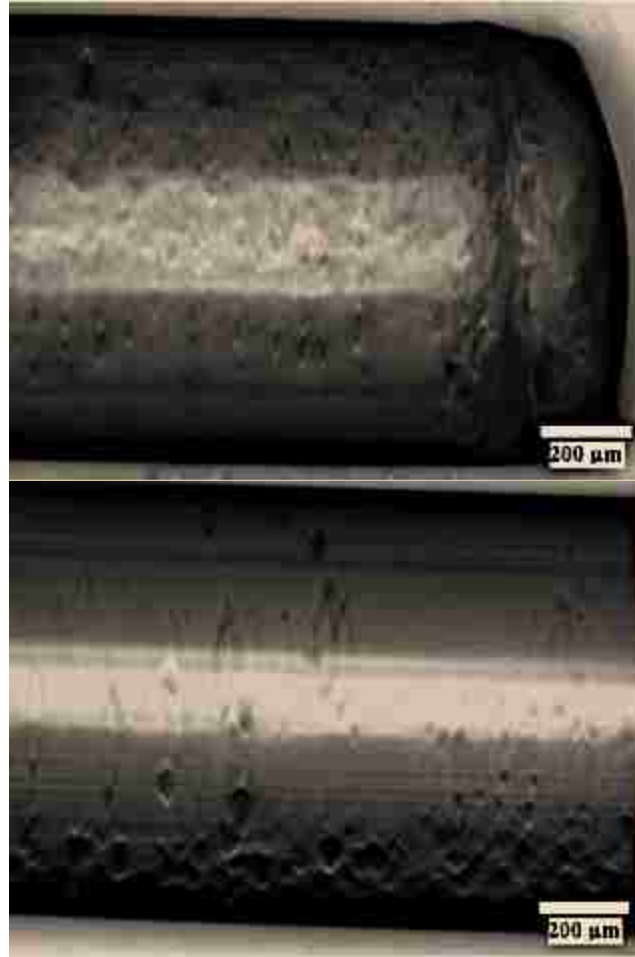
Figure 4.17: *Hyper-g ZBLAN sample (top) and 1-g ZBLAN sample (bottom) at 310°C.*
At a temperature of 310°C the hyper-g sample has clearly crystallized and the 1-g sample
shows onset of crystallization (evidenced by the wavy texture). Therefore, in a hyper-g
environment the ZBLAN crystallizes at a much earlier temperature than in 1-g. The
quantification of the gray value plots can be seen in Figure 4.18.
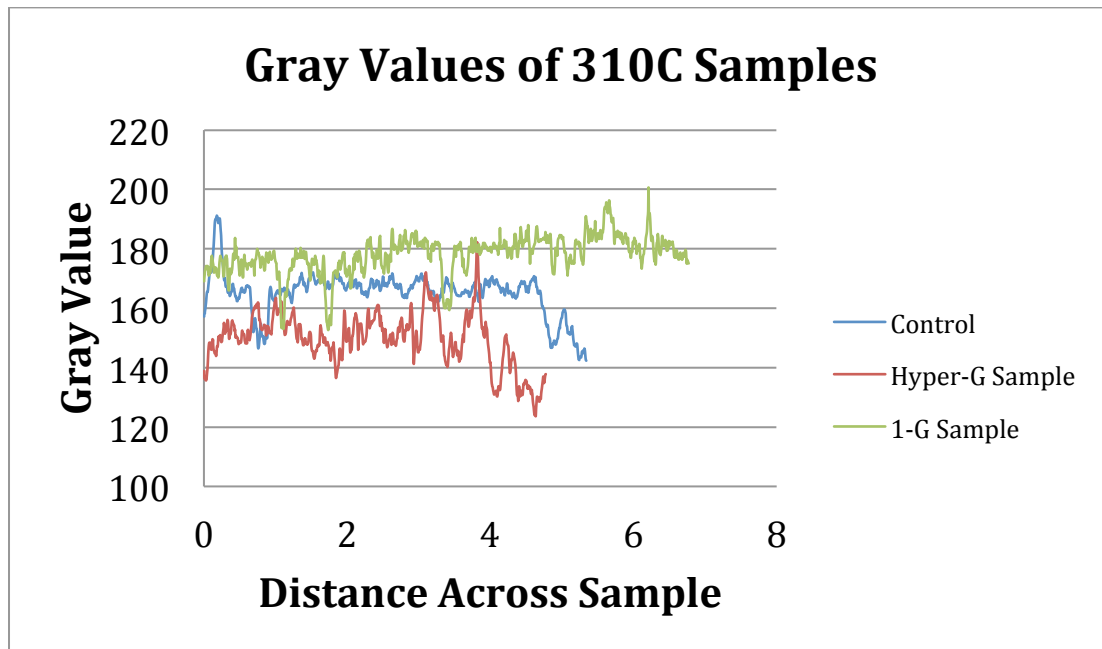
Figure 4.18: *Transmission plot of hyper-g ZBLAN sample and 1-g ZLBAN sample at*

310°C.

Figure 4.18 shows evidence that the hyper-g sample has crystallized at a slightly lower

temperature than the crystallization temperature (360°C) by having a lower gray value

(150) than the 1-g sample (160). Although, the hyper-g vs. 1-g evidence isn't as strong as

the μ-g vs. 1-g it is important to point out the effect hyper-g has on the ZBLAN samples.

Due to the variability of the hyper-g magnitude (1-g – 1.8-g) during the flight, each

hyper-g sample can yield varied results. The hyper-g samples discussed in this section

represent the overall effect that hyper-g has on a ZBLAN sample.

In addition to the 100X magnification microscopy, 400X magnification was also

completed. The same constant light intensity and phase contrast specifications were

implemented. The additional magnification was completed in order to identify smaller

crystallinity not apparent in the 100x magnification. Figure 4.19 shows the control

sample without any heat processing.

Figure 4.19: *400X magnification ZBLAN control sample.*

The ZBLAN control sample micrograph at 400X magnification shows an abundance of ~1-5 μm crystallites. This evidence shows that the initial synthesis processes completed in unit gravity induces very fine crystal growth. At this level of magnification the 'gray value' plots were not required due to the easily distinguishable variability apparent from the micrographs. Figure 4.20 shows the ZBLAN sample processed at 360°C in 0-g (top) and 1-g (bottom).
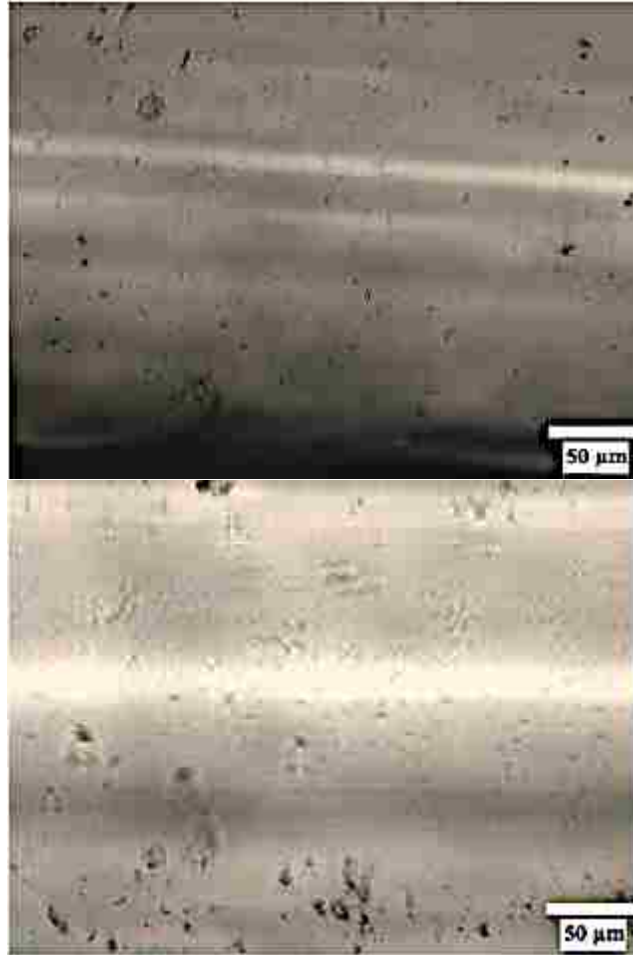
Figure 4.20: *400X magnification of ZBLAN processed at 360°C in 0-g (top) and 1-g (bottom).*

Figure 4.20 0-g (top) shows very similar crystal size to that of the control sample at this magnification (Figure 4.19). The crystal size is still on the order of approximately 1-5 μm. Whereas the 360°C sample at 1-g (bottom) has a slightly larger crystal formation and is more distributed. The approximate crystal size in the 1-g sample at 360°C appears to be on the order of 5-10 μm. There also is evidence of a radiating wavy texture as described by Wilson *et al.* [Wilson, 1984]. Figure 4.21 shows the ZBLAN samples processed at 370°C in 0-g (top) and 1-g (bottom).
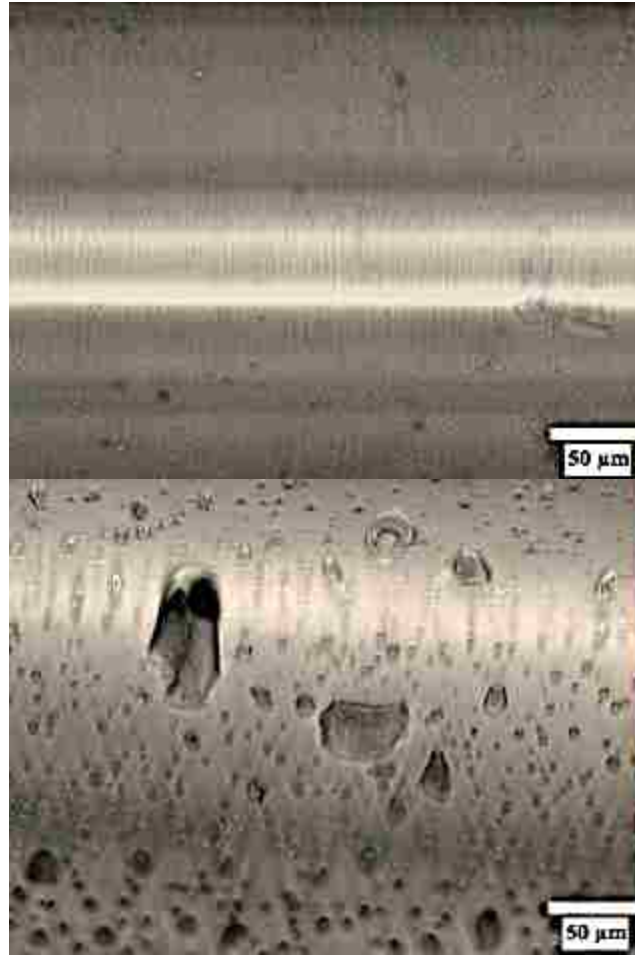
Figure 4.21: *400X magnification of ZBLAN processed at 370°C in 0-g (top) and 1-g*

(bottom).

The 370°C 0-g processed sample shows similar crystal evidence as the 360°C 0-g sample however a more radiating pattern has developed. The overall crystallite size has remained constant in the 0-g sample however the crystallite size in the 1-g sample has drastically increased. A few crystallites have grown to approximately 50 μm, whereas the majority of the crystals are on the order of 10-20 μm. Figure 4.22 shows the ZBLAN samples processed at 380°C in 0-g (top) and 1-g (bottom).
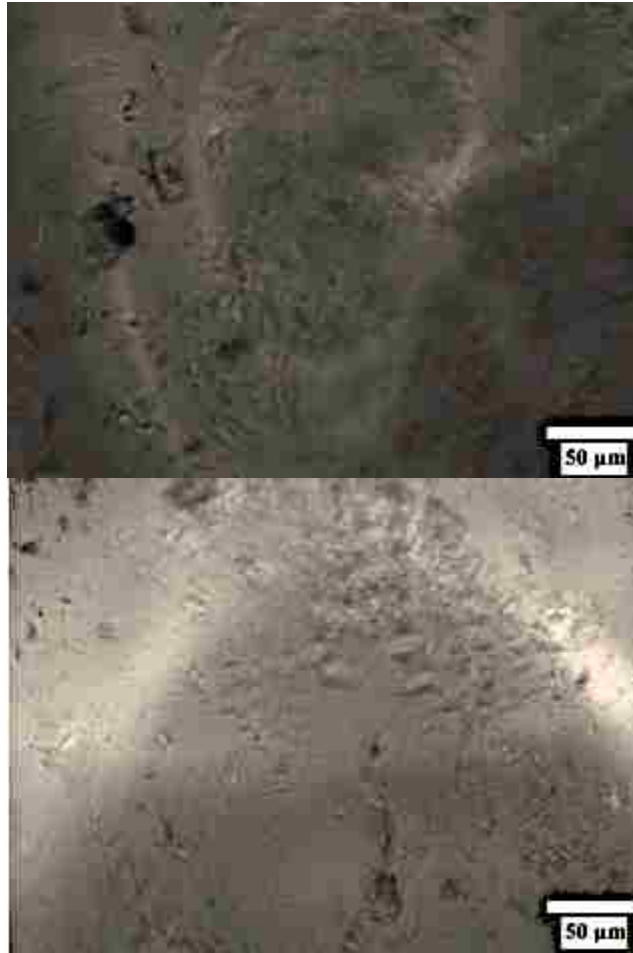
Figure 4.22: *400X magnification of ZBLAN processed at 380°C in 0-g (top) and 1-g*

(bottom).

Similar to the 100X magnification micrographs of the 380°C ZBLAN samples, the

crystallanity evidence is very similar between the 0-g and 1-g samples. The 400X

micrographs show similar crystallinity on the same size magnitude and the same patterns.

This is evidence that the mechanism governing crystal suppression in 0-g has little or no

effect at this temperature level. Figure 4.23 shows the ZBLAN samples processed at

410°C in 0-g (top) and 1-g (bottom).
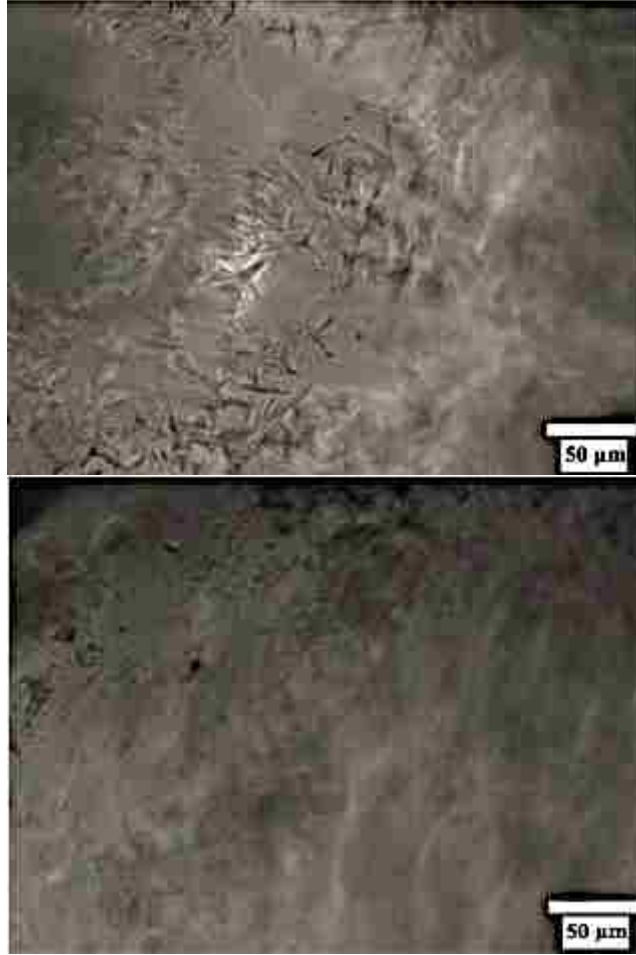
Figure 4.23: *400X magnification of ZBLAN processed at 410°C in 0-g (top) and 1-g (bottom).*

The ZBLAN samples processed at 410°C have both clearly crystallized. The shape of the crystallites in the 0-g (top) sample has differed from that of the crystallites shown in the previous micrographs. Similar radiating wavy texture is apparent in both 0-g and 1-g samples. Similar to the 380°C 0-g processed sample the mechanism governing crystal growth suppression has been overcome at this point in the temperature scheme.

Furthermore, 400X magnification micrographs were taken of the hyper-g processed ZBLAN samples. Figure 4.24 shows the ZBLAN samples processed at 290°C in hyper-g (top) and 1-g (bottom).
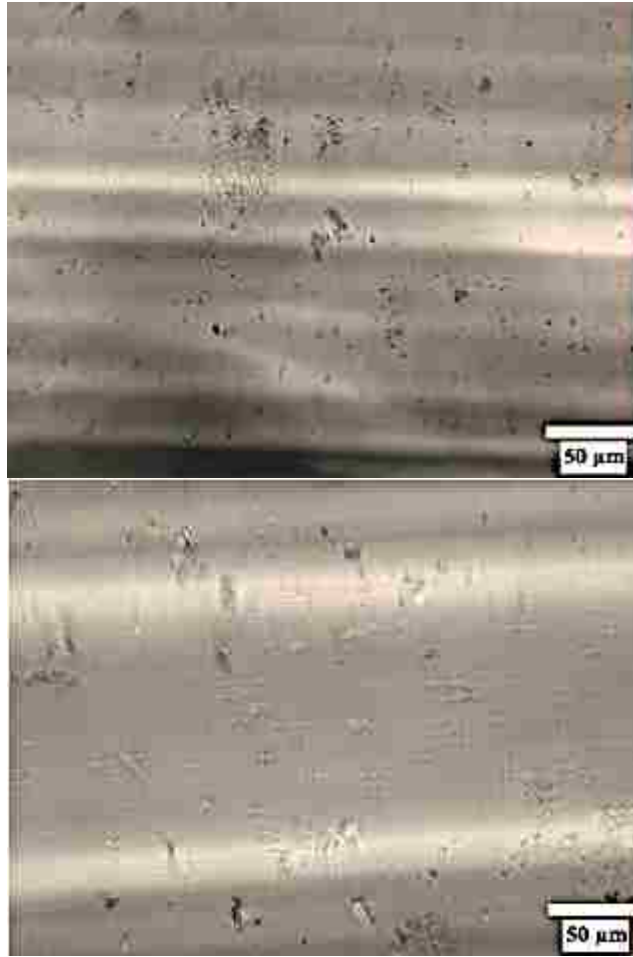
Figure 4.24: *400X magnification of ZBLAN processed at 290°C in hyper-g (top) and 1-g (bottom).*

The results obtained from the 290°C micrographs show crystallization on the order of 1-5 μm. The crystallites seem to be more abundant and arranged in small groups in the hyper-g (top) sample. The micrographs show evidence that crystallization has progressed beyond the initial crystals found in the control sample (Figure 4.19). These results are similar to that of the 100X magnification hyper-g micrographs, both suggest crystallization prior to the reported Tx of 360°C. Figure 4.25 shows the hyper-g samples processed at 310°C in hyper-g (top) and 1-g (bottom).
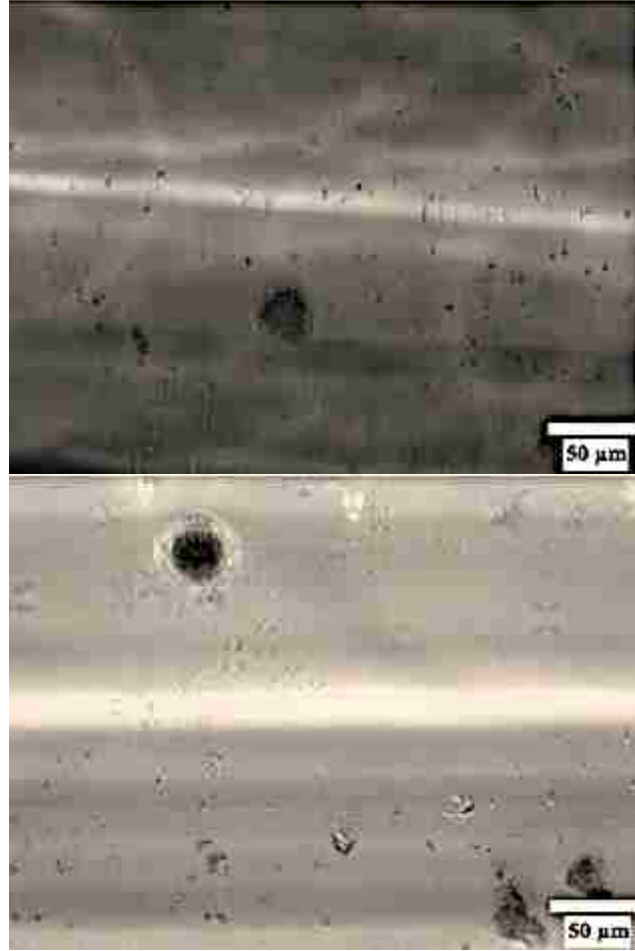
Figure 4.25: *400X magnification of ZBLAN processed at 310°C in hyper-g (top) and 1-g (bottom).*

Shown in the 310°C hyper-g and 1-g micrographs is a similar crystallinity growth. Small (1-5 μm) crystallites have appeared in abundance and some have clustered into 20 μm groups. Also noticed is that the hyper-g micrograph has the wavy texture similar to the micrographs above the crystallization temperature. Identical to that of Figure 4.24, the hyper-g micrographs show that crystallization has began prior to the reported crystallization temperature in 1-g.

4.2 Polarized Optical Microscopy

In addition to phase contrast microscopy, polarized optical microscopy was used to investigate the crystallinity of the ZBLAN samples. Polarized light microscopy exploits the optical properties of the material by revealing detailed information concerning the composition of the material, such as internal crystal growth. Therefore, polarized optical microscopy will provide additional detail beyond the phase contrast microscopy previously utilized. The microscope model used for this analysis is an Olympus BX50 set at 100X magnification. Figure 4.26 shows a micrograph of the control sample under polarized microscopy.
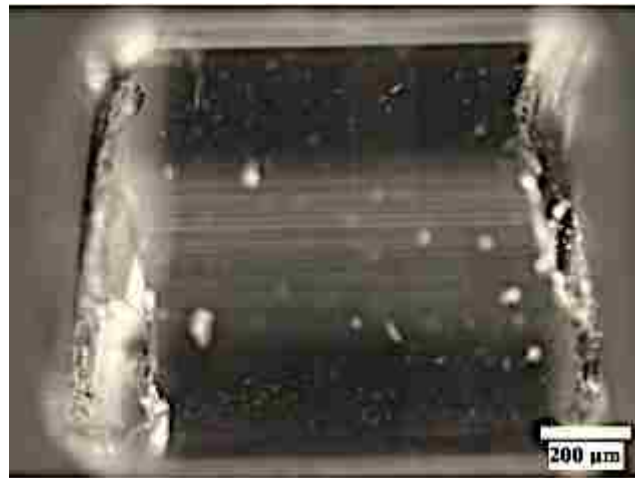
Figure 4.26: Polarized micrograph of ZBLAN control sample.

The polarized optical microscopy shows unique features not shown in the phase contrast microscopy. The first feature noticed is the few inclusions/crystals at an approximate size of 10-20 μms. There is also evidence of an abundance of very fine (1-5 μm) crystallites distributed throughout the sample. Figure 4.27 shows the samples processed at 360°C in 0-g (top) and 1-g (bottom).
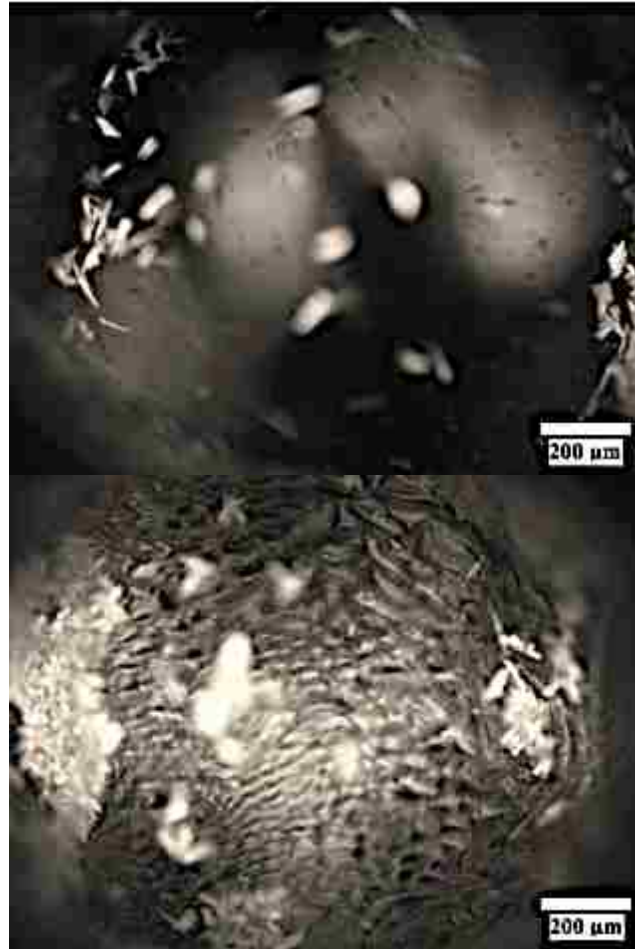
Figure 4.27: Polarized micrograph of ZBLAN sample processed at 360°C in 0-g (top) and 1-g (bottom).

Crystal growth is shown in both micrographs for the 360°C temperature set, however, the growth patterns are drastically different. The 0-g sample has a distributed acicular (slender and needle like) crystal pattern whereas the 1-g sample has the radiating wavy texture with mixed crystal structures on the order of 100 – 200 μm. Figure 4.28 shows ZBLAN samples heated to 370°C in 0-g (top) and 1-g (bottom).
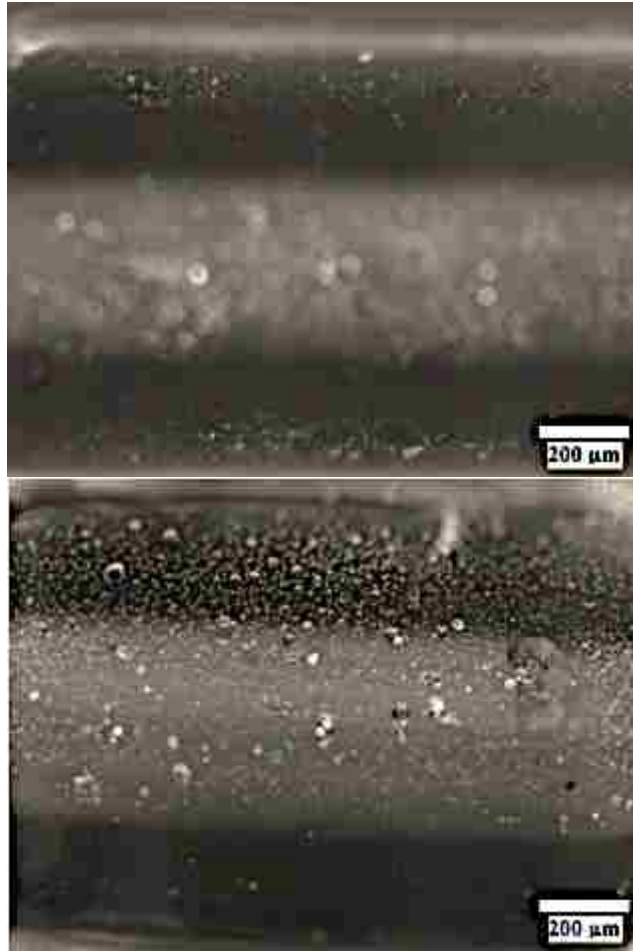
Figure 4.28: *Polarized micrograph of ZBLAN sample processed at 370°C in 0-g (top) and 1-g (bottom).*

The samples processed at 370°C show different results from that of the samples processed at 360°C. The crystal shape at the 370°C samples are more circular in shape as opposed to the acicular shape found in the 0-g 360°C sample. Both 370°C samples show a smattering of circular crystal formation on the order of 1-5 μm. However, the 1-g sample appears to have more crystallites than that of the 0-g sample. Figure 4.29 depicts the samples processed at 380°C in 0-g (top) and 1-g (bottom).
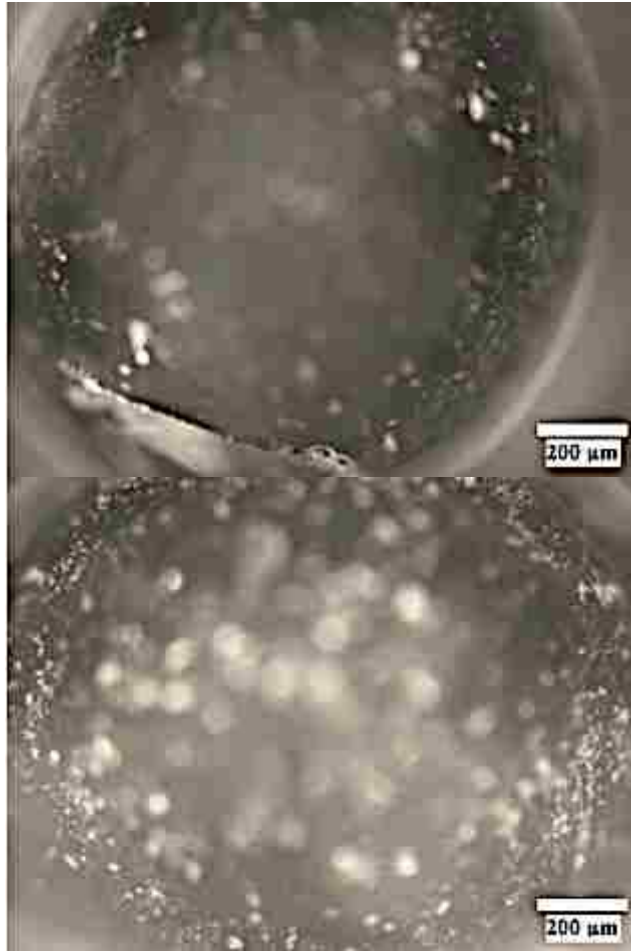
Figure 4.29: Polarized micrograph of ZBLAN sample processed at 380°C in 0-g (top) and 1-g (bottom).

A 10 degree progression in the temperature scheme shows that both samples have readily crystallized and lost their original shape. Both ZBLAN samples (Figure 4.29) have become spherical in shape and have crystal formation on the order of 1-10 μm. The results from the polarized microscope at this temperature are consistent with all of the previous microscopy results, both samples crystallize at 380°C. Figure 4.30 shows samples processed at higher a higher temperature (410°C) in 0-g (top) and 1-g (bottom).
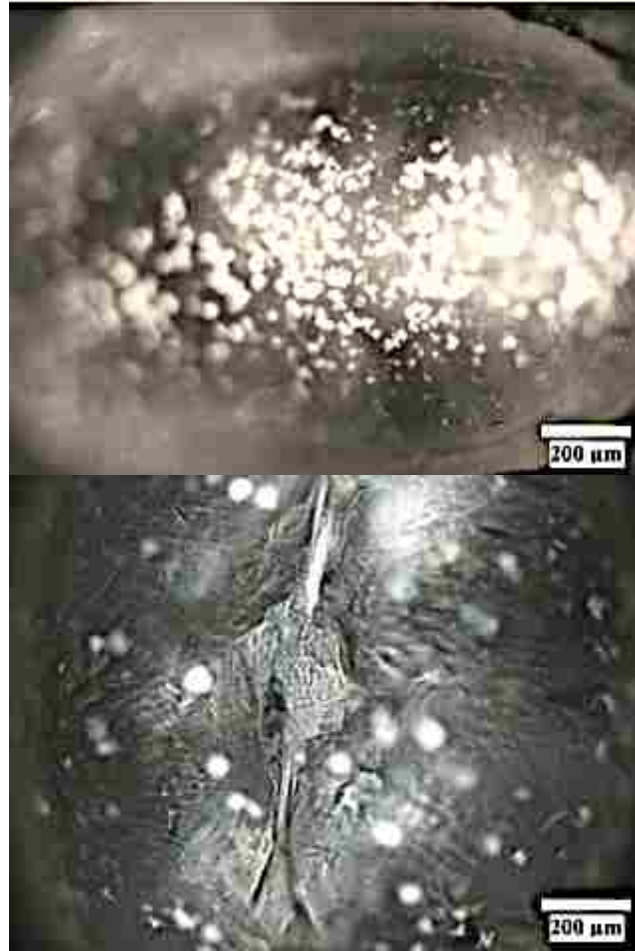
Figure 4.30: Polarized micrograph of ZBLAN sample processed at 410°C in 0-g (top) and 1-g (bottom).

Further investigation in the temperature scheme shows that at higher temperatures both the 0-g samples and the 1-g samples readily crystallized. This evidence can be seen in Figure 4.30 where both samples have become polycrystalline. These results are consistent with results obtained by other microscopy techniques mentioned above.

Additionally, the hyper-g samples were processed with the polarized microscope. Figure 4.31 shows the ZBLAN samples processed at 290°C in hyper-g (top) and 1-g (bottom).

Figure 4.31: *Polarized micrograph of ZBLAN sample processed at 290°C in hyper-g*

(top) and 1-g (bottom).

Figure 4.31 show that the hyper-g sample has a slightly higher amount of crystallites than that of the 1-g sample; almost no difference is noticed between each sample. The crystal size is in the order of 1-5 μm for both samples. Also noticed is that the 1-g sample under polarized microscopy is very similar to that of the control sample. However, the hyper-g sample has more finely grained crystallites distributed throughout the sample. Figure 4.32 shows additional hyper-g samples processed at 310°C.
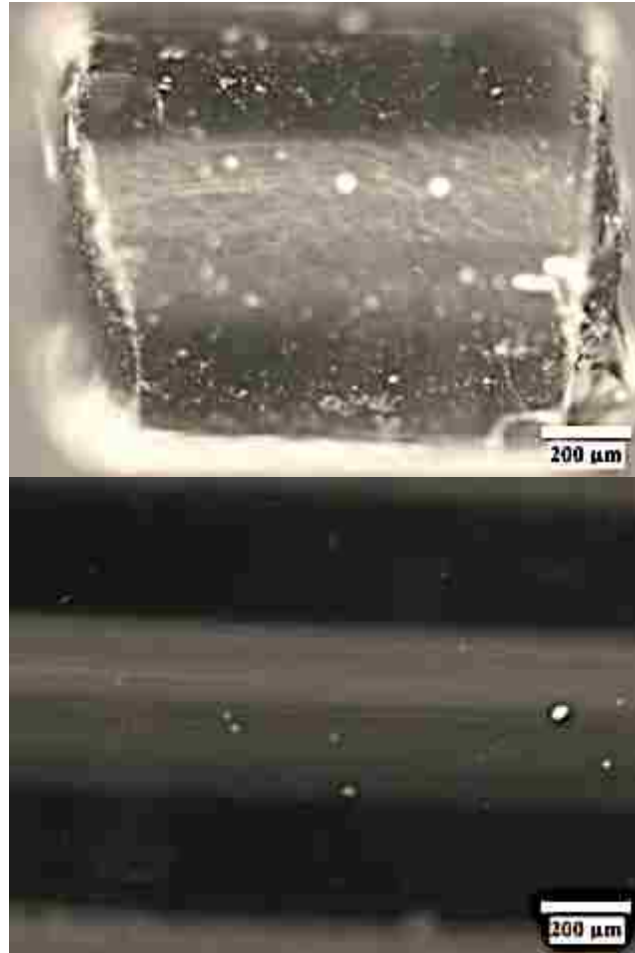
Figure 4.32: *Polarized micrograph of ZBLAN sample processed at 310°C in hyper-g*

(top) and 1-g (bottom).

The hyper-g sample processed at 310°C has readily crystallized with many crystallites on the order of 5 μm. Whereas the 1-g sample at the same temperature provides evidence that little or no crystallization has occurred at this point. These results are also similar to that of the previous microscopy techniques utilized. Samples processed in a hyper-g environment will crystallize earlier than the reported crystallization temperature.

4.3 Scanning Electron Microscopy

In addition to the optical microscopy, Scanning Electron Microscopy (SEM) micrographs of the ZBLAN samples were also taken. A SEM micrograph of the control specimen can be seen in Figure 4.33.
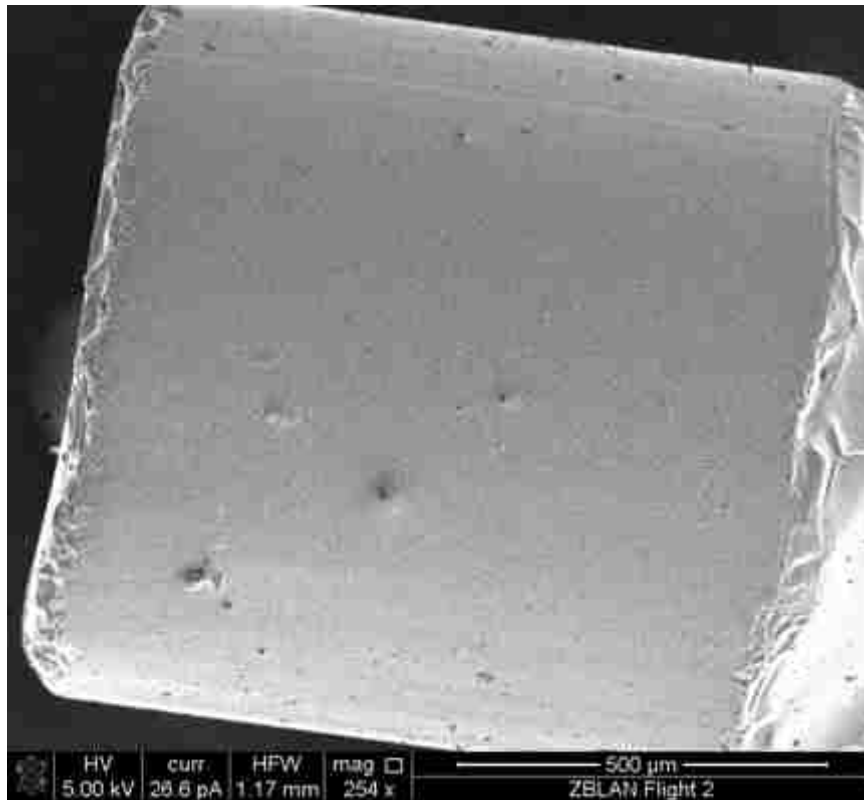
Figure 4.33: *SEM micrograph of ZBLAN control sample.*

A higher magnification of the control sample can be seen in Figure 4.34.
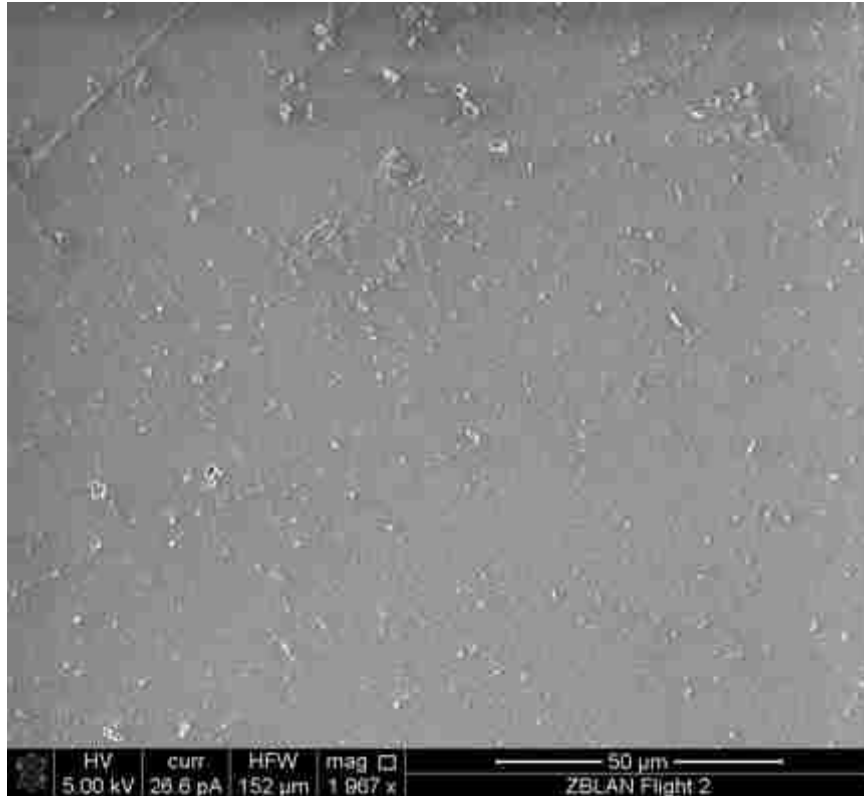
Figure 4.34: *High magnification SEM micrograph of ZBLAN sample.*

The evidence displayed in the high magnification SEM micrograph of the control sample

shows a smattering of very small (<1 μm) crystals apparent on the surface of the sample.

These very fine crystallites went unnoticed in the optical micrographs. Continuing along

the previous temperature progression, Figure 4.35 shows the ZBLAN samples in high

magnification processed at 360°C in 0-g (top) and 1-g (bottom).
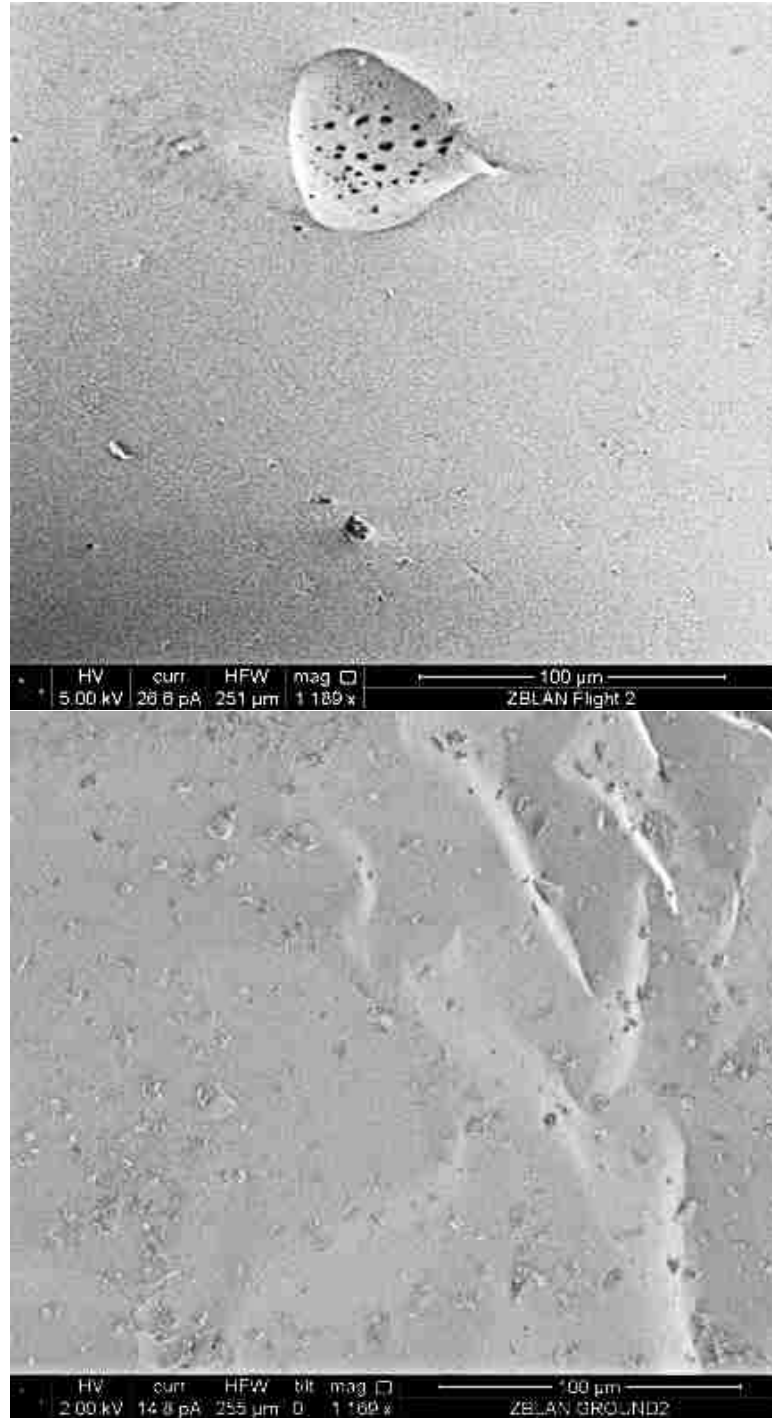
Figure 4.35: *SEM micrographs of ZBLAN processed at 360°C in 0-g (top) and 1-g*

(bottom).

The SEM micrographs at this magnification show very similar results as the previous

optical micrographs at both magnification levels. There is less crystallization in the 0-g

sample and a higher amount with a larger size of crystallization shown in the 1-g sample. Overall, very similar results are displayed with the SEM techniques as with the two previously discussed optical microscopy techniques. The minor difference noticed is the very fine crystal size shown at high magnification levels. Once the temperature set point approaches the crystallization temperature the crystal size demonstrated by both SEM and optical techniques is the same. Figure 4.36 shows the SEM micrographs for the ZBLAN samples at 410°C in 0-g (top) and 1-g (bottom).
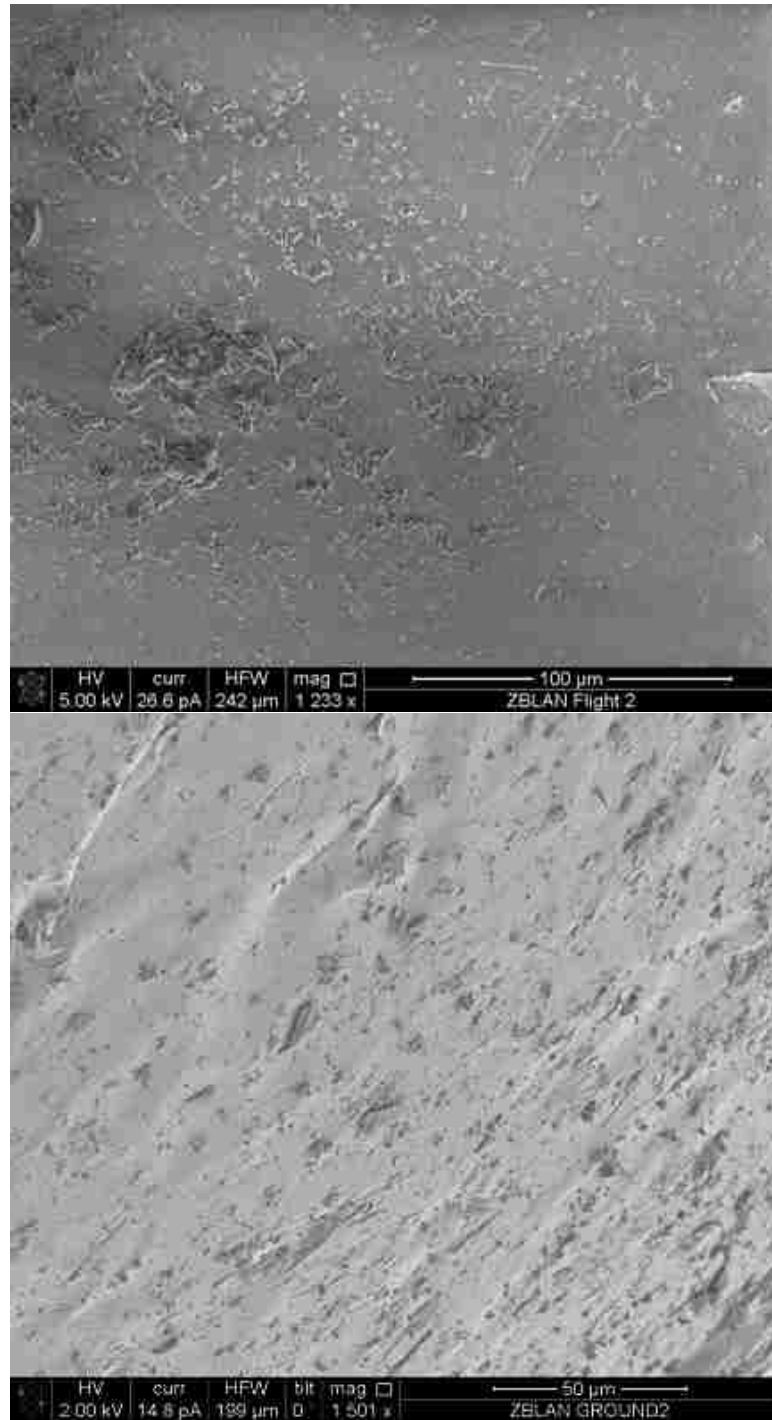
Figure 4.36: *SEM micrograph of ZBLAN processed at 410°C in 0-g (top) and 1-g*

(bottom).

The high temperature (410°C) SEM micrographs show a high amount of crystallinity in

both samples as expected based on the previous optical micrograph results. Both samples

have crystallization on the order of 5-10 μm and additional crystal growth on the order of 10-20 μm.

The major conclusion made from the optical micrographs and gray value plots is that crystallization occurs at 380°C in 0-g whereas crystallization occurs at 360°C in 1-g. Additional microscopic techniques (400X, polarized light microscopy) conclusions agree with the previous statement. The SEM micrographs didn't provide any major information beyond what the optical microscope techniques previously discussed. The additional information gained through SEM investigation is that the SEM micrographs show crystallization on the surface whereas it is difficult to determine the location of the crystallization displayed via optical techniques. The crystallization shown in the optical techniques could either be internal crystal growth or surface crystallization. The evidence of crystallization is all that is required to support the primary goal of this study. The SEM results did show very fine crystallization for the control samples that wasn't noticed under optical microscopy.

All of the results gathered from the microscopy investigation techniques mentioned above will assist with the following analysis and conclusions.

4.4 Rationale for Analysis of Flow and Mobility in micro-g and 1-g

In this section various reports on crystal formation in ZBLAN and other glasses have been critically reviewed to determine the mechanisms by which crystals can initiate and grow. In the context of this research of particular interest are phenomena that have the potential of being impacted by gravity or lack thereof (0-g). The analytical modeling of convective flow (influenced by gravity) as well as migration of particles that are gravity induced (sedimentation) vs. independent of gravity (diffusion) are presented in

118

the next section. Cranmer et al. (1990) have shown that most optical materials including ZBLAN are susceptible to moisture-induced degradation and crack growth, which can also be correlated to lower strength. The authors state that, "crack growth rate is controlled by either transport of the water molecule or hydroxyl radical (OH) or the reaction rate of these species with the highly strained bonds of the solid at the crack tip". They also point out that, "Because it is the chemical activity of the water, i.e. its partial pressure relative to saturation in a given environment, rather than its absolute concentration that is the key variable, completely inert environments are difficult to achieve". Ionic bonds of various forms in ZBLAN react with the water molecule, which is capable of donating either an electron or a proton to initiate the reaction. Ruihua et al. [1990], have reported ZrO_2 crystallites in ZBLAN using Raman spectroscopy. In addition to using a transmitted light polarizing optical microscope (also used in our research) these authors used SEM with carbon coating of polished surfaces and observed microcrystals in the size range of 2-8μm. Crystallites observed in preforms were of a much larger size 20-40μm. It was reported in this paper that LaF_3, which is used as a modifier in ZBLAN, also crystallizes out due to inhomogeneous mixing and locally enriched regions. The ionic nature of ZBLAN (vs. covalent bonds in Silica glass) makes it more susceptible to chemical degradation. LaF_3 crystals also cause almost two orders of magnitude higher attenuation due to a greater mismatch in refractive index, as compared to ZrF_4 and BaF_2 crystals.

Although less susceptible because of its covalent nature, Silica glasses also experience moisture-induced degradation, particularly at the surface where physically adsorbed water can eventually break down the structural bonds and alter the chemistry

119

[Leed and Pantano, 2003]. Due to their inherent lack of order glasses have a wide range of surface adsorption sites, which can be simulated with molecular dynamics tools to determine the distribution of active sites (Figure 4.37).
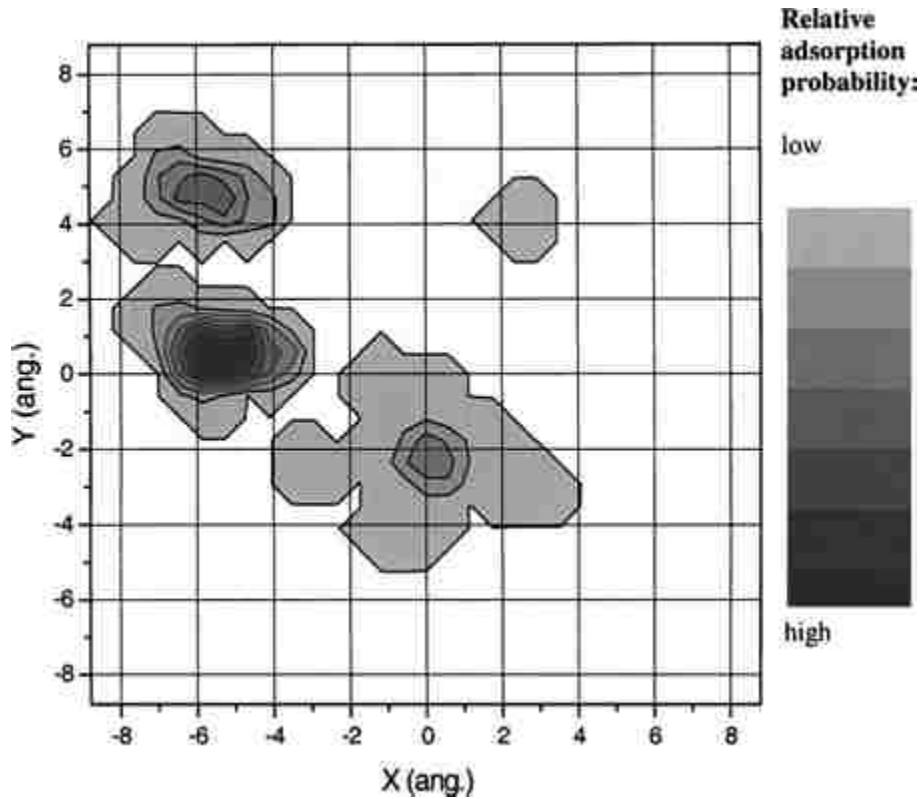
Figure 4.37: *Relative probability of water molecule attaching to regions of the surface*

[Leed and Pantano, 2003]

An example of an active site in Silica glass is a 3-coordinated Si; (SiO_3-; Non-bridging Oxygen), where hydroxylation (attachment of OH) occurs creating a Silanol group (Si-OH). Analogous to water where surface tension is caused by polarized water molecules, increasing the temperature beyond T_g in glass leads to increased availability of active sites. It is important in Figure 4.37 to note that the separation distance between an active and an inactive site is on the order of a few angstroms. This lends credibility to the

120

premise that even a small movement of reactive atoms/molecules could help promote reaction.

Poggemann et al. (2003) investigated the structure of Fluoride glasses using Atomic Force Microscopy (AFM) (Figure 4.38).
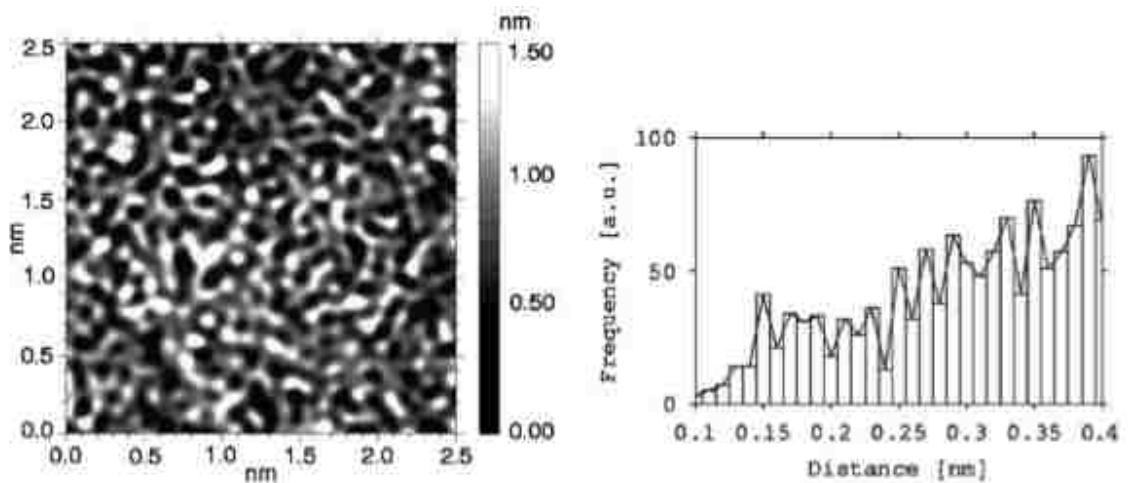
Figure 4.38: *Non-contact image of an ZrF_4-BaF_2-LaF_3 glass fracture surface and distribution of atomic distances [Poggemann et al., 2003].*

Their study indicated that Fluoride glasses have a dense structure with high connectivity. The authors state that "Special percolation paths seem to be not present. This is also reflected by the low Na diffusion coefficient".

According to a paper by Hehlen et al., [2008], extensive modeling of the cooling efficiency in ZBLAN:Yb3+ has shown transition-metal ions as well as water and hydroxyl (OH) ions to be the most problematic impurities and has estimated ~10–100 ppb to be the maximum impurity concentration for optical cryocoolers to be practical at 100–150°K. Neither individual fluoride compounds nor finished ZBLAN glass with the desired purity are commercially available. In fact, impurity levels in commercial fluorides are at least ~1000 times higher and unsuited for the preparation of laser-cooling

121

materials. This also explains the wide range of laser-cooling performance that has been observed in the past on nominally identical commercial ZBLAN:Yb3+ samples, the variations likely being the result of uncontrolled contaminations. Airborne mineral particles are a significant potential source of contamination by metal ions during open batch processing. Mineral dust particles consist primarily of silicon, aluminum, and iron compounds. African dust, for example, contains ~9 wt% of iron in the form of iron oxide (hematite, goethite) and clays (Illite, Kaolinite, Smectite). In the northern hemisphere, the mass concentration of dust particles on continents ranges from 10–1000 $\mu g/m^3$ of air and can vary significantly with location and season. Aerosol dust particles range in diameter from 1 nm to tens of μm.

This review of existing literature on the reactivity of glasses including ZBLAN lends credibility to the following:

- Reactions can be initiated by either internal or external contamination leading to crystallization.

- Greater variation of surface energy as well as greater exposure of such sites to contaminants leads to a propensity for crystallization at the surface.

- With regards to moisture induced crystal formation, the source of moisture could be residual moisture or adsorbed moisture in the glass. Other materials promoting crystallization can be internal (La) or external (microscopic mineral dust).

- Inherent (internal) impurities are immobile at normal temperature and are mobilized upon heating, particularly as the glass softens at temperatures above its T_g.

Therefore the rate of crystallization will be a function of how often materials capable of nucleating or growing a crystal arrives at an active site. This indicates that the mobility (flow and velocity) of the material system plays an important role in determining the rate of crystallization.

4.5 Analysis of Mobility in ZBLAN

The analyses conducted as part of the present research investigated the processes of heat and mass transfer that affect mobility in a fluid. The two primary processes to consider are mobility (mass transfer) due to buoyancy driven convection and mobility through diffusion. Conduction is a contributor of heat transfer, which indirectly affects the other two mass transfer mechanisms and hence it is included in the investigation. The process of diffusion is unaffected by the magnitude of the gravity acceleration whereas buoyancy driven convection is directly proportional to gravity. Evidence obtained from optical microscopy suggests that the ZBLAN samples processed in microgravity crystallized at a temperature (~380°C) above the recorded crystallization temperature. This evidence suggests that the lack of mobility due to convection in the microgravity environment affects the crystallization of the ZBLAN samples such that crystal growth is suppressed. Therefore, the ZBLAN sample crystallized at 360°C in 1-g sample should be of comparable magnitude to the crystallization in a 380°C μ-g sample. The contribution of each mobility term can be described symbolically in Eq. 4.1 shown below.

$$\Delta_{D360°C} + \Delta_{C1-g} \approx \Delta_{D380°C} + \Delta_{Cμ-g}$$

Where the Δ represents the contribution from the respective mobility term. The D in the subscript represents the contribution from diffusion at the specified temperature. The

subscript *C* represents the mobility contribution from the convection term at the specified gravity level (1-g, and micro(μ)-g). The temperatures (360°C and 380°C) were selected based on crystallization evidence from the optical and gray value transmission plots as discussed in previous sections. This novel equation captures the mobility due to diffusion and convection at relevant drawing temperatures.

4.6 Diffusion Analysis

Boutarfaia et al. (2001) studied the crystallization kinetics in fluoride glasses other than ZBLAN. Composition adjustments were implemented in a multicomponent glass based on the fluorides of In, Ga, Y, Zn, Sr, Ba and Na and physical properties of the resulting glasses were measured. The apparent activation energy for crystallization, E, was reported to be in the range of 190 to 210 kJ/mol. Since the activation energy for ZBLAN was not available, the variation of diffusion for different diffusing molecular species was determined using the Einstein equation. In order to compare the results thus obtained, the equivalent activation energy was derived using the diffusion vs. temperature data from the Einstein equation with that from the more conventional diffusion equation, Eq. 4.2.

$$D = D_0 \, e^{-E/RT}$$

Where *E* is the activation energy, *R* is the universal gas constant and T is the absolute Temperature. Using this equation and the values of *D* at different temperatures, the activation energy for ZBLAN was calculated to be 340 KJ/mol at the temperature range 650-660°K where crystallization occurred in a micro-gravity environment.

These authors state, "When the E value is small, devitrification tendency is reduced, while less stable glasses often exhibit very large values. This may appear paradoxical insofar as one would expect this activation energy to represent the energy barrier between metastable vitreous state and crystal. In fact, the physical meaning of E is still to be explained."

This paper also points out that fiber drawing is difficult for materials with an Avrami exponent greater than 3, and Fluoride glasses have Avrami exponents in excess of 4. The value of the Avrami exponent n is larger than 4, corresponding to an increasing nucleation rate with time. The Avrami # 'n' relates the volume fraction of materials crystallized 'x' to the time 't' during which crystallization is allowed to occur according to Eq. 4.3:

$$x = 1 - e^{-kt^n}$$ ■■■

Overall, diffusion is a transport phenomenon that occurs throughout nature. A fundamental definition of diffusion is described as the intermingling of molecules in solids, liquids and gases due to spontaneous motion of individual molecules. Diffusion as a function of time and distance, which are both of interest in our analyses, governed by Fick's first and second law shown in Eq. 4.4 and 4.5 respectively.

$$J = -D \frac{\partial \phi}{\partial x}$$ ■■■

$$\frac{\partial \phi}{\partial t} = D \frac{\partial^2 \phi}{\partial x^2}$$ ■■■

Where J is the diffusion flux, D is the coefficient of diffusion, ϕ is the concentration (amount of substance per volume), and t is time.

The diffusion constant can be calculated based on the Stokes-Einstein equation given below in Eq. 4.6.

$$D = \frac{kT}{6\pi\eta R}$$

Where D is the diffusion constant, k is Boltzmann's constant, T is the specified temperature, R is the radius of the diffusion molecule, and η is the viscosity. The viscosity equation as a function of temperature for ZBLAN was formulated using the viscosity graph described by Dunkley *et al.* [Dunkley, 2004] shown in Figure 4.39.
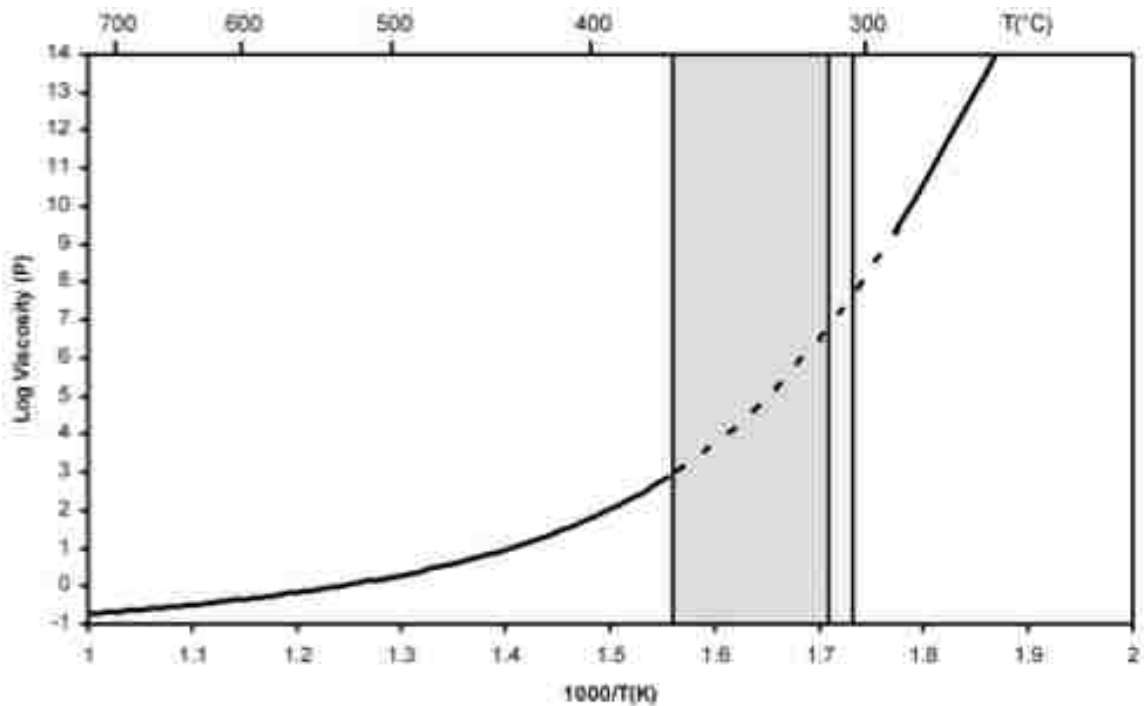
Figure 4.39: *Viscosity of ZBLAN versus temperature [Dunkley, 2004].*

The viscosity as a function of temperature equation for Figure 4.39 can be seen in Eq. 4.7.

$$\eta(T) = 10^{\frac{87,447}{T} - \frac{8.18E7}{T^2} + \frac{2.57E10}{T^3} - 31.721}$$

The units of Eq. 4.7 are in Poise (P). The COMSOL model calls for units of Pascal-second (Pa-s), therefore dividing Eq. 4.7 by 10 will provide the correct unit system (1Pa-s = 10P).

The Stokes-Einstein equation (Eq. 4.6) can be used to determine the diffusion coefficient of a molecule of radius, R, diffusing through ZBLAN. Each molecular constituent of ZBLAN including water and oxygen molecules were investigated as possible diffusing molecules. The water and oxygen molecules were investigated due to moisture and oxygen induced crystallization as described by Cranmer et al. [1990]. The list of molecules and their corresponding molecular radii are shown in Table 4.1.

Table 4.1: *List of investigated diffusion molecules.*

Molecule	Size (m)
ZrF_4	1.92E-10
BaF_2	1.95E-10
LaF_3	1.63E-10
AlF_3	1.14E-10
NaF	1.62E-10
H_2O	2.75E-10
O_2	1.21E-10
Average	1.74E-10

The average molecular radius was used for determining the diffusion coefficient of ZBLAN as a representation of the overall diffusivity of the material. The calculated diffusion coefficient in ZBLAN is represented in Figure 4.40.
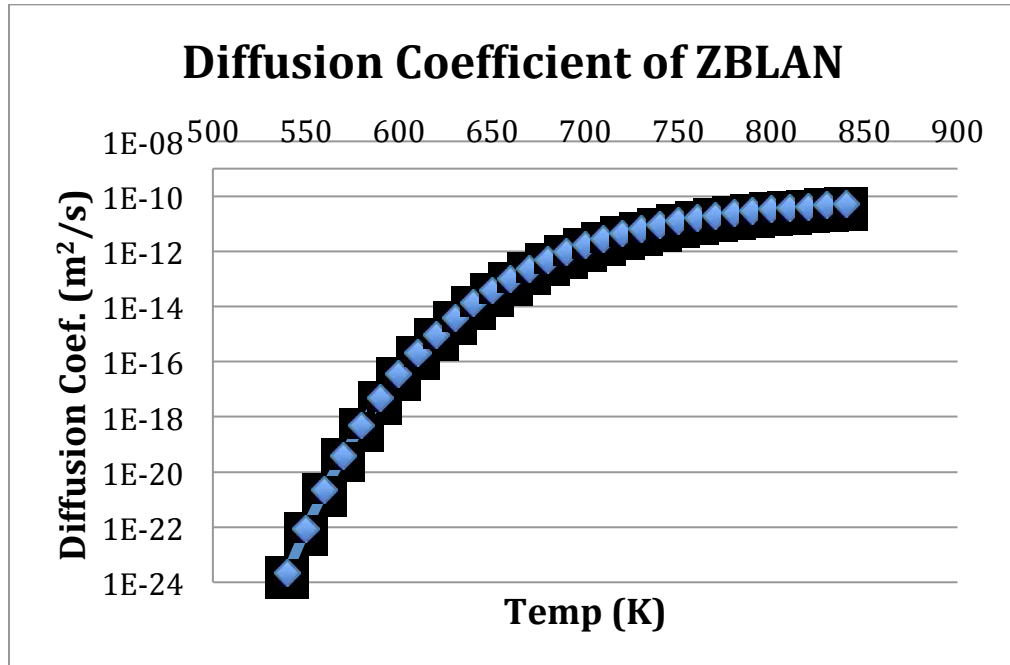
Figure 4.40: *The calculated diffusion coefficient of ZBLAN glass at varying*

temperatures.

As shown in Figure 4.40, the diffusion coefficient of ZBLAN glass increases
rapidly. The calculated diffusion coefficient at the relevant temperatures of 360°C and
380°C are 1.31E-14m^2/s and 1.01E-13m^2/s respectively. The diffusion calculations will
be further utilized in the upcoming sections.

4.7 Conduction Analysis

Before the final heat transfer model was developed a pure conduction model was
created and verified with an analytical model. A one dimensional conduction problem
was developed for a semi-infinite plate of ZBLAN (properties determined from a
literature survey). An analytical based model was developed for verification in which the
generalized equation for transient thermal conductivity is used, given by Eq. 4.8.

$$\frac{\partial^2 T}{\partial x^2} + \frac{\partial^2 T}{\partial y^2} + \frac{\partial^2 T}{\partial z^2} + \frac{1}{k}\frac{dq}{dt} = \frac{1}{\alpha}\frac{dT}{dt}$$ ⬛

Where T is temperature, k is the thermal conductivity, q is heat energy and α is the thermal diffusivity constant given by Eq. 4.9.

$$\alpha = \frac{k}{\rho C_p}$$ ⬛

Where ρ is the density and C_p is the specific heat. In order to investigate a one dimensional heat transfer, the solution pertaining to an infinite media can be described in Eq. 4.10.

$$\frac{T(x,t)-T_0}{T_\infty - T_0} = 1 - \text{erf}\left(\frac{x}{2\sqrt{\alpha t}}\right)$$ ⬛

Where T(x,t) provides the temperature at location x at time t, T_0 and T_∞ are initial and final (boundary) temperatures, erf is a function whose values can be determined from Figure 4.41.
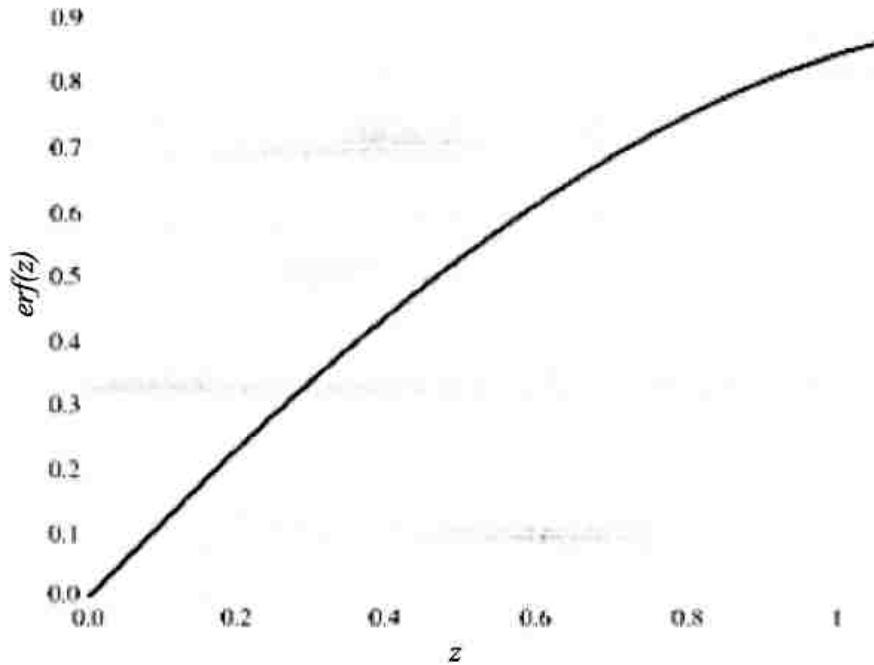
Figure 4.41: *Graph of the error function for Eq. 4.7 [Incropera and DeWitt, 2002].*

The above equations and graph were utlized to verify a pure conduction COMSOL model

in a semi-infinite plate. Figure 4.42 shows the COMSOL model results for a 1-

dimensional pure conduction model.
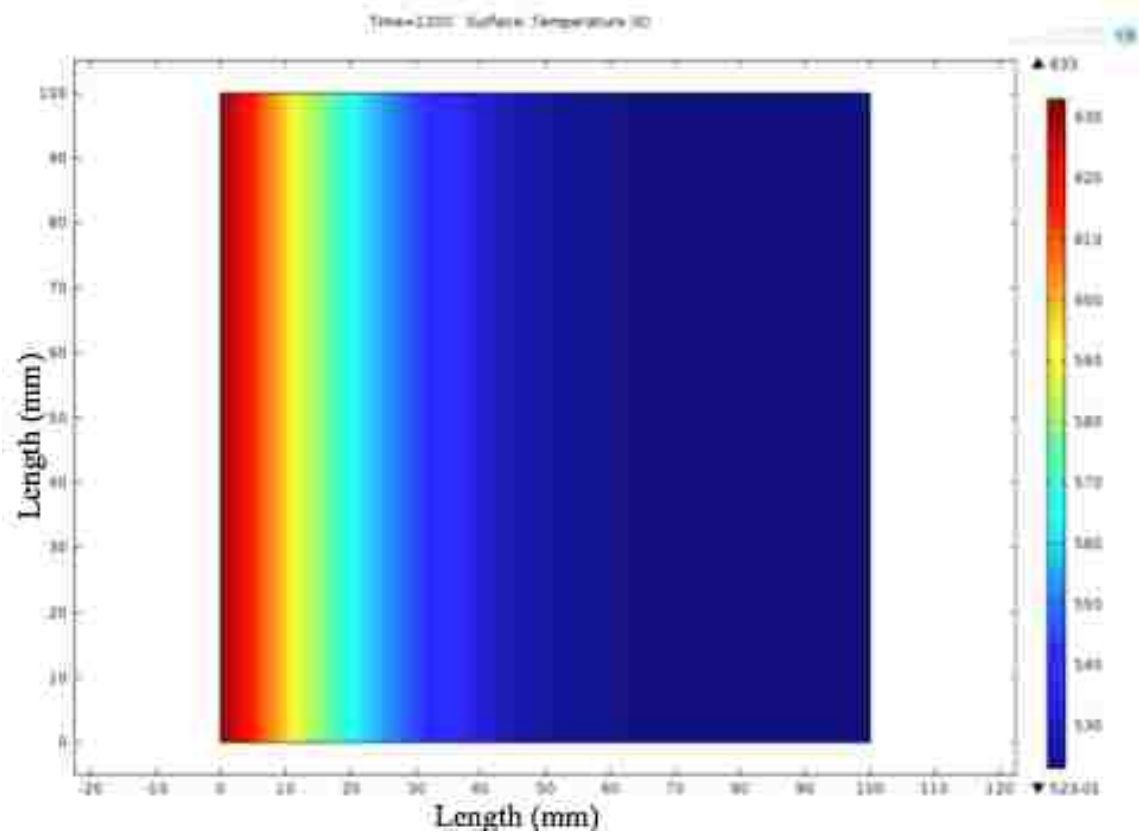
Figure 4.42: *Pure conduction problem for ZBLAN at 1200s (20min) [523K to 633K].*

The model results shown in Figure 4.42 are for a pure conduction problem in a semi-infinite ZBLAN sample heated from 523K (250°C) to 633K (360°C) from the left boundary for a duration of 20 minutes. The model yields results as expected for a pure conduction problem, heat is evenly conducting through the sample from the heat soure (left boundary). As previously described, the results were verified analytically by means of Eq's. 4.9-4.10. Table 4.2, below, shows the comparison of the two results when calculating the temperature at varying locations from the left boundary.

Table 4.2: COMSOL results versus calculated results for conduction.

Location From Left Boundary (mm)	COMSOL Temp (K)	Calculated Temp (K)
1	631	632
5	615	616
10	598	597
15	578	578
20	567	566
25	556	555

Table 4.2 shows that the two results are almost identical, which ultimately verifies the accuracy of COMSOL for analyzing pure conduction.

4.8 Convection Analysis

Convection is a heat transfer and mass transfer mechanism that governs movement of molecules within fluids. The governing equations for convection can be seen in Eq. 4.11 - 4.13.

$$\frac{\partial u}{\partial x} + \frac{\partial v}{\partial y} = 0$$

$$\rho = u\frac{\partial u}{\partial x} + v\frac{\partial u}{\partial y} = -\frac{\partial p}{\partial x} + \mu\frac{\partial^2 u}{\partial y^2} - \rho g$$

$$u\frac{\partial T}{\partial x} + v\frac{\partial T}{\partial y} = \alpha\frac{\partial^2 T}{\partial y^2}$$

Where ρ is the density of the fluid, p is the pressure, μ is the viscosity of the fluid, g is the gravitational term, T is temperature and α is the thermal diffusivity constant. Additionally, the x-direction in this analysis refers to the horizontal length of the sample

(2-3mm) direction and the y-direction is along the width (diameter, 1mm) of the sample and is in the direction of gravity.

Convection can be seperated by the different types of convection specific to the situation. The specific convection mechanism present in this study is known as natural or free convection. Natural convection in a heated ZBLAN sample was then investigated. Natural convection is a heat transport mechanism in which the fluid motion is generated purely by density differenes in the fluid due to temperature gradients. Natural convection will occur when the fluid near a heat source becomes hotter and less dense (relative to surrounding fluid) and rises. The surrounding cooler and more dense fluid falls and replaces the previous fluid. This cooler fluid is now closer to the heat source, which then becomes hotter, rises, and the process is continued. This continued process then creates what is known as a convection current; this progression transfers fluid from one location to another. The overall driving force for natural convection to occur is bouyancy, which results from a difference in fluid density. Therefore, bouyancy requires inertial forces such as gravity to drive natural convection. Thus, natural convection lacks it's driving force in a state of microgravity. The onset of natural convection is determined by the Rayleigh Number (Ra), a dimenstionless number shown in Eq. 4.14.

$$\mathbf{Ra} = \frac{\Delta \rho g L^3}{D \mu}$$

Where $\Delta \rho$ is the difference in density between the two convecting fluids, g is the local gravitational acceleration, L is the characteristic length-scale of convection, D is the diffusivity, and μ is the dynamic viscosity. A relationship for the density of ZBLAN was required to accurately determine the Rayleigh Number as well as build a heat transfer

model in COMSOL. The density as a function of temperature for ZBLAN was formulated analytically by using the documented density at room temperature (ρ = 4.33g/cm^3) and the documented coefficient of thermal expansion (α = 17.6E-6/°C) [Harrington, 2007]. Utilizing the coefficient of thermal expansion, the calculation must take into account expansion of volume, represented in Eq. 4.15.

$$\frac{dV}{dT} = 3\frac{dL}{dT}$$ ⬛

The resulting function of density of ZBLAN with respect to temperature can be seen in Eq. 4.16.

$$\rho(T) = 4334.1 - 0.2175T$$ ⬛

The units of Eq. 4.16 are in kg/m^3, which are the appropriate units required by COMSOL. According to the Rayleigh Number, when the density variation in the fluid is high, natural convection will be more rapid. Also the same conclusion can be made for the gravity term, g, when g is large so will natural convection. Conversly, reducing g to zero completely halts natural convection, thus removing convection as a transport mechanism. Also, convection will be less likely at a higher viscosity and less relevant compared to the diffusivity rate. Overall, the Rayleigh number shows how the onset of natural convection is proportional to the gravity term and is shown in Table 4.3.

Table 4.3: Rayleigh number calculations for ZBLAN in 1-g compared to μ-g.

Ra No. (1-g)	
360°C	380°C
5.68E+04	6.51E+04
Ra No. (μ-g)	
5.68E-02	6.51E-02

The Rayleigh number calculations presented in Table 4.3 represent a ZBLAN sample heated from 250°C to the respective temperatures 360°C and 380°C. The numbers provide additional evidence that relates the Rayleigh number to the gravity term, thus formulating natural convection to be directly proportional to gravity.

In order to verify that COMSOL multi-physics was modeling natural convection correctly, the full ZBLAN model was manipulated from a COMSOL provided convection verification model. The verification model shows the natural convection currents for a warming water glass. The model provided by COMSOL has been verified, therefore, the water glass model was minupulated so the dimensions and properties align with that of the ZBLAN model. Figure 4.43 shows the results obtained when running the warming water glass model.
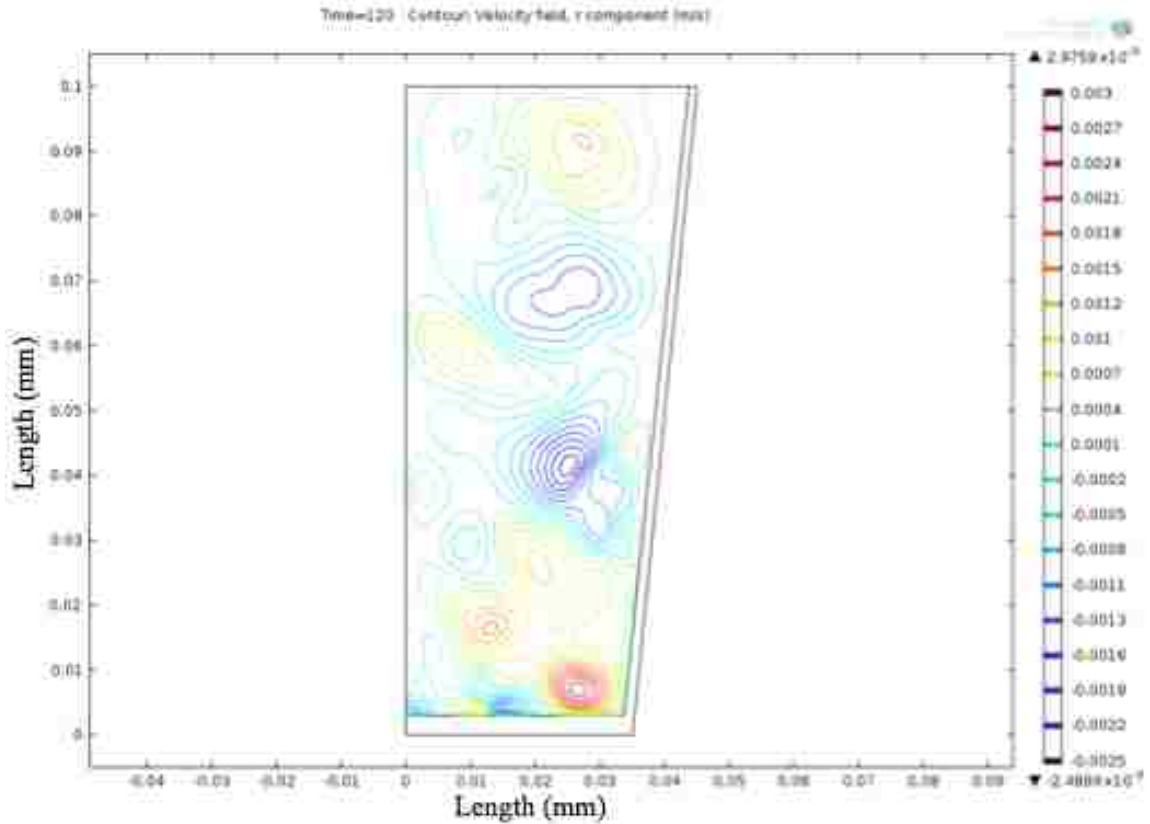
Figure 4.43: COMSOL velocity contour results for a glass of water cooling from 5°C to 22°C.

Once the provided COMSOL model was manipulated to the specific dimensions and properties of the ZBLAN model, the model could provide natural convection velocity currents as well as temperature gradients at specific times. Each step of the COMSOL model verification can be found in Appendix A. A ZBLAN specific model was developed with exact dimensions and properties relating to the experimental program discussed in Chapter 3. The output from the COMSOL model provides a temperature gradient and velocity contour at specific time intervals for the desired temperature. Figure 4.44 shows a temperature gradient and velocity field for a ZBLAN sample heated from 250°C to 360°C at a time step of one second.
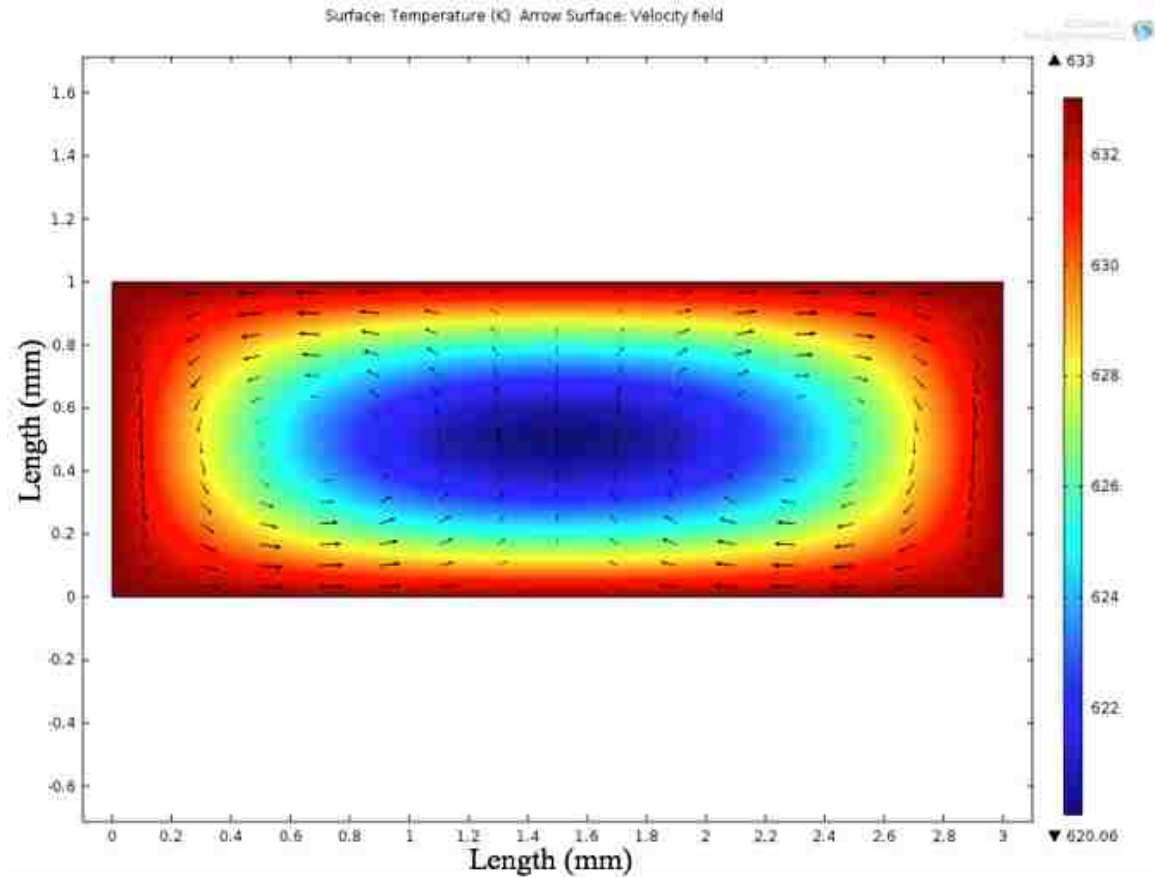
Figure 4.44: *ZBLAN sample heated from 523K to 633K at 1s.*

At a time of 1 second the ZBLAN sample is rapidly heating, as evidenced by the thermal

gradient represented in Figure 4.44. A velocity field was added to the plot to show the

movement of the fluid due to the temperature variations. Figure 4.45 shows the thermal

gradient of the same ZBLAN sample at 0.5s (note the larger temperature range on the

scale to the right of figure).
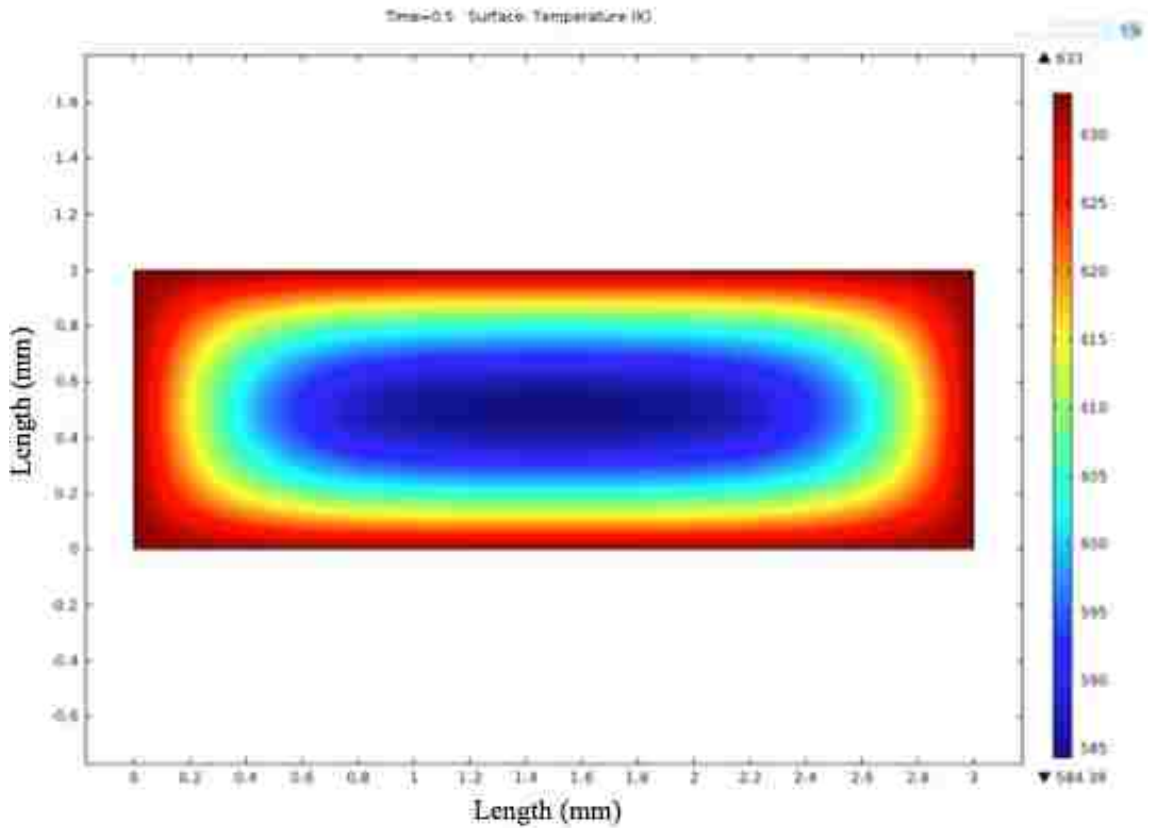
Figure 4.45: ZBLAN sample heated from 523K to 633K at 0.5s.

As shown in Figure 4.42, the ZBLAN temperature gradient only varies by approximately 50 degrees at 0.5s compared to a 10 degree variation at 1s (Figure 4.44). Figure 4.46 shows the ZBLAN sample at three seconds, the entire sample is now close to 633°K.
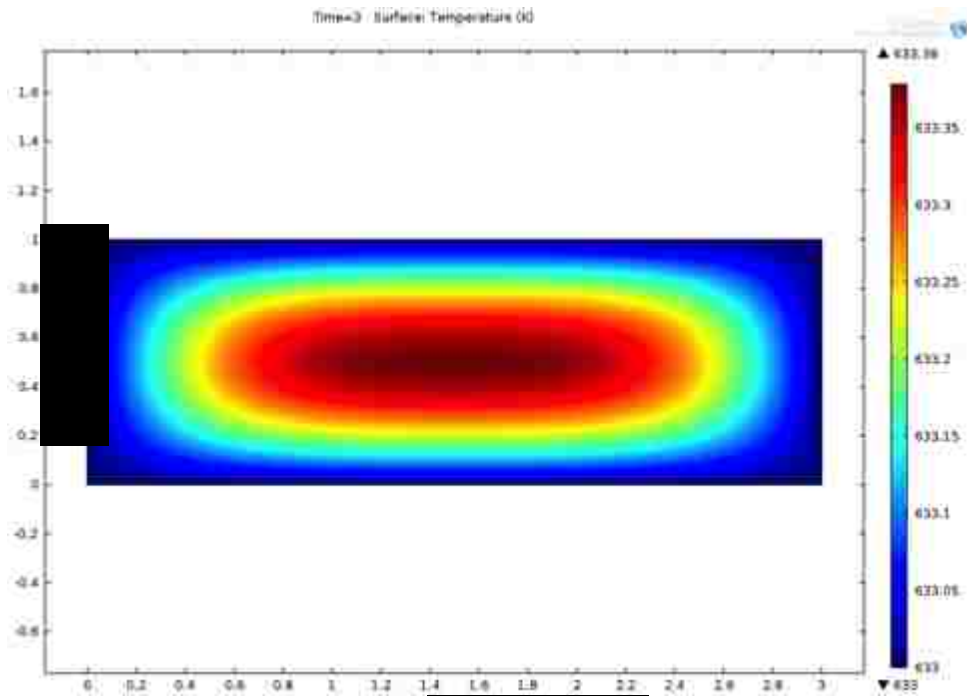
Figure 4.46: *ZBLAN sample heated from 523K to 633K at 3s.*

As shown in Figure 4.46 the sample has reached a steady state temperature. Figure 4.46

shows a small temperature variation of 0.38 degrees. This variation is insignificant to the

overall scope of the experiment. The overall conclusion gleaned from the temperature

gradient analysis is that the ZBLAN sample in the experiment reaches the set temperature

within a period of approximately 3 seconds; well within the time-frame of our

experiments.

In addition to the temperature gradient plots, velocity contour graphs are also

plotted. A graphical representation of one of the velocity contour results for the ZBLAN

sample model can be seen in Figure 4.47.
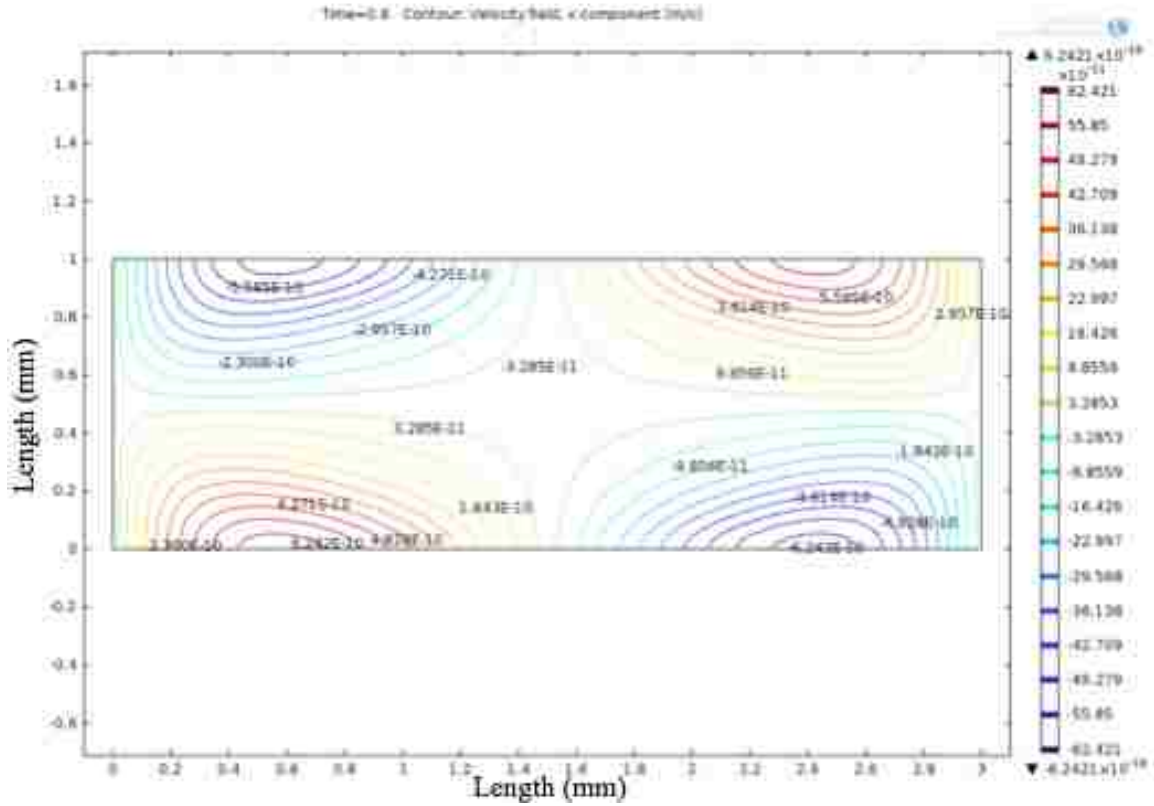
Figure 4.47: *Velocity contour plot for ZBLAN heated from 523K to 633K at 0.8s [unit-gravity].*

The velocity contour shown in Figure 4.47 represents the convection current for the fastest time step from 0-20 seconds (the duration of microgravity).

A graphical representation of the convection analysis can be seen in the Figures below. Figure 4.48 shows the velocity across the ZBLAN sample at varying time steps. Figure 4.49 isolates the outer edge of the sample and shows the velocity versus time.
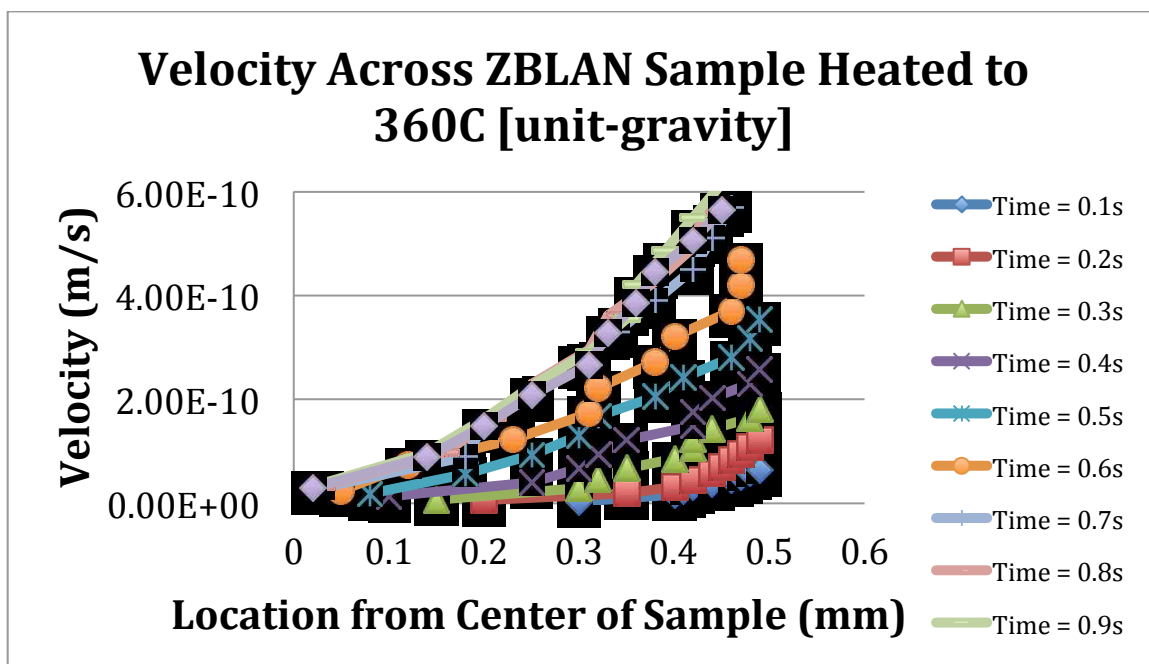
Figure 4.48: *Velocity across the ZBLAN sample heated from 250°C to 360°C at varying*

times.
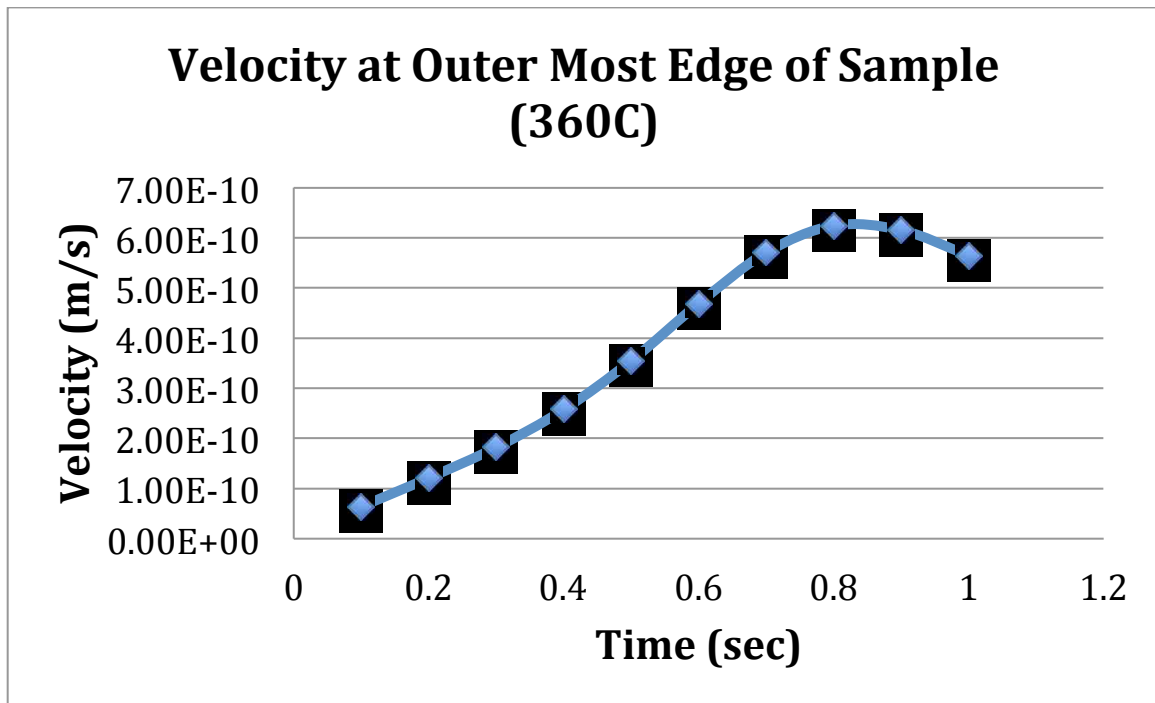
Figure 4.49: *Velocity at outer edge of the ZBLAN sample heated from 250°C to 360°C*

from 0 to 1 second.

Figure 4.50 is similar to Figure 4.49, however the time is plotted out to 12 seconds as

opposed to 1 second. Figure 4.50 plots the outer edge velocity in a ZBLAN sample

heated from 250°C to 360°C from the time period of 0.1 seconds to 12 seconds. The time

that the ZBLAN sample is heated and cooled in the microgravity duration is estimated to

be approximately 12 seconds. Some of the time is lost due to translating the sample in

and out of the furnace and the reaction time required to quench the sample. Figure 4.50

can be seen below.
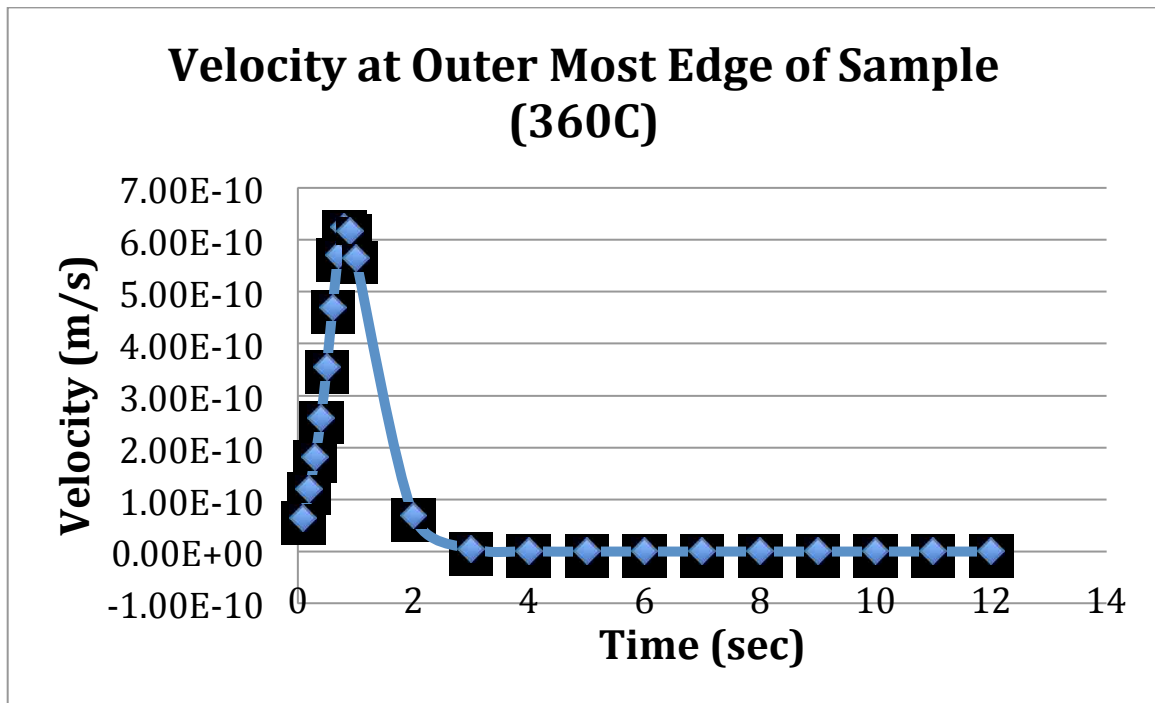
Figure 4.50: *Velocity at outer edge of ZBLAN sample heated from 250°C to 360°C from*

0.1 to 12 seconds.

As seen in Figure 4.50, the convection velocity at the outer edge of the sample increases

rapidly due to thermal shock, and then decreases down to a constant velocity due to

thermal equilibrium.

In addition to investigating the velocity at the outer edge of the sample, the

average velocity throughout the sample was plotted versus time, shown in Figure 4.51.
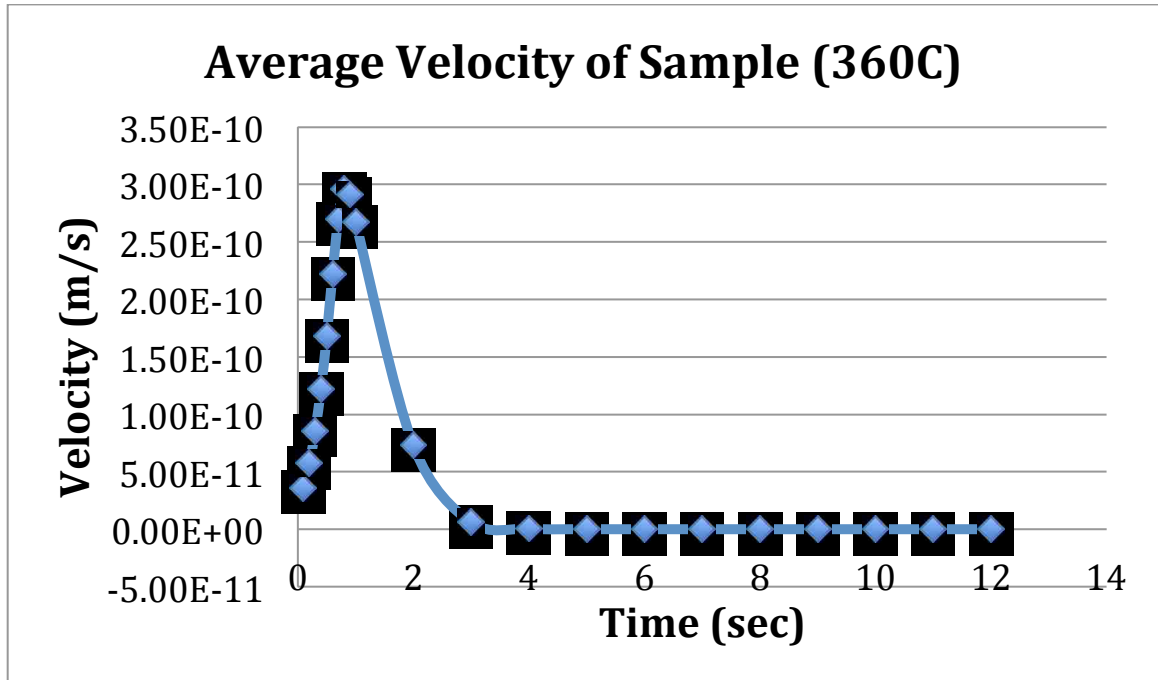
Figure 4.51: *Average velocity of ZBLAN sample heated from 250°C to 360°C from 0 to*

12 seconds.

The same observation can be made for the average velocity plot versus time; the

convection values increase rapidly to 0.8 seconds then decrease steadily to a much slower

velocity, due to thermal shock (initially) proceeded by thermal equilibrium after

approximately 2 seconds.. These velocity numbers for ZBLAN were utilized in the

comparison of the diffusion versus convection mobility terms.

4.9 Convection and Diffusion Comparison

The Péclet number represents the rate of advection of a physical quantity by the

flow to the rate of diffusion of the same quantity. The Péclet number can be seen in Eq.

4.17.

$$Pe_L = \frac{LU}{D}$$

144

Where *L* represents the characteristic length, *U* is the contribution due to convection (velocity), and *D* is the contribution due to diffusion. Using the Péclet number at the two key temperatures (360°C and 380°C) previously investigated can better show the dominant mobility contributor. The resulting Péclet numbers for each temperature can be seen in Table 4.4.

Table 4.4: *Péclet number for ZBLAN at 360°C and 380°C.*

Pe #	
360°C (1-g)	380°C (μ-g)
6.87	6.82E-06

The Péclet number results shown in Table 4.5 depict the mobility contribution due to convection in 1-g and μ-g at the two temperatures. The contribution due to convection in μ-g has almost no affect on the mobility of ZBLAN. The contribution due to diffusion is the dominant component in a μ-g environment. In a 1-g environment neither mobility term dominates by evidence of the Péclet number at 360°C. The Péclet number at that temperature and gravity level isn't excessively large or small which suggests neither term is dominant.

An additional comparison can now be made between the independently calculated diffusion and convection numbers. In order for an accurate comparison to be made, the diffusion coefficient value is divided by the characteristic length of the sample (1mm) as previously done via the Péclet number. This process results in a diffusion velocity in m/s, which can now be compared to the convection velocity from the COMSOL models, also in units of m/s. The diffusion number is obtained from the aforementioned Stokes-Einstein equation (Eq. 4.6 and Figure 4.40) utilizing the average molecular radii,

calculated at a temperature of 360°C and 380°C. The convection numbers were obtained

from the previously described convection analysis (Figure 4.50). The calculated values

are described and totaled in Table 4.5.

Table 4.5: *Diffusion and convection numbers at 360°C (1-g) and 380°C (μ-g).*

	360°C		380°C	
	ΔD	ΔC (1-g)	ΔD	ΔC (μ-g)
	1.31E-11	9.03E-11	1.01E-10	6.87E-16
Total	1.03E-10		1.01E-10	

The data described in Table 4.5 shows that the mobility term due to diffusion increases

by an order of magnitude when increasing the temperature by 20-degrees. Also noticed is

that the velocity term due to convection is on the same order of magnitude at 1-g,

however, the convection value under microgravity is negligible. As shown in Table 4.4,

the totals of convection plus diffusion at both temperatures are essentially equal. Also

depicted is that the total at 360°C is an order of magnitude higher than that of the

diffusion term. This shows how the contribution of convection plays an important role in

the mobility of ZBLAN glass. Ultimately, the totals from the diffusion plus convection in

μ-g approximately equal that of diffusion plus convection in 1-g. Although the numbers

of low magnitude, Leed & Pantano (2007) describe that the distance between active and

inactive growth sites are on the order of Ângströms. Therefore, molecules don't have to

move a great distance in order to contribute to crystallization and suppressing the

dominant mobility term (convection) suppresses crystallization.

Based on the micrograph evidence described in earlier sections, ZBLAN

crystallizes irrespective of a μ-g environment at high temperatures (~410°C). This

evidence is supported by the high diffusion coefficient present at 410°C (9.47E-10m/s) as

compared to the total contribution of convection and diffusion at 360°C (1.03E-10m/s). The mobility due to diffusion at 410°C is on the same order of magnitude as that of the total contribution of convection and diffusion at 360°C, therefore removing convection at high temperatures is not effective in the suppression of crystal growth. Conversely, removing the convection term from the 360°C sample leaves a small diffusion term, resulting in a ZBLAN sample with minor crystal growth.

4.10 Conclusions

Overall, this analysis describes the heat and mass transfer mechanisms governing crystal growth/suppression in a 1-g and μ-g environment under varying temperatures. A novel equation relating crystallization to advection (diffusion plus convection) in μ-g and 1-g was developed and analyzed. The basis for the equation was formed from micrograph and gray value conclusions showing that ZBLAN crystallizes at 380°C in μ-g and at 360°C in 1-g. The analysis showed that the contribution due to convection is a major contributor to crystal growth in a ZBLAN sample and removing this term by μ-g means results in a suppression of crystallization within a given temperature range. Suppressing convection by microgravity processes inhibits the crystallization cross-over point (from amorphous to crystalline) in ZBLAN. At a certain point, approximately 410°C, μ-g processing of ZBLAN to suppress crystal growth becomes irrelevant. This result is sufficient due to fiber drawing temperatures never exceeding the crystallization temperature (360°C).

CHAPTER 5 – Assessment of Thermal Degradation and Fracture of ZBLAN Fibers

This chapter describes the separate study of the thermal degradation and fracture analysis of ZBLAN fibers. This chapter includes an inclusive literature review pertaining to the fracture analysis and effect of micro-crystal formation in a vitreous material.

5.1 Introduction

The ZBLAN glass fiber drawing process involves heating a preform to within its working temperature range, ΔT, approximately bounded by the glass transition temperature, T_g (265°C), and the crystallization temperature, T_x (365°C) [Harrington, 2004]. Other sources report a similar ZBLAN T_x of approximately 360°C [Wilson, 1985]. ZBLAN samples obtained for this study were acquired from OgMentum Inc. The part number for these samples is ZMF-160/200. The polymer protective coating was removed via non-invasive chemical stripping. The average peak DSC (Differential Scanning Calorimetry) results were: $T_g = 265$°C and $T_x = 377$°C which provides a working temperature of, $\Delta T = 112$°C. Due to this narrow working range, ZBLAN is a difficult glass to draw into fiber form. It is also documented that ZBLAN is very susceptible to crystallization growth at temperatures above its glass transition temperature [Harrington, 2004]. The final process in typical fiber drawing set-ups is a take up reel. The purpose of the take up reel is to collect the completed fiber until the drawing process is complete. Due to ZBLAN's crystallization potential, the diameter of the take up reel needs to be adequately sized so that the fiber doesn't break, which would cause the drawing process to be disrupted. This research quantifies the minimum take up reel diameter based on the amount of crystallization induced in the fiber across a range of

drawing temperatures. This information is also pertinent to subsequent handling and storage of ZBLAN fibers to avoid damage and breakage.

5.2 Effect of Micro-crystals on Fiber Fracture

There are key microstructural differences between the properties of an amorphous ceramic and a polycrystalline ceramic. Optical waveguides such as ZBLAN are amorphous materials at room temperature but become polycrystalline at higher temperatures. Microcrystals formed during heating constitute inherent flaws, which play a strong role in the mechanical properties and the handling ability of optical waveguides, in particular ZBLAN fibers. The property of the fiber to flex and bend is useful for handling and positioning the fiber in a desired application. The mechanical testing reported here consisted of bending the fibers to specific radii of curvature to determine the applied curvature at which fiber fracture occurs.

Hayashi et al. [1989] have conducted studies on the mechanical response of different types of fiber-optic cables. Since their cable consists of an outer protective plastic sheath and other materials besides the glass fiber, their research focused on modeling of strain hardening behavior in plastic and steel fibers. Park *et al.* (2001) have presented the most extensive study to date of the fracture behavior of directionally solidified $Y_3Al_5O/Al_{12}O_3$ (YAG/Alumina) fibers and also reported using the nano-indentation technique to determine fracture toughness. This paper also demonstrated how the microstructure of crystals in the YAG/Alumina fibers affects its tensile strength, ductility and micro-scale properties. Strength of the fiber was found to be in between that of its two constituent materials. The $Y_3Al_5O_{12}/Al_2O_3$ fibers heat treated in an inert atmosphere demonstrated a 40% drop in tensile strength and a corresponding drop of

149

Weibull's modulus from 11.2 to 5.6. This degradation was attributed to fracture initiation at the surface and greater reactivity of the fiber surface; surface diffusion is faster than interphase boundary diffusion and volume diffusion.

Fracture toughness of glass in fiber form is not readily available since test standards developed for bulk material are not applicable to small fibers. Researchers have therefore resorted to using the micro-indentation tests and correlating the results to fracture toughness K_{Ic} values [Anstis, 1981]. The authors describe the errors that arise from the nonlinear fracture processes and provide a comparison of K_{Ic} data from indentation vs. conventional means. According to this paper the K_{Ic} values of commonly found amorphous glasses vary from 0.68 – 0.91 MPa m$^{1/2}$. This can however vary by a factor of 5 depending on material composition and test technique. Gong et al. (2001) determined fracture toughness values of soda-lime glass based also on the indentation technique. They reported a coefficient of variation greater than 10% is common even in fibers with identical chemical/material composition; the probability distribution function of K_{Ic} values of soda-lime glass was reported to be in the range of 0.5 to 0.9 MPa m$^{1/2}$. Nötzolda et al., (2010) investigated the effect of residual stresses on fracture toughness in fritt-bonded glass plates. Their study showed that the effect of residual stress on fracture toughness depends on the nature of fracture (pure tensile vs. mixed mode).

Because of the large difference in fracture toughness values reported in the available literature and the lack of K_{Ic} values for ZBLAN, a qualitative analysis using fracture mechanics principles was used. This analysis is based on the premise that fracture initiates on the surface due to the propensity of surface crystal growth during heating (Figure 5). Geometry dependent stress intensity factors determine stable or

unstable crack growth that ultimately leads to fiber fracture at various levels of applied curvature.

5.3 Experimental Program

<u>Heat Treatment and Controlled Bending Tests</u>

Multiple ZBLAN fibers were subjected to a range of temperatures for a designated amount of time. The processing temperatures were selected so that a clear crystallization transition is evident when investigating the sample using the optical microscope. The temperatures spanned from below the glass transition temperature to above the crystallization temperature in small increments. Time dependent degree of crystallization at temperatures near or at Tx and Tg were also investigated. The samples were then wrapped around an aluminum fixture of a known diameter. The fixture was machined out of 6061-T6 aluminum with a Computer Numeric Controlled (CNC) router by the University of New Mexico Mechanical Engineering machine shop. The fixture has a maximum diameter of 20.32 cm (8 in.) and a minimum diameter of 1.27 cm (0.5 in.) in 1.27 cm (0.5 in.) increments and confirmed via high precision calipers to be within ± 0.127 mm (0.005 in) of the specified dimension. A photograph of the fixture can be seen in Figure 5.1.
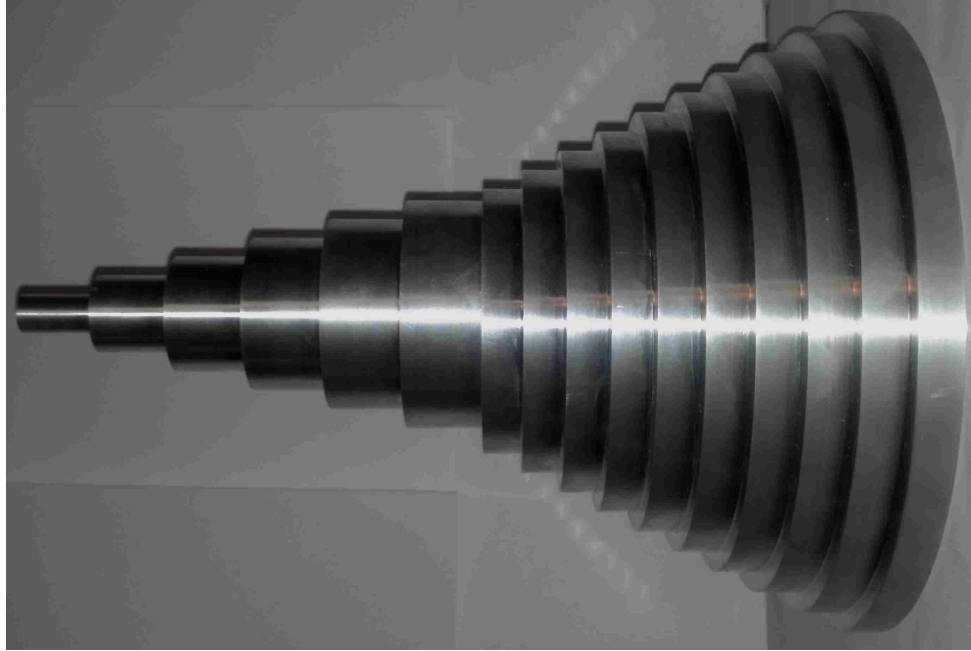
Figure 5.1: *A photograph of the fiber-wrapping fixture.*

The ZBLAN fibers tested had a diameter of 200 ± 10 μm (4.33E-3 in.) and an average length of 3.81 cm (1.5 in.). The length of the ZBLAN fiber was limited by the size of the heating oven and the amount of material available for this experiment. The oven used for this experiment is a Thermocyn oven calibrated to a local variance of ±0.5°C of the controller readout. The test matrix for this experiment can be seen in the 1st three columns of Table 5.1. After the fiber was heated, it was then wrapped around the fiber-wrapping fixture until failure was obtained. Failure was considered when the fiber separated into two or more segments. Each test was conducted with three separate fibers and the failure radius was averaged to the nearest half inch. The minor variance in the failure diameter was ± 1.27 cm (0.5 in.) and was a rare occurrence. Most tests failed at the same radius of curvature for all three samples.

$$\varepsilon = y\rho$$

Where ε is the strain at the location y measured from the neutral axis (center of fiber) and ρ is the known curvature of the fiber at failure defined as the inverse of the Radius of Curvature ($\rho = 1/R$) in Figure 5.2.
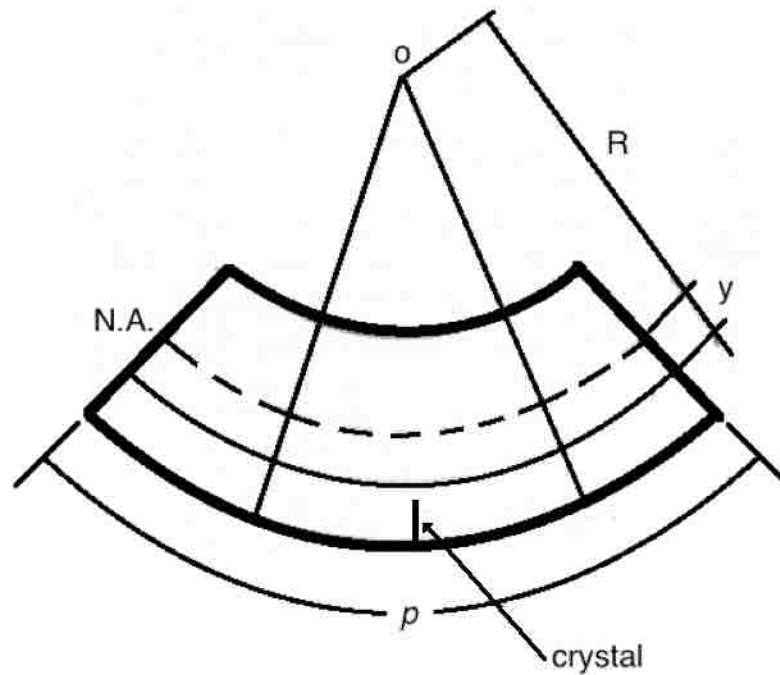
Figure 5.2: Schematic showing curvature of bent fiber with microcrystal located on the surface of the fiber.

Since glass is known to be a linear elastic material, stress σ is proportional to the applied strain ε. Therefore the maximum stress applied to the glass is on the outermost surface and is proportional to the applied curvature. The results of the mechanical wrapping test

can be seen in the last two columns of Table 5.1. The strain data was calculated using Eq. 5.1.

**Table 5.1:** *Results of mechanical wrapping test.*

| | | | ZBLAN Fiber | |
Test #	Temp. (˚C)	Duration (sec)	Failure Diameter (cm) [in.]	Strain at Failure
Control	N/A	N/A	11.43 [4.5]	1.75E-03
Test 1	270	60	13.97 [5.5]	1.43E-03
Test 2	290	60	12.70 [5.0]	1.57E-03
Test 3	300	60	13.97 [5.5]	1.43E-03
Test 4	300	120	13.97 [5.5]	1.43E-03
Test 5	300	240	12.70 [5.0]	1.57E-03
Test 6	300	480	13.97 [5.5]	1.43E-03
Test 7	310	60	12.70 [5.0]	1.57E-03
Test 8	320	60	13.97 [5.5]	1.43E-03
Test 9	330	60	12.70 [5.0]	1.57E-03
Test 10	340	60	13.97 [5.5]	1.43E-03
Test 11	350	60	13.97 [5.5]	1.43E-03
Test 12	360	10	13.97 [5.5]	1.43E-03
Test 13	360	30	15.24 [6.0]	1.31E-03
Test 14	360	60	15.24 [6.0]	1.31E-03
Test 15	360	120	13.97 [5.5]	1.43E-03
Test 16	360	240	15.24 [6.0]	1.31E-03
Test 17	360	480	16.51 [6.5]	1.21E-03
Test 18	370	30	15.24 [6.0}	1.31E-03
Test 19	380	30	16.51 [6.5]	1.21E-03
Test 20	390	30	16.51 [6.5]	1.21E-03
Test 21	400	30	20.32 [8.0]	9.84E-04
Test 22	420	30	19.05 [7.5]	1.05E-03
Test 23	450	30	20.32 [8.0]	9.84E-04

A graphical representation of the heat treatment temperature (constant soak time) versus failure diameter and the corresponding failure strain can be seen in Figure 5.3 and Figure 5.4 respectively. Initially increasing temperature does not reduce strain at failure. Between 360°C and 400°C strain at failure decreases with increasing temperature, while

beyond 400°C it reaches a steady state. These observations will be explained with a

fracture mechanics based model later in this document.
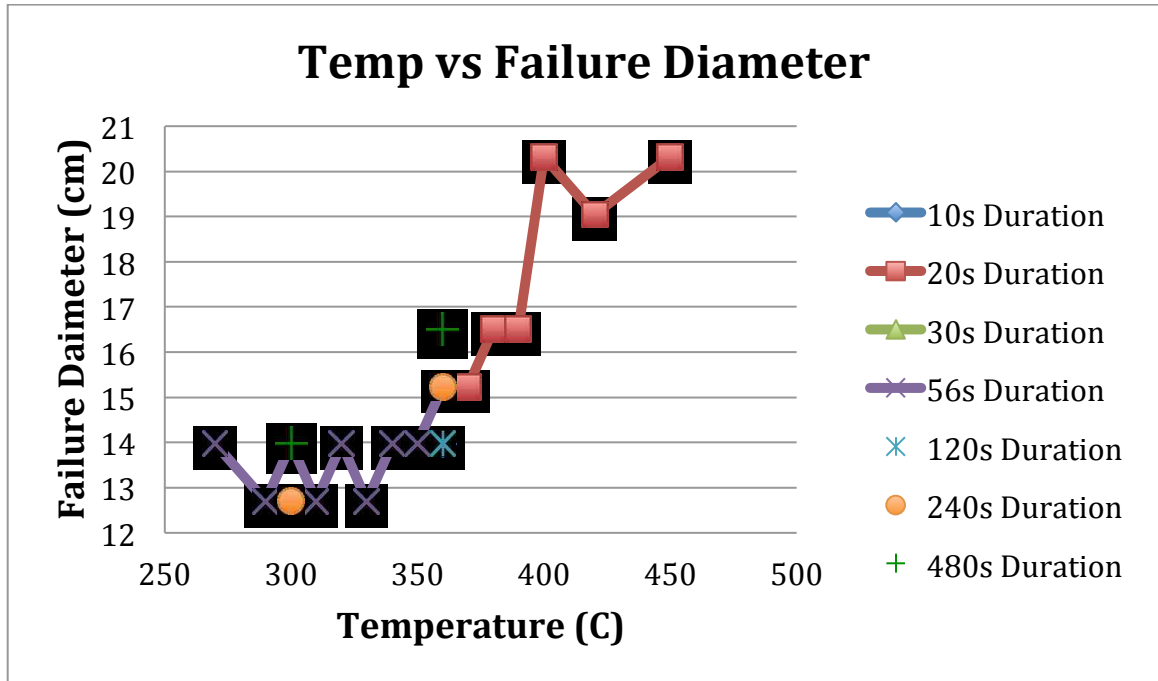
Figure 5.3: *Temperature versus failure diameter of ZBLAN fiber wrapping test.*
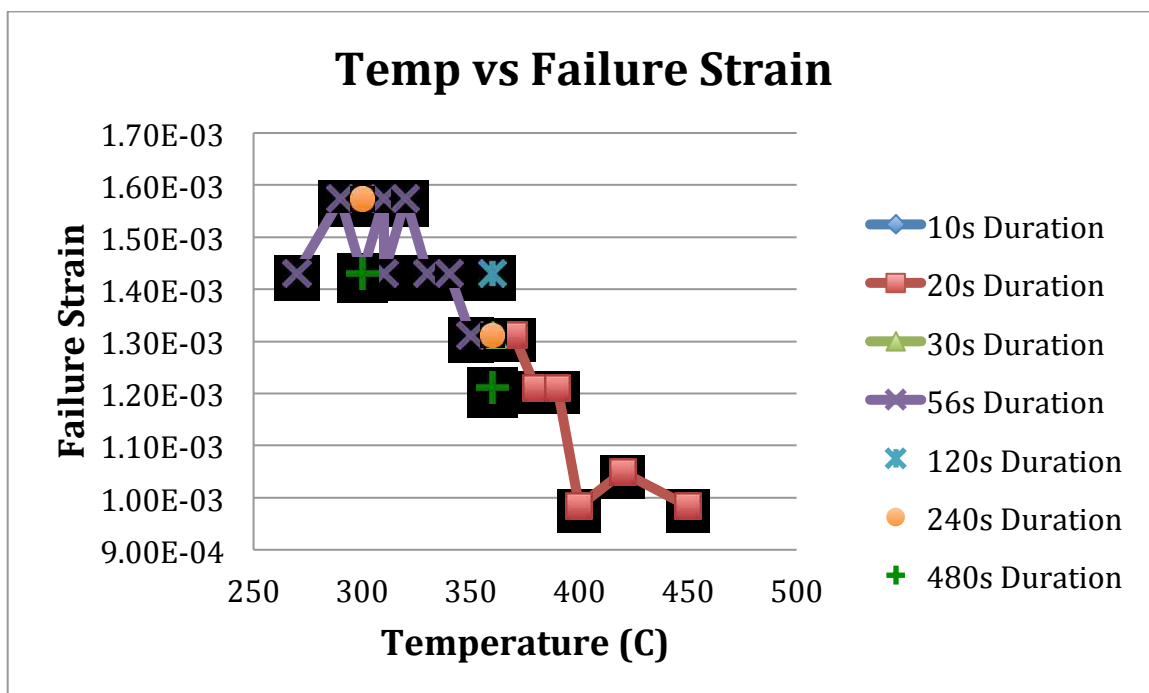
Figure 5.4: *Temperature versus failure strain of ZBLAN fiber wrapping test.*

As seen in Figure 5.4, the temperature versus failure strain graph is a reflection of the

temperature versus failure diameter, Figure 5.3. This is due to the radius of curvature of

the bend fiber being inversely proportional to the resulting strain on the outer edge of the

fiber. Figure 5.3 shows that the higher the soak temperature the lower the bending

capabilities of the fiber. Similarly, Figure 5.4 shows that at higher temperatures the fiber

fails at a lower strain. Overall, the crystallinity is directly correlated to the brittleness of

the fiber.

Scanning Electron Microscope (SEM) and Optical Microscope Observations

Figure 5.5 a-c shows Scanning Electron Microscope (SEM) photos of samples

heat treated to 270°C (60 sec), 360° (60 sec) and 400°C (30 sec). Very fine crystal

formation can be seen in Figure 5a corresponding to 270°C. Upon 360°C heating, larger

(~50μm) surface crystals are noticeable (Figure 5.5b). At 400°C the surface crystals are

more numerous (Figure 5.5c). Based on this observation and literature survey, along with the fact that bending induces greatest stress at the outer edge of a fiber, it was conjectured that crack initiation from the micro-crystals formed on the surface are responsible for the fracture. A fracture mechanics based model was therefore investigated to study the growth of surface cracks into a glass fiber and the consequent decrease in bending radius of fibers treated to a higher temperature.
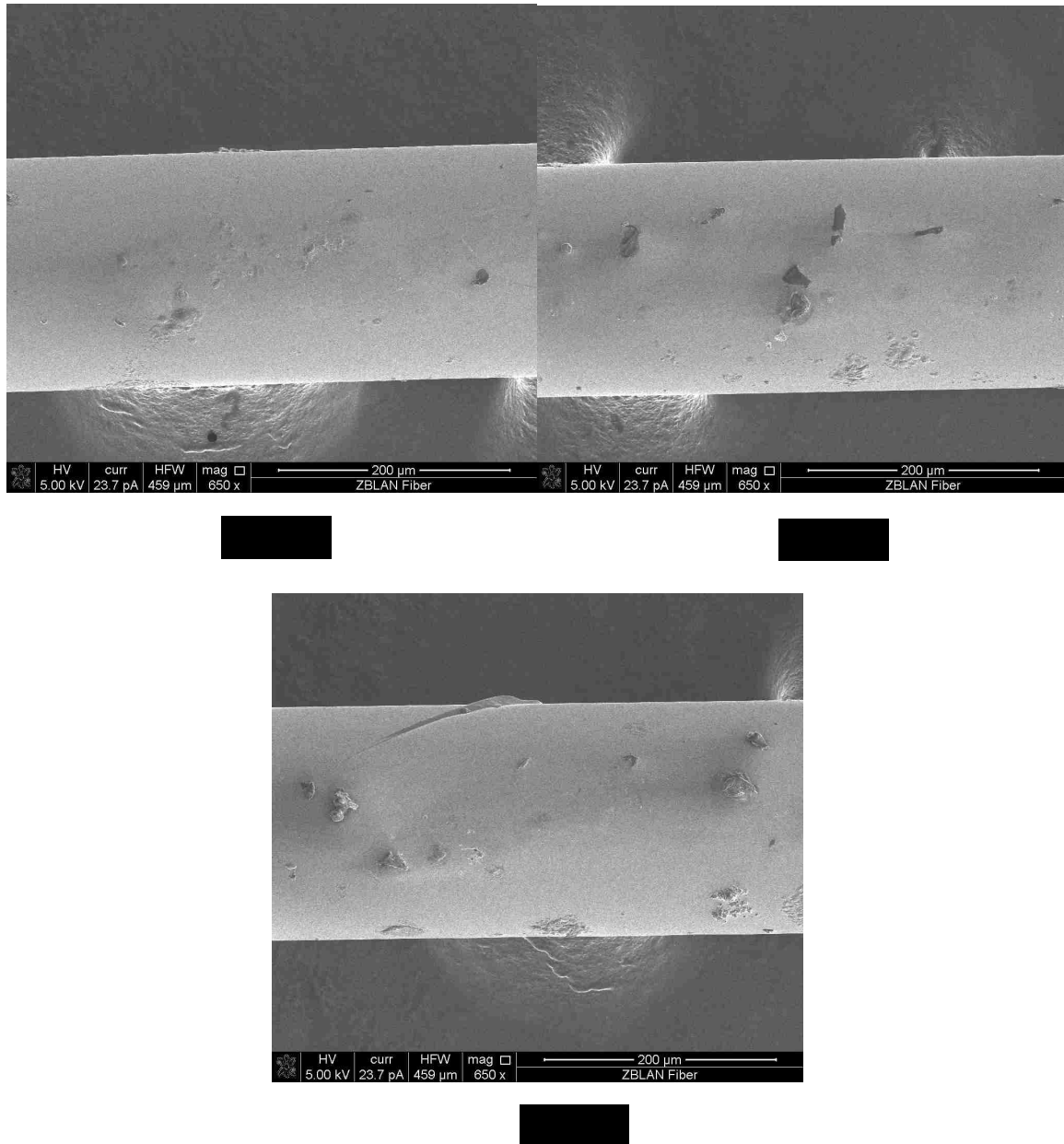
Figure 5.5: a-c, SEM Micrograph of Fibers Heat Treated to 270° (60 sec), 360° (60 sec)

and 400°C (30 sec).

Comparing the previously discussed ZBLAN preform samples (Section 4), the

360°C, 0-g, processed samples under SEM (Figure 4.35) shows smaller surface

crystallization than that of the 1-g ZBLAN fiber in Figure 5.5b. The average crystal size

in Figure 5.5b is approximately 50μm whereas the average surface crystal size in the 0-g

ZBLAN sample is 10μm. The higher temperature sample, 400°C, shows a corresponding surface crystal size (50μm) to that of the 0-g processed (25μm) sample (Figure 4.36). This result continues to show that 0-g processing suppresses the crystallization of ZBLAN samples and can be utilized to increase the wrapping ability of ZBLAN fibers.

Further investigation utilized an optical microscope (Olympus BX51) in polarized light transmission mode to display the crystallinity of the failed ZBLAN fiber. A ZBLAN fiber that was not subjected to any heat treatment was considered as the control fiber. The control fiber failed at an average wrapping diameter of 11.43 cm (4.5 in.) and a corresponding micrograph can be seen in Figure 5.6.
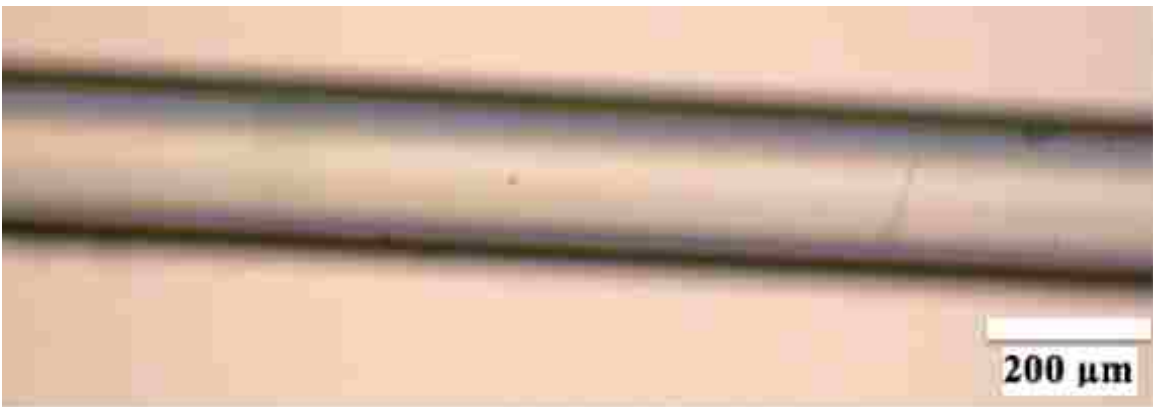
Figure 5.6: Optical micrograph of the as received control ZBLAN fiber.

The micrograph shown in Figure 5.5 and all micrographs hereafter represents an average depiction of the entire length of the fiber. Multiple micrographs were taken of each sample and the most clear and representative was selected for reporting purposes. Figure 5.6 shows that the fiber is relatively clear of any crystallites at this magnification level (X100). This finding is consistent with the expectations of the as-received fiber. The first test in the test matrix (Table 5.1: Test 1) is a fiber processed at 270°C for a duration of 60 seconds. A corresponding micrograph can be seen in Figure 5.7.
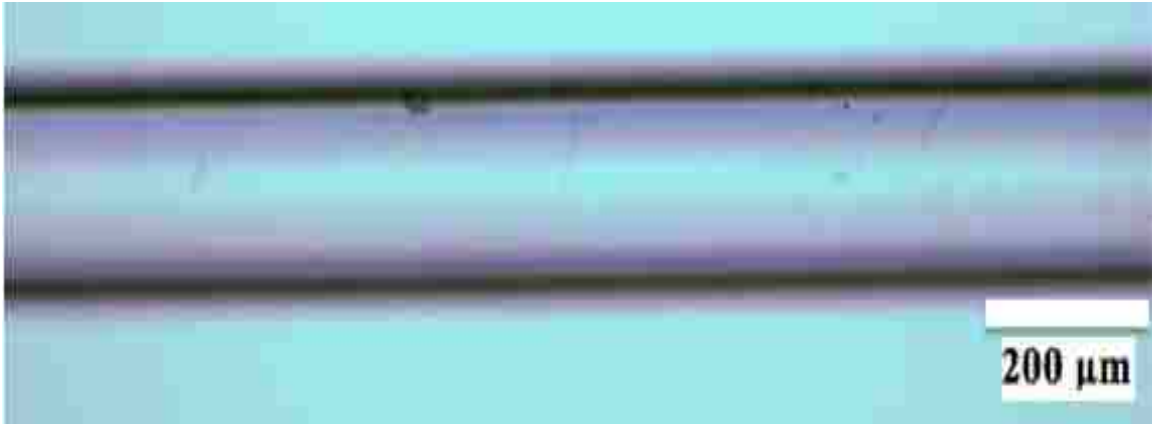
Figure 5.7: Micrograph of a ZBLAN fiber processed at 270°C for 60 seconds.

Figure 5.7 is similar to the clarity shown in Figure 5.6, however, Figure 5.7 has a few more noticeable crystals on the surface than the control sample. Test 5.1 failed at an average diameter of 13.97 cm (5.5 in.) compared to the 11.43 cm (4.5 in.) of the control fiber. Continuing to test 3, a fiber processed at 300°C for a duration of 60 seconds is shown in Figure 5.8.

Figure 5.8: Micrograph of a ZBLAN fiber processed at 300°C for 60 seconds.

Figure 5.8 shows similar amounts of crystal growth as displayed in Figure 5.7. This is consistent with the results of the wrapping test, as both samples failed at the same diameter interval, 13.97 cm (5.5 in.).

Next in the test matrix was examining the effect of extending the time at a constant temperature to establish if a ZBLAN fiber in unit gravity, at a temperature above Tg and below Tx, will crystallize more if the crystals are allowed more time to grow. Test 6 in the test matrix allowed the ZBLAN fiber to be heated at 300°C for a duration of 8 minutes. A micrograph representing Test 6 can be seen in Figure 5.9.
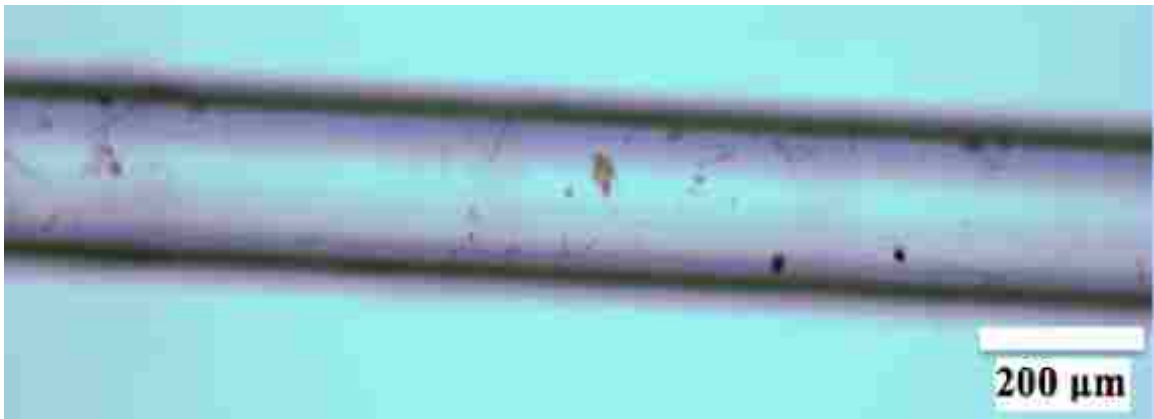
Figure 5.9: *Micrograph of a ZBLAN fiber processed at 300°C for 8 minutes.*

This time dependent study of crystallization in a ZBLAN fiber below the crystallization temperature showed a small amount of enhanced crystal growth, however, no effect on the bendability of the fiber. The average failure diameter of the 300°C ZBLAN fiber at 8 minutes failed at the same diameter of the 300°C ZBLAN fiber at 60 seconds, 13.97 cm (5.5 in.). This demonstrates that small increase in crystal growth does not affect the wrapping ability of the fiber. Similar test at the crystallization temperature (360°C) show different results. Figure 5.10 and Figure 5.11 represent a ZBLAN fiber processed at 360°C for a durations of 10 seconds and 30 seconds, respectively.
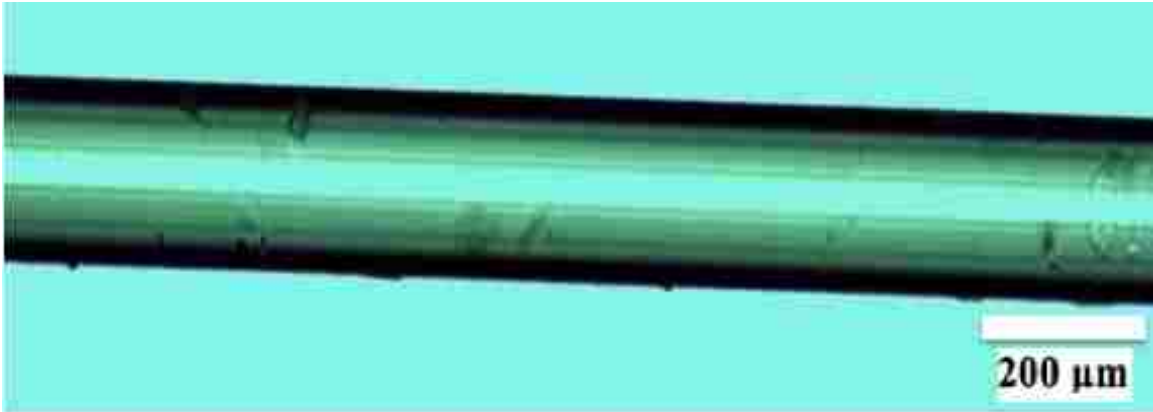
Figure 5.10: Micrograph of a ZBLAN fiber processed at 360°C for 10 seconds.
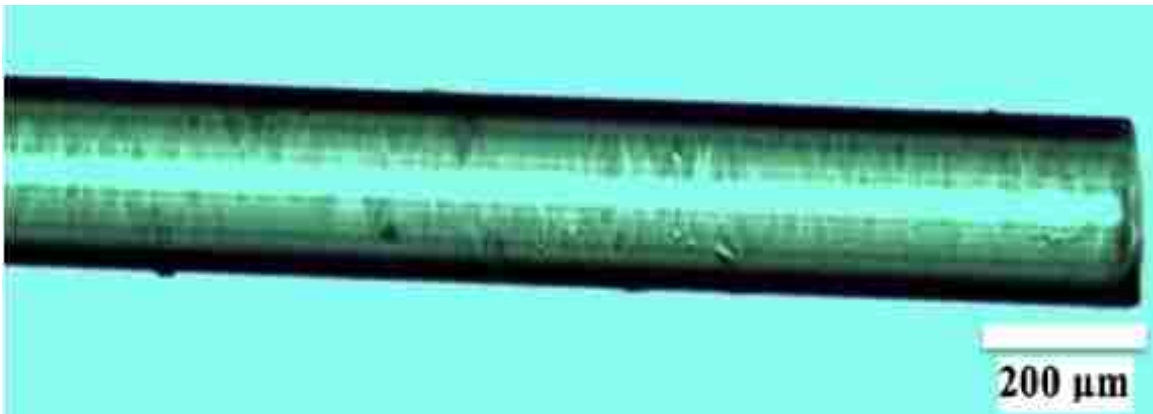
Figure 5.11: Micrograph of a ZBLAN fiber processed at 360°C for 30 seconds.

Both Figures 5.10 and 5.11 show more evidence of crystallization than the lower

temperature processed fibers. The fiber processed for only 10 seconds failed at the

previous diameter of 13.97 cm (5.5 in.) while the fiber processed for 30 seconds failed at

a diameter of 15.24 cm (6.0 in.). The 20 second increase in processing time constituted a

1.27 cm (0.5 in.) jump in failure diameter. Although the wrapping fixture is only limited

to 1.27 cm (0.5 in.) increments, this result shows that at the crystallization temperature,

the amount of crystallization is dependent upon the processing time. Figure 5.12 shows a

ZBLAN fiber processed at 360°C for a duration of 8 minutes (480 seconds).

Figure 5.12: *Micrograph of a ZBLAN fiber processed at 360°C for 8 minutes.*

It can be seen that a fiber processed at the crystallization temperature (360°C) for a span

of 8 minutes shows strong evidence of crystallization. When put through the wrapping

test spectrum the fiber fails at 16.51 cm (6.5 in.) as compared to the ZBLAN fiber

processed at the same temperature for 30 seconds, 15.24 cm (6.0 in.). The results showed

that processing time at the crystallization temperature does have a minor effect on the

crystallization and wrapping ability of the fiber. The next fiber processed was at a

temperature of 370°C for a period of 30 seconds, a micrograph of this sample can be seen

in Figure 5.13.
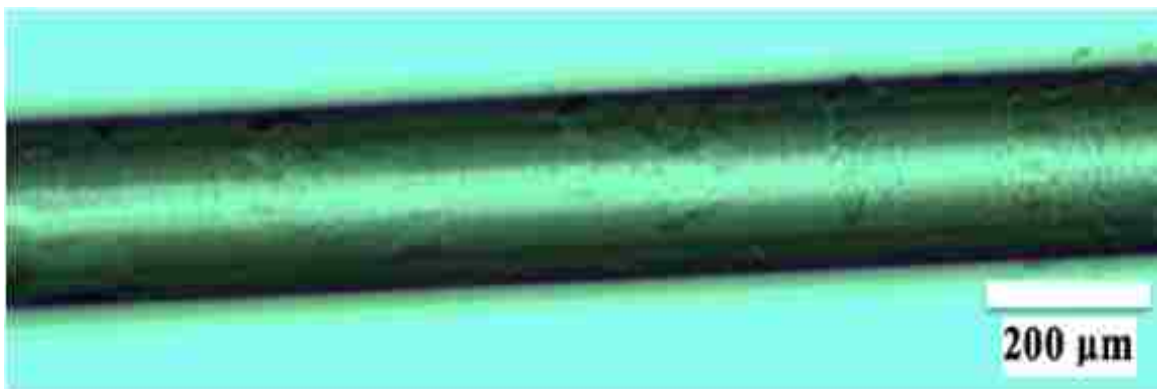
Figure 5.13: *Micrograph of a ZBLAN fiber processed at 370°C for 30 seconds.*

The ZBLAN fiber processed at 370°C for a duration of 30 seconds appears to have the same crystallinity as the 360°C fiber heated for 8 minutes however its average failure diameter was 1.27 cm (0.5 in.) lower. However, the following test (Test 19) on a ZBLAN fiber processed at 380°C for a period of 30 seconds show results that are similar to the 360°C sample for 8 minutes.
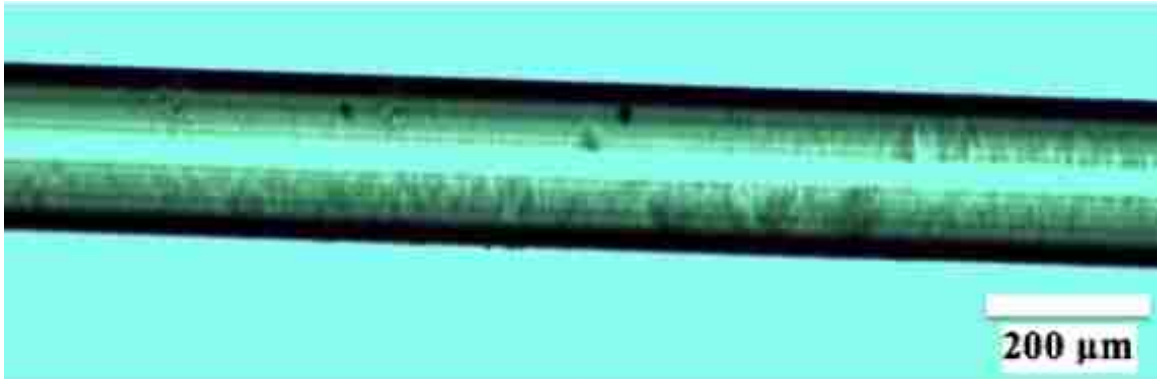
Figure 5.14: Micrograph of a ZBLAN fiber processed at 380°C for 30 seconds.

The crystallization pattern of test 19 shown in Figure 5.14 is similar to that of Figure 5.12 and Figure 5.13. The evidence of crystallinity is indistinguishable at this point in the crystal growth of the material. Continuing on the test matrix, Test 21 processed a ZBLAN fiber at 400°C for a duration of 30 seconds. Figure 5.15 shows the micrograph corresponding to Test 21.

Figure 5.15: *Micrograph of a ZBLAN fiber processed at 400°C for 30 seconds.*

The ZBLAN fiber processed at 400°C for 30 seconds shows a different crystallization structure than the previous crystallized fibers. This sample appears to have long branching fiber growth as opposed to the grainy, light impeding, texture of the other samples. These were also the first samples where crystallization was visible with the naked eye. The samples were white in color as opposed to the transparent glassy color of the previous samples. This sample failed at a diameter of 20.32 cm (8.0 in.), the maximum extent of the wrapping apparatus. The final two tests at higher temperatures had similar results as the 400°C tests. The results show that at the loss of wrapping ability (strain at failure) is significant at temperatures above than the crystallization temperature (360°C).

5.4 Fracture Mechanics Analyses

In consideration for the weak interface between the microcrystal and the bulk amorphous phase, a fracture mechanics based analysis was conducted. The objective of this qualitative analysis is to determine how the size and shape of a crystal growing from

the surface of a cylindrical fiber can influence the stress intensity factor and initiate

fracture. For this analyses the following assumptions were made:

    i.   Cracks initiate from the edge of a crystal

    ii.   Linear Elastic Fracture Mechanics is applicable, considering that the

        material is glass, which is known to be brittle. Therefore, the value of the

        Stress Intensity Factor (SIF) determines stable and unstable crack growth.

In fracture mechanics the Stress Intensity is used to predict the stress state (stress

intensity) at the location of the crack tip due to a force or residual stress. The magnitude

of the SIF depends on the sample geometry, the size and location of the crack, and the

magnitude and location of the loads applied to the sample. Various fracture mechanics

models have been developed to determine the SIF for specific geometric conditions and

loading.

An analytical solution for a semi-circular shaped crack (simulating the interface

of a microcrystal) on the surface of a long cylinder (fiber) undergoing pure bending or

curvature is available from Al-Laham, (1998). The consequent Stress Intensity Factors

(SIFs) (K_{IA} and K_{IB}) at locations A and B (Figure 5.16) are given by Eq. 5.2.

$$K_{IA/B} = \sqrt{\pi a} \left(\sigma f_{bg}^{A/B} \left(\frac{a}{t}, \frac{2c}{a}, \frac{R_i}{t} \right) \right)$$

Therefore K_{IA} determines crack growth into the fiber and K_{IB} determines crack growth

along the surface of the fiber. At any point in time, the larger of the two determines the

preferred mode of crack propagation. In Equation 5.2, *a* represents the depth of the crack,

2c represents the width of the crack, *t* is the thickness of the cylinder, *Ri* is the inner

radius of the cylinder, σ is the outer fiber bending stress, and f_{bg} represents the geometric

function at locations A or B. A schematic of the cylinder can be seen in Figure 5.16.
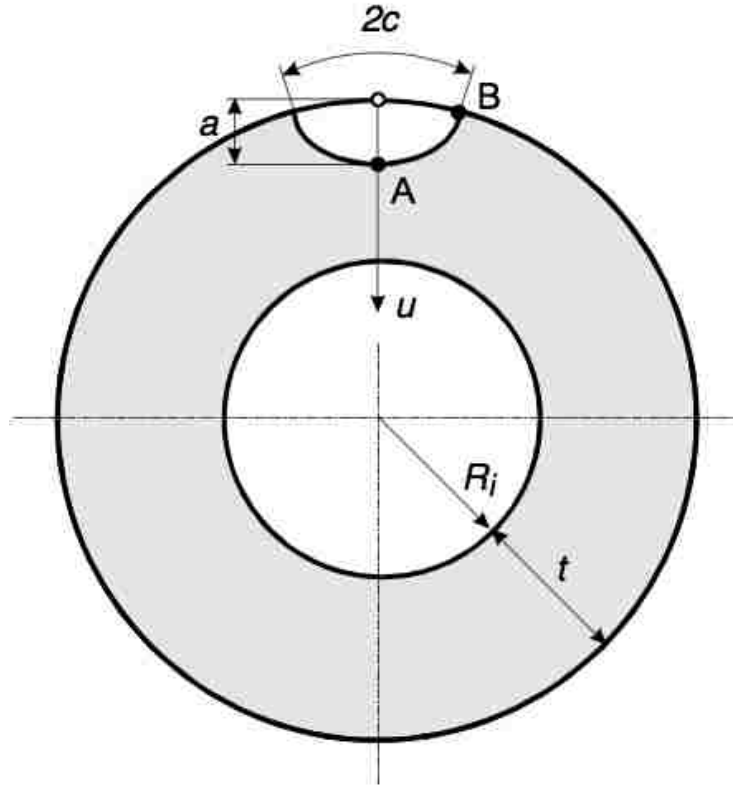
Figure 5.16: *Schematic of semi-circular shaped crack on the surface of a fiber [Al-*

Laham, 1998].

Although the model represents a hollow cylinder this aspect can be neglected for small

initial crack size and crack growth (a<<t). This is shown from the geometric function

(f_{bg}) tables provided by Al-Laham, (1998), shown in Table 5.2.

Table 5.2: *Geometric functions (f_{bg}) at point A for a/t values of 0 & 0.2 and Ri/t values of 5 & 10 [Al-Laham, 1998].*

2c/a=2, Ri/t=5	
a/t	f_{bg}
0	0.659
0.2	0.645
2c/a=2, Ri/t=10	
a/t	f_{bg}
0	0.659
0.2	0.653

The geometric function values (f_{bg}) only had a 1% variance from *a/t* of 0.2 when the R_i/t

value has doubled. Therefore, limiting *a/t* crack size values between 0.0 and 0.2 will

allow the Al-Laham, (1998) model to best serve as a fracture analysis for this study.

Although Al-Laham's model provides tables for both *Ri/t =5 and 10*, the smaller value of

5 was used for all further calculations. Table 5.3 shows initial values used for the fracture

mechanics models.

Table 5.3: *Initial values used for fracture model calculations.*

Property	Value	Units
Diameter of Fiber	200	μm
σ	6.94E+07	Pa

The sigma (σ) value used is the average stress value obtained from the wrapping tests.

Critical Stress Intensity K_{IC} values were calculated based on average surface crystal size

measured from SEM using Eq. 5.2 to be discussed next.

Table 5.4: *K_{IC} values for ZBLAN fiber compared to known K_{IC} values of glass.*

Material	K_{IC} [Mpa.m$^{1/2}$]
Common Amorphous Glass	0.68 - 0.91[6]
ZBLAN	0.18 - 0.43

According to Anstis *et al*, (1981) the K_{IC} values of commonly found amorphous glasses vary from 0.68 – 0.91 MPa.m$^{1/2}$ and these numbers can vary by a factor of 5 depending on material composition. Since the fibers heat treated to temperatures lower than about 360°C did not degrade (see initial part of the data in Figure 5.4) it can be assumed that the size of crystals at 360°C allowed the SIF K_{IC} to reach the critical value of K_{IC}. The K_{IC} value for ZBLAN was therefore determined based on measurement of crystal size from SEM micrographs (Figure 5.5b), corresponding strain data (Table 5.1) and Eq. 5.2. Based on the SEM micrograph in Figure 5.1, the crystals on the surface are approximately 50 μm. The fibers with this type of crystal formation failed at a stress level of 40MPa determined from the strain and curvature at failure in the wrapping experimentation. Utilizing Eq. 5.2 with the geometric function for $2c/a = 2$ and 32 gives the values shown in Table 5.4. The lower value of K_{Ic} for ZBLAN as compared to common amorphous silica glass is expected based on the literature review [Anstis, 1981; Nötzolda, 2010] and common perception of the fragile nature of ZBLAN fibers.

The effect of crystal growth at higher temperatures was modeled by examining the effect of increasing crystal size on the surface (*c*) and into the fiber (*a*) as per Figure 5.16, and looking at how it affects K_I. Increasing value of K_I indicates failure at smaller applied stress (proportional to strain and applied curvature) and vice versa.
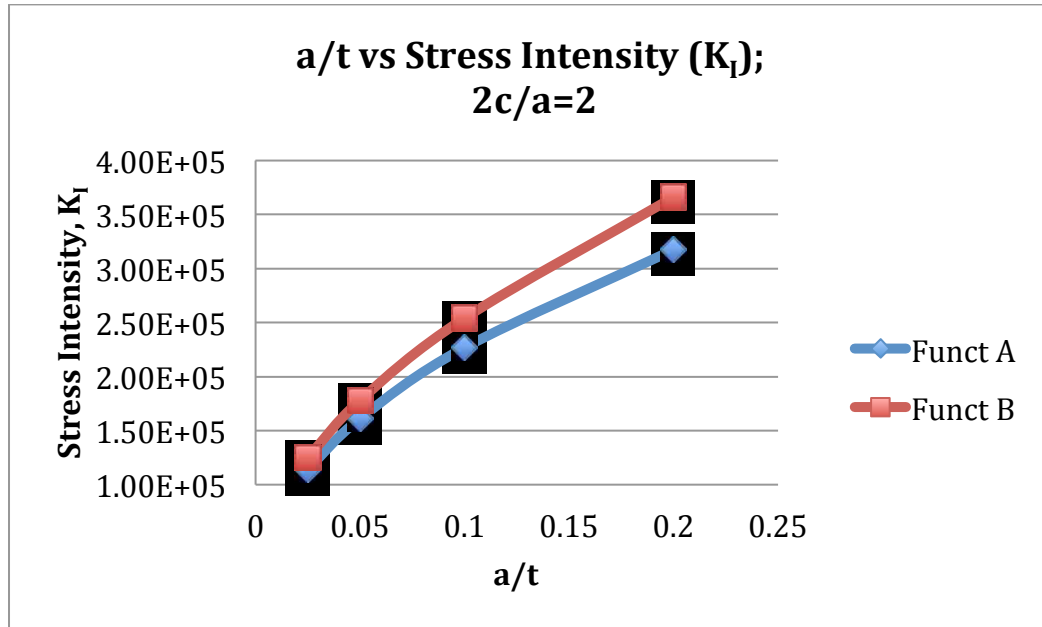
Figure 5.17: *Stress intensity vs. crack depth at constant crack width (2c/a=2).*

The first model (Figure 5.17) shows the consequence of the crack growing into the fiber; i.e. *2c/a* held constant while *a/t* increases. Figure 5.17 provides data for both geometric functions at locations A and B. In Figure 5.17, it is shown that the stress intensity values are always higher for growth on the surface (function B) of the fiber as the crack depth increases. Therefore, the initial crack will grow on the surface before growing into the fiber. Also, increasing crystal size leads to a continuously increasing K_I, and hence a continuously decreasing strain to failure.

However, the effect is the opposite if the crystal growth is on the surface (increasing 2c/a) and not into the fiber (a/t = constant). This can be seen in Figure 5.18.
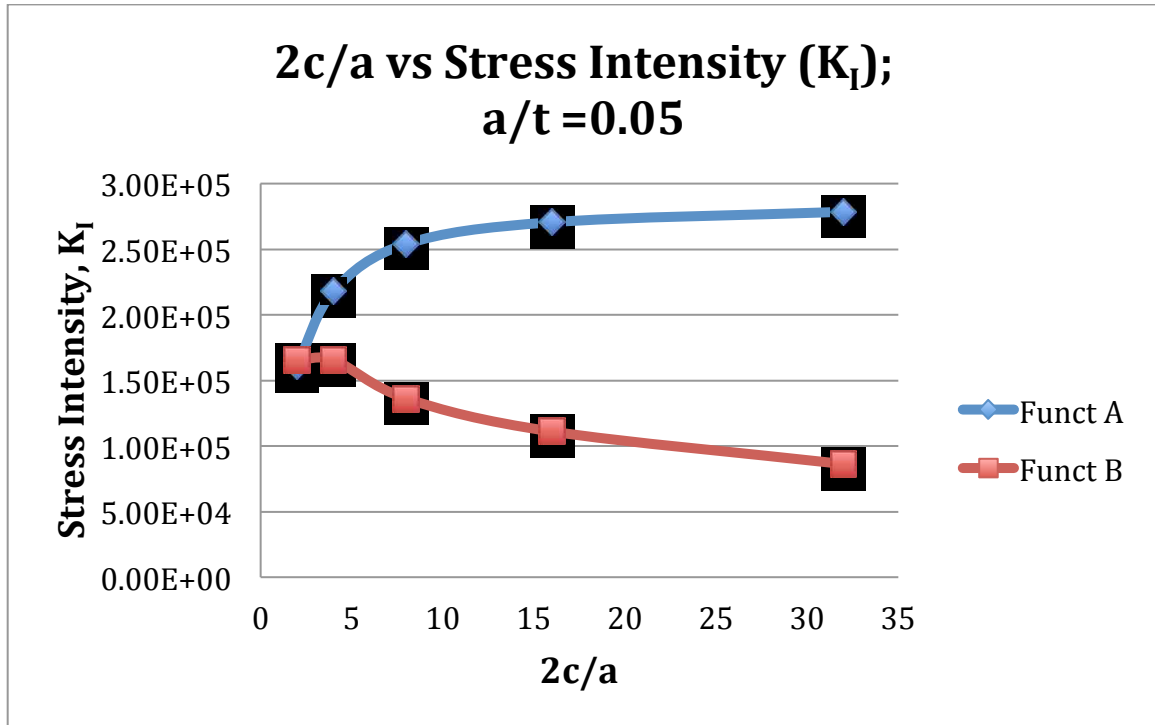
Figure 5.18: *Stress intensity vs. crack width at constant crack depth (a/t=0.05).*

Figure 5.18 represents the crack only growing on the surface with a crack depth of

a/t=0.05. The graph shows that as the crack grows on the surface, the stress intensity

factor at location B drops (stable crack growth) as the intensity factor at A increases. This

is as expected because as the crack grows on the surface, the closer the tip of the crack

gets to the neutral axis of the fiber, where the applied stress is zero. Also observed from

the graph is that as the initial crystal becomes longer (2c/a increases) the stress intensity

factor at location A initially increases but slowly tapers off at high 2c/a values. This

indicates that crystal growth will reduce strain at failure, but will reach a steady value.

This can explain the observations in our experiments (Figure 5.4) where beyond 400°C

there is no further degradation of strain at failure.

5.5 Thermal Degradation Conclusions

Multiple ZBLAN fibers were heated for a designated amount of time to induce crystal formation. The samples were then wrapped (bent) around a known diameter aluminum fixture. The diameter at which the fiber failed was recorded and photographed with the aid of optical microscopy.

The results from this study show that a take up reel of at least 15.24 cm (6.0 in.) needs to be used if drawing in a unit gravity environment. The tests completed within the working temperature range primarily failed at a diameter of 13.97 cm (5.5 in.), therefore a slightly larger diameter is recommended. As the drawing temperature gets closer the drawing temperature gets to the crystallization temperature the take up reel diameter must increase.

The duration of heating does have a temperature dependent effect on the crystallization of ZBLAN. At a processing temperature of 300°C (well below the crystallization temperature), the processing time didn't have any affect on the strength and wrapping ability of the fiber. Close to the crystallization temperature of 360°C, the micrograph depiction of crystallization was very similar but the longer duration of heating resulted in a reduced wrapping diameter.

Additionally, a connection can be made to the ZBLAN samples processed in microgravity (Section 4). Although, the ZBLAN samples in the degradation study are fibers and the ZBLAN samples are preforms in the microgravity study, the material is still of the same composition and is still prone to crystallization. The main conclusion from the microgravity study shows that crystallization is halted in microgravity. Therefore, a microgravity heat processed ZBLAN fiber wont crystallize until a

temperature of 380°C, which would also result in a higher handling ability. Whereas the 360°C (1-g) processed fibers were crystalline and failed at high bending radii (15.24 cm). Processing the same fiber at the same temperature (360°C) in microgravity will prevent crystallization, thus leading to a higher handling ability.

Lastly, the fracture mechanics analysis allowed different forms of crack initiation to be modeled. This study assumed that cracks initiate from the crystals formed on the surface of a cylindrical fiber. Therefore for very small crystals (at temperatures below 360°C), for which $K_I < K_{IC}$, there is no reduction of failure strain.

If a crack primarily grows on the surface (increase in c/a ratio) the stress intensity value decreases and does not lead to fracture. If the crystal growth is into the fiber (increasing a/t), the Stress Intensity Factor increases quickly leading to rapid and continuous drop in flexibility and strain at failure. If the crystal growth is preferentially on the surface (increasing c/a) the flexibility of the fibers initially decrease, and then approaches a constant value. This fracture analysis and conclusion is consistent with the experimental data (Figure 5.4) which shows decreasing strain to failure followed by a steady value beyond 400°C.

5.6 Future Work and Recommendations

Although this study provides useful insight into the flexibility and failure strain of ZBLAN fibers processed at different temperatures for varying duration of time, there is room for additional work. The first and foremost is the degree of crystallinity quantification. The micrographs described in this study only depict evidence of crystallization in the sense of murky texture or light transmissibility. Further techniques such as X-Ray Diffraction analysis could be implemented to better quantify the

amount/type/size of crystallites inherent in each sample. Due to the time constraints of this study, this was not completed. In addition, the wrapping fixture is limited by the size of its step increments by 1.27 cm (0.5 in). A fixture could be made that has smaller increments that would provide a more accurate determination of the failure diameter. The repeatability of the wrapping test was also limited by the amount of material available for this study.

CHAPTER 6 – Conclusions

6.1 Conclusions

In the present research, multiple ZBLAN samples were heat treated in a 1-g and µ-g environment in order to understand the role of gravity in the crystal growth suppression in ZBLAN glass. Many researchers have proven that crystallization is suppressed under microgravity conditions with minimal supporting evidence as to understanding the mechanism supporting this phenomenon. The hypothesis for this study was formed based on a literature survey and empirical evidence based on the study of heat transport mechanisms. The hypothesis for this study is that the process of mass transport known as natural convection is the primary mechanism governing crystal suppression in microgravity. Based on a literature survey and empirical understanding, nucleation and crystal growth requires movement of particles in order to gain additional growth units. Conversely, immobilizing molecular movement results in starving nuclei of collecting new growth units.

To support this hypothesis a set of experimental and analytical analysis was completed. The analytical analysis consisted of an in depth investigation into the primary mechanisms of mass transfer (mobility) present in a semi-molten ZBLAN glass sample. A COMSOL multi-physics model was developed to show the effect of conduction and convection in a ZBLAN sample that is an exact model of the experimental program. Convection is understood to be the higher order mobility term in a fluid, as opposed to diffusion. The COMSOL model and theoretical analysis shows that natural convection is directly proportional to the gravity term. Therefore, natural convection in microgravity is suppressed, leaving diffusion as the only mobility mechanism. The diffusion numbers

were determined analytically through the Stokes-Einstein equation. Unlike convection, diffusion is not affected by gravity and is only governed by temperature and viscosity. The numbers obtained for convection and diffusion were then compared and totaled to show the overall mobility of molecules within a semi-molten ZBLAN sample. Two key temperatures were investigated in this manner, 360°C and 380°C. 360°C was chosen because that is the documented crystallization temperature (T_x) of ZBLAN in 1-g. Experimental evidence from this study and literature review show that crystallization is suppressed at 360°C in μ-g. The micrograph results discussed in Chapter 4 illustrate crystallization occurs in μ-g at approximately 380°C. Thus, an investigation of the molecular mobility at these key temperatures and respective gravity conditions was completed. Since crystallization occurs at 360°C in 1-g and 380°C in μ-g, the total mobility due to diffusion and convection at 360°C (1-g) should be approximately equal to the mobility of diffusion at 380°C (μ-g) if the hypothesis is correct. The results of this analysis show that the total mobility at 360°C in 1-g (1.03E-10m/s) approximately equals that of the diffusion mobility at 380°C in μ-g (1.01E-10m/s). Therefore, the mass transport (mobility) in ZBLAN is the primary mechanism governing crystal growth suppression in microgravity.

Furthermore, the micrographs of the ZBLAN samples elucidate high amounts of crystallization above 380°C (approximately 410°C). The contribution due to diffusion at 410°C (9.47E-10m/s) is higher than that of the total mobility contribution at 360°C (1.03E-10m/s). Thus, crystallization at that high of temperatures will occur regardless of suppressing convection. Therefore, microgravity processing to suppress crystal growth at temperatures at or above 400°C is ineffective.

176

In conclusion, the results from this study support the hypothesis that the mechanism governing crystal growth suppression in ZBLAN glass is directly related to the mobility due to heat transport mechanisms, specifically natural convection and diffusion. Natural convection is the higher order molecular mobility term and can be suppressed in a microgravity environment. Suppressing convection ultimately starves growing crystallites in the sample and yields a high quality amorphous sample.

6.2 Recommendations for Future Work

Many of the results and conclusions from the present research warrant further investigation.

Firstly, additional experimentation could be completed that tailors the temperature scheme to a smaller range of temperatures. An example could be a temperature range of 360°C to 390°C in 1-2 degree increments. A smaller degree increment would more accurately show the crossover from amorphous to crystalline. This set of experimentation can be completed on the same testing apparatus used in the present study.

Furthermore, a controlled hyper-gravity environment would aid in this analysis. For the present research, a hyper-gravity environment was provided on the zero-g aircraft and utilized in the experimentation. However, due to the variability of the hyper-g environment (1.2-g - 1.8-g) it was difficult to make accurate conclusions based on the results. Overall, the hyper-g processed samples appeared to crystallize at a temperature (~340°C) below the crystallization temperature (360°C). This evidence is consistent with the conclusions of the present study. Since convection is proportional to gravity, a higher gravity term will increase convection, resulting in higher movement within the sample. Higher mobility will result in more mixing and more growth units to be collected for

crystal growth to occur. However, this temperature isn't as precise as the microgravity experiments because the variability of the hyper-g section. Thus experimentation with a controlled hyper-g environment would be extremely beneficial.

Thirdly, in the experimentation component of this research, a longer duration of microgravity would be useful. A longer time dependent study could be completed in a microgravity environment to determine the effect of time on crystallization. The thermal degradation of ZBLAN fibers study showed that there is a time dependence on crystallization and the 20 seconds of microgravity time available on the parabolic aircraft isn't enough time to test this scenario.

Lastly, multiple optical microscopy techniques were the primary investigation technique used in this study to determine crystallization of the samples. For the purposes of this study, it was only essential to display evidence of crystallization as opposed to the type and specific size of crystals. Thus, an X-Ray Diffraction (XRD) study would aid in determining the species of crystals, size of crystals, and amount of crystallinity. The amount of crystallization would be beneficial to the study such that a degree of crystallinity at varying temperatures could be presented. This analysis could show when the same amount of crystallization is present in 360°C 1-g sample to that of the microgravity processed sample.

APPENDIX A

This section describes the process involved in verifying the COMSOL convection model.

Initially, a COMOSL model of a warming glass of water was developed as per a provided COMSOL tutorial/verification model. COMSOL provided a step-by-step guide to develop a convection model for a warming glass of water. Figure A.1 shows the results obtained by developing the described model, compared to the provided results from COMSOL documentation.
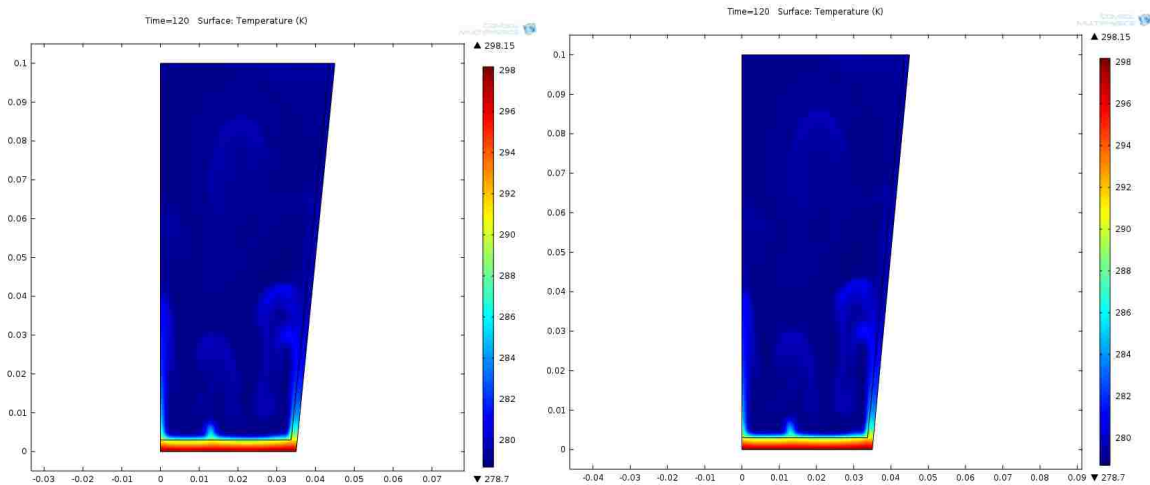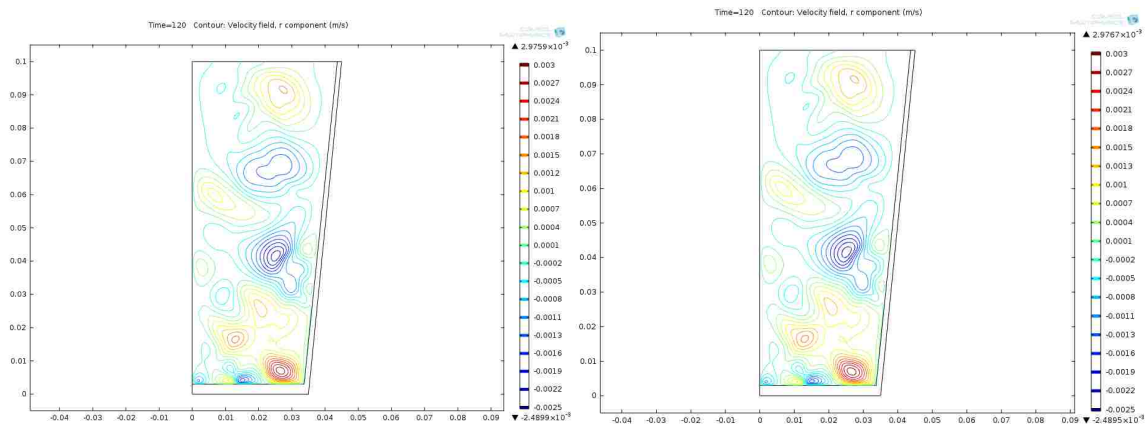

Figure A.1: *Water glass model at 2 mins. Modeled version (left) and COMSOL's version (right).*

The documentation also provided temperature gradient results for different time steps as well as results for a convection velocity contour, shown in Figure A.2 and A.3 respectively.
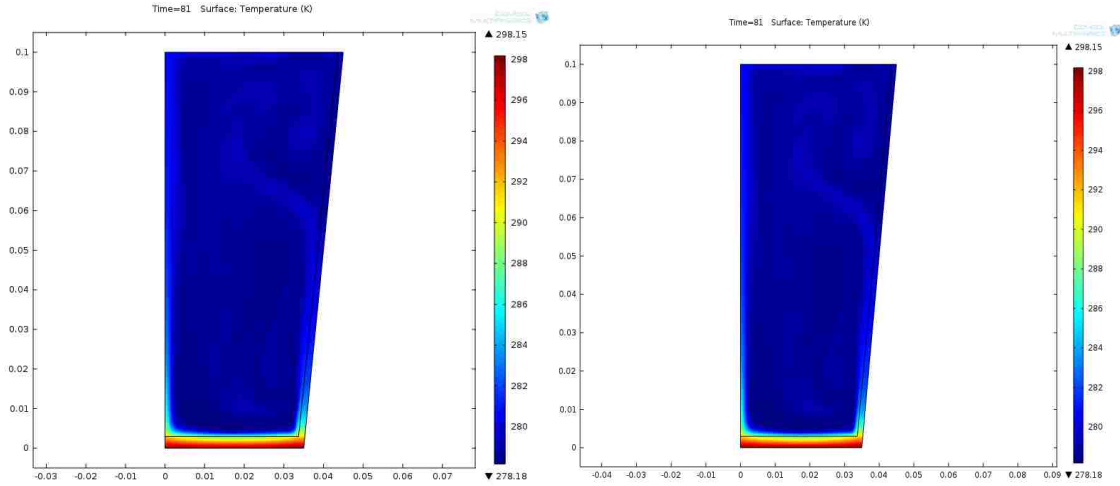
Figure A.2: *Water glass model at 81s. Modeled version (left) and COMSOL's version (right).*


Figure A.3: *Water glass velocity contour at 120s. Modeled version (left) and COMSOL's version (right).*

In order to back the full ZBLAN model in to the water glass model, the minor differences were slowly changed and the progression is described as follows. Figure A.4 shows the water glass model with the glass container removed.
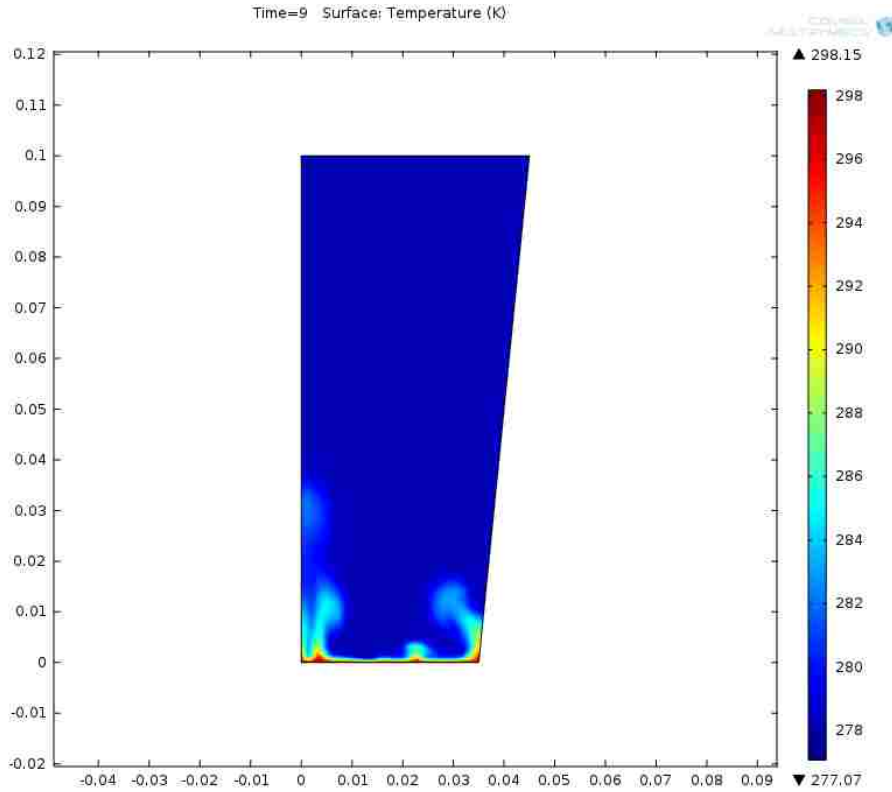
Figure A.4: *Temperature gradient of water with glass removed at 9s.*

Next, with the geometry still the same; the properties were changed to the calculated ZBLAN properties, as shown in Figure A.5. In addition to the property changed, the temperature numbers were changed to that appropriately matching the experimental conditions.
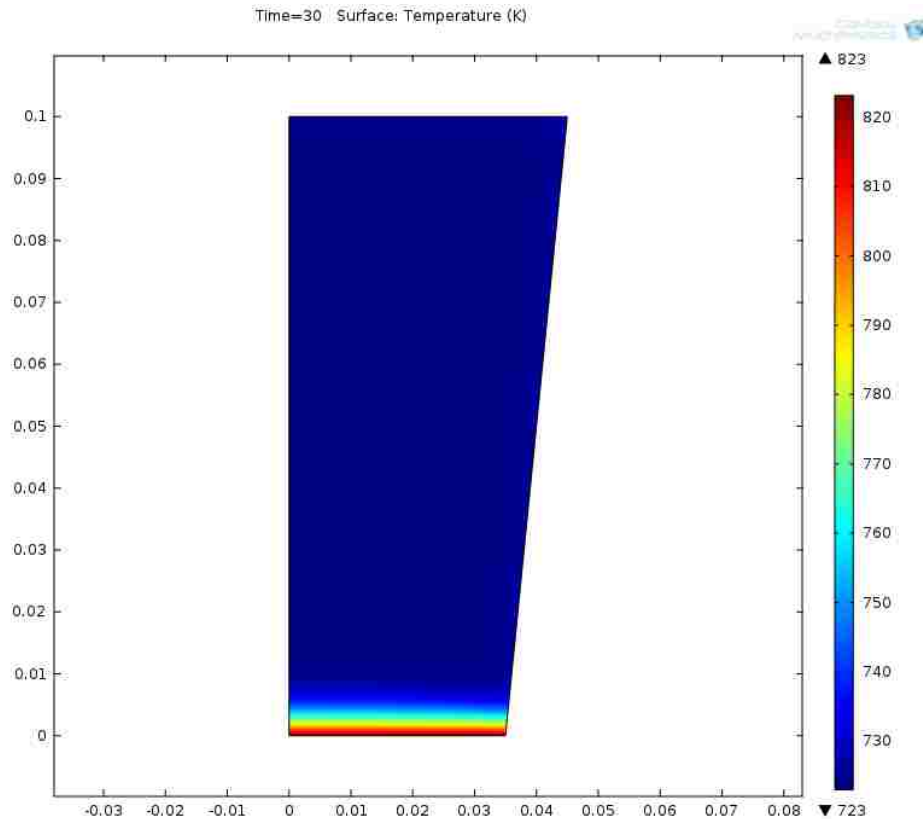
***Figure A.5:*** *Water model temperature gradient with glass removed and w/ ZBLAN*

material at 20s heated from 723K to 833K.

As shown in Figure A.5, the heating location is still on the bottom of the sample, as per

the water glass model. The next change involved manipulating the geometry so that the

sample has the same dimensions as the experimental sample, this can be seen in Figure

A.6.
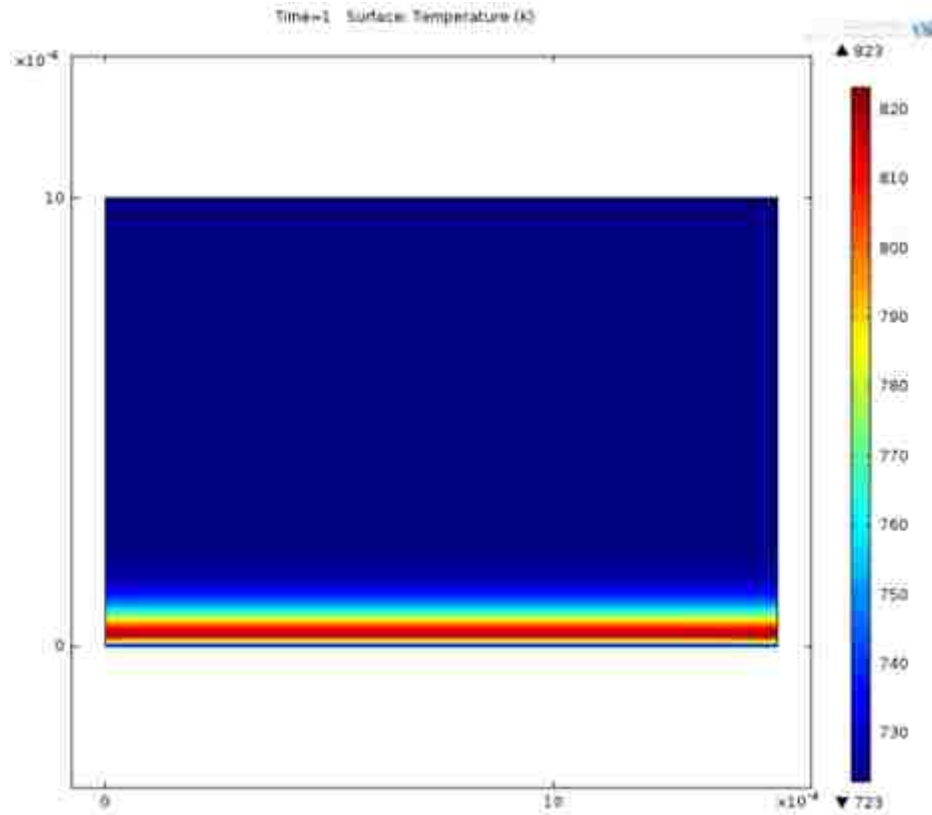
Figure A.6: *ZBLAN temperature gradient when heated from bottom (3d-axisymetric)*

from 723K to 833K at 1s.

As described in Figure A.6, the sample is still heated from the bottom only and is still a
3d-axisymetric model. The next change implemented is applying the heating conditions
on all edges of the sample.
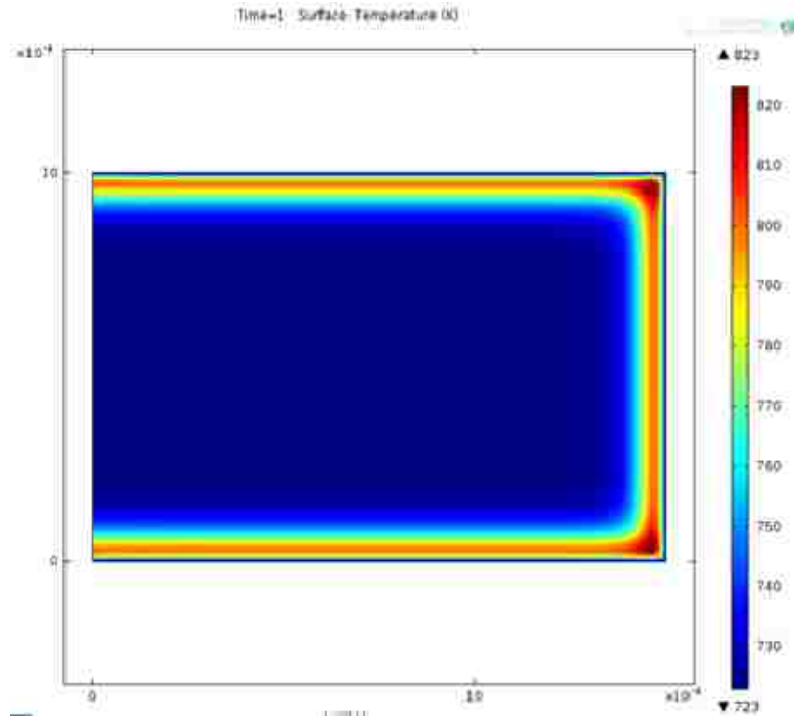
Figure A.7: *ZBLAN temperature gradient (2d-axisymetric) when heated from all side*

from 723K to 833K.

The final step in obtaining the full ZBLAN model in COMSOL was to remove the 3d-axisymetric boundary condition located on the left side of the sample. Currently, (Figure A.7) the model geometry is a thin cylinder (disk-like) shape. The geometry should revolve around the x-axis as opposed to the y-axis to make a long cylindrical shape. However a 2-d cross section analysis model is representative of the actually cylindrical sample. Figure A.8 shows the sample with the symmetrical boundary condition removed.
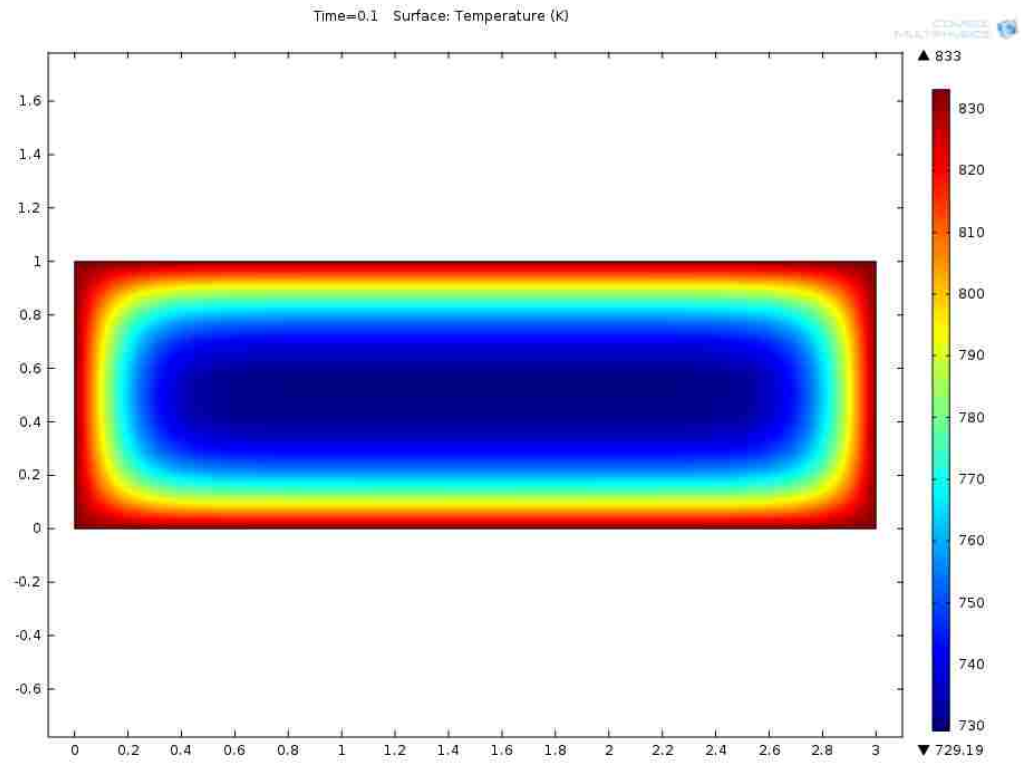
Figure A.8: *ZBLAN temperature gradient when heated from 723K to 833K at 0.1s.*

A velocity contour of the same ZBLAN sample can be seen in Figure A.9.
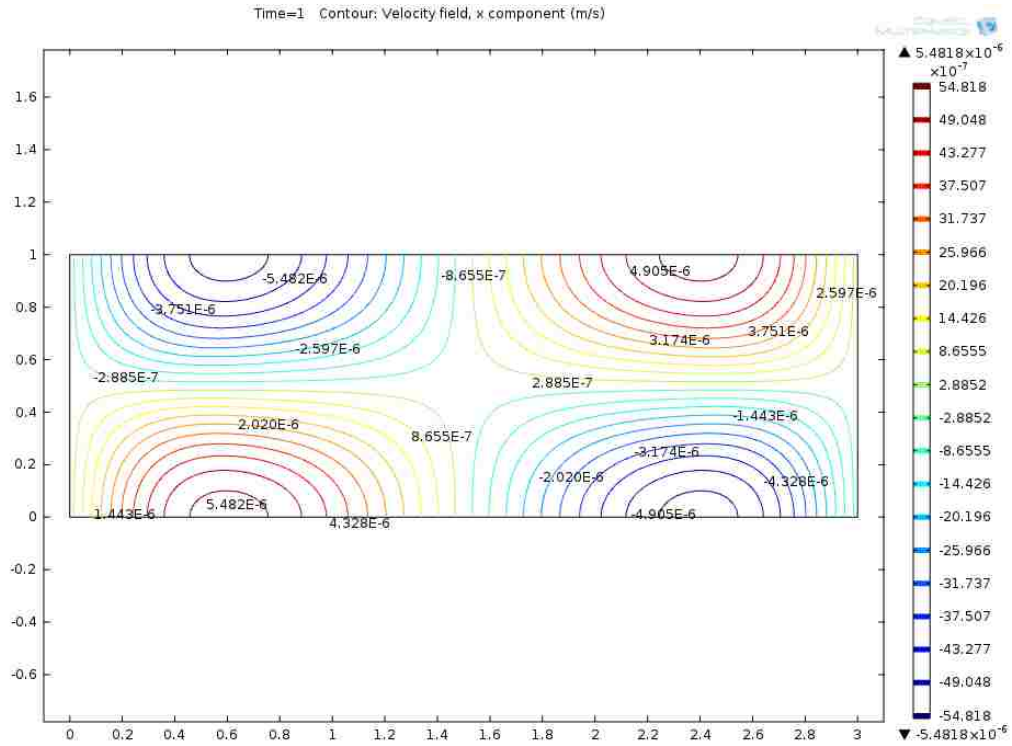
Figure A.9: *ZBLAN velocity contour when heated from 723K to 833K at 1s.*

This process overall verifies the results provided by COMSOL when modeling a ZBLAN

sample, similarly to the experimental program.

REFERENCES

Al-Laham S., "Stress Intensity Factor and Limit Load Handbook", British Energy Generation Ltd., EPD/GEN/REP/0316/98, ISSUE 2, © 1999, pp. AI32-AI37.

Anstis G. R., Chantikul P., Lawn B. R., and Marshall D. B., "A Critical Evaluation of Indentation Techniques for Measuring Fracture Toughness: I, Direct Crack Measurements", J. of the American Ceramic Society, V64, No. 9, pp. 533-538.

Boutarfaia A., Legouera M., Poulain M., "Glass formation and crystallization kinetics in a multicomponent fluoride glass", Journal of Non-Crystalline Solids 291 (2001) pp. 176-180.

Berg, S., "Measurement of extensional viscosity by stretching large liquid bridges in microgravity," *Journal of Non-Newtonian Fluid Mechanics,* V55, 1994, p.307-319

Cranmer D. C., Freiman S. W., White G. S. and Raynes A. S., "Moisture and water induced crack growth in optical materials", SPIE Proceedings, V1330, 1990, pp. 152-163.

Dhindaw, K. B., "Solidification under microgravity," *Sādhanā,* V26, Parts 1 & 2, 2001, p.59-69.

Dunkley, R. I., "The Study of Devitrification Processes in Heavy-Metal Fluoride Glasses," *Annal New York Academy of Science,* V1027, 2004, p.150-157.

FAI Materials Testing Laboratory Incorporated, 825 Chance Road, Marietta, Georgia 30066, www.faimaterialstesting.com

Gong J., Chen Y. and Li C., "Statistical Analysis of Fracture toughness of soda-lime glass determined by indentation", Journal of Non-crystalline solids, V279, 2001, pp. 219-223.

Harrington, James A., "Infrared Fiber Optics," *OSA Handbook*, Vol. III, 2007

Hayashi, A., "Optical Fiber Cable Flexibility Design Under Plastic Deformation and Its Evaluation," *Electronics and Communications in Japan,* Part 1, V72, No. 6, 1989, p.725-732.

Hehlen A., Epstein R. I., Patterson W. M., "Synthesis of ultrapure ZBLAN glass for laser refrigeration", Proc. of SPIE Vol. 6907, Laser Refrigeration of Solids, edited by Richard I. Epstein, Mansoor Sheik-Bahae 2008.

Hiemenz P, and Rajagopalan, R., *Principles of Colloid and Surface Chemistry,* 3rd Ed., Marcel Dekker, 1997

Kundrot, C., "Microgravity and Macromolecular Crystallography," *Crystal Growth & Design,* V1, No. 1, 2001, p.87-99.

Leed E. A., Pantano C. G., "Computer modeling of water adsorption on silica and silicate glass fracture surfaces", Journal of Non-crystalline Solids", V325, 2003, pp. 48-60.

Meyers, M. and K. Chawla, *Mechanical Behavior of Materials,* 2nd Ed., Cambridge University Press, 2009

Nakao, Y. and Moynihan, C.T., "DSC study of crystallization and melting of ZrF_4-BaF_2-LaF_3-AlF_3-NaF glasses," *Material Science Forum,* 67/68, p. 187-195, (1991)

Nötzolda, K., "Temperature dependent fracture toughness of glass frit bonding layers" Microsystem Technologies, V16, No. 7, pp 1243-1249, July 2010

Ogmentum Incorporated, P.O. Box 4470, State Line, NV 88449-4470 USA, www.ogmentum.com

Park, Y., "Effect of the microstructure on the mechanical properties of a directionally solidified Y3Al5O12/Al2O3 eutectic fiber," *Journal of Materials Science,* V36, 2001, p.5593-5601

Poggemann J. F., Heide G. and Frischat G. H., "Direct view of the structure of different glass fracture surfaces by atomic force microscopy", Journal of Non-crystalline Solids", V326-327, 2003, pp. 15-20.

Probstein, R. F., *Physicochemical Hydrodynamics: An Introduction,* 2nd Ed., Wiley-Interscience, New York, 1994 [1994]

Regel, L. L., "Experiments on crystallization of semiconductor materials, eutectic alloys and crystal growth from water solution in microgravity," *Acta Astronautica,* Vol 21, No. 5, 1990, p. 331-348.

Ruihua L., Haobing W., Peizhen D. and Fuxi G., "Characterization of the defects in a ZBLAN glass", SPIE Proceedings, V1327, 1990, pp. 40-48.

Schaffer, J. et al., *The Science and Design of Engineering Materials,* 2nd Ed., WCB/McGraw-Hill, 1999

Sjölin, L., "Protein crystal growth of Ribonuclease A and Pancreatic Trypsin Inhibitor aboard the MASER 3 rocket," *Journal of Crystal Growth,* V110, 1991, p.322-332.

Strelov, I. V., "Mathematical Modeling and Experimental Investigation of the Effect of Temperature Gradients on Crystallization Processes under Terrestrial and Space Conditions," *Crystallography Reports,* V50, No. 3, 2005, p.490-498

Tran, D.C., G.H. Siegel & B. Bendow, "Heavy Metal Fluoride Glasses and Fibers: A Review," *Journal of Lightwave Technology.* Vol. 2, [5], p. 121-138 (1984).

Tucker, D., "Effects of gravity on processing heavy metal fluoride fibers," *Journal of Materials Research,* V12, No. 9, 1997, p.2223-2225.

Tucker, D., "Effects of Gravity on ZBLAN Glass Crystallization," *Annals New York Academy of Sciences,* 1027, 2004, p.129-137.

Tucker, D., "The effects of a magnetic field on the crystallization of a fluorozirconate glass," *Journal of Materials Research,* V22, No 6, 2007, p.1431-1434

Tucker, D. "Effects of microgravity on ZBLAN optical fibers utilizing a sounding rocket," *SPIE,* Vol. 2809, 1996, p.23-32.

Turnbull, D., "Under What Conditions can a Glass be Formed?" *Contemporary Physics,* V10, No. 5, 1969, p. 473-488.

Ulmann, D. R., "A kinetic treatment of glass formation," *Journal of Non-Crystalline Solids,* V7, 1972, p337-348.

Varma, S., "Effect of gravity on crystallization in heavy metal fluoride glasses processed on the T-33 parabolic flight aircraft," *Journal of Materials Science,* V36, 2001, p. 4551-4559.

Varma, S., "Effect of microgravity on optical degradation in heavy metal fluoride glasses processed on the CSAR-I sounding rocket," *Journal of Materials Science,* V36, 2001, p. 2027-2035.

Varma, S., "Effect of microgravity on optical degradation in heavy metal fluoride glasses processed on the CSAR-II sounding rocket," *Journal of Materials Science,* V37, 2002, p. 2591-2596.

Voloshin, A. E., "Perfection and Homogeneity of Space-Grown GaSb:Te Crystals," *Crystallography Reports,* V47, Suppl. 1, 2002, p.S136-S148.

Vlack, L., *Elements of Materials Science and Engineering,* 6th Ed., Addison-Wesley Publishing Company, 1989

Wilson, S.J., Gibson, S., Gaukrodger, S., Scott, M.G., "Observation of Crystallisation in Fluorozirconate Glasses", Materials Science Forum, V5, 1985, p. 269-274

Workman, G., Smith, G. O'Brien S., and Adcock L., "ZBLAN Microgravity Study," *Final Report submitted to National Aeronautics and Space Administration George C. Marshall Space Flight Center*, April 1995.